MULTIPLEXING ON A NANOPHOTONICS PLATFORM FOR QUANTUM OPTICS AND NEURAL INTERFACES

A Dissertation

Presented to the Faculty of the Graduate School

of Cornell University

in Partial Fulfillment of the Requirements for the Degree of

Doctor of Philosophy

by

Aseema Mohanty

December 2017

MULTIPLEXING ON A NANOPHOTONICS PLATFORM FOR QUANTUM OPTICS AND NEURAL INTERFACES

Aseema Mohanty, Ph.D.

Cornell University 2017

The integrated silicon photonics, or nanophotonics, platform was originally developed for optical interconnects for high bandwidth data transfer. The need to dramatically scale this platform for communications applications has led to active research in switching and multiplexing signals using different degrees-of-freedom of light such as path, wavelength, and the transverse spatial mode. In recent years, extending the platform to use new materials has allowed for a new range of applications such as quantum optics, biosensing, and spectroscopy that span the visible to mid-infrared wavelength range. Fully utilizing this platform allows an unparalleled level of control over a large set of optical channels in waveguides with reconfiguration capability, low power consumption, and more stability which can be applied to this broad range of applications. This allows large table-top optical setups for quantum optics and microscopy to be miniaturized to the compact footprint of a nanophotonics chip.

Here in this dissertation, we extend this multiplexing nanophotonic platform into the visible wavelength regime in order to address two areas that require high density optical channels: quantum optics and neural interfaces for optogenetics. We develop a platform based on low-loss silicon nitride waveguides that can be thermally tuned using integrated microheaters to introduce reconfigurability in the visible wavelength range. We show how nanophotonic optical channels can be used for both quantum interference as well as neuron

activation within the brain.

To scale up the integrated quantum optics platform, we developed nanophotonics building blocks that utilize the transverse spatial modes within a single multimode waveguide for key quantum interference experiments that form the basis of more complex transformations within a smaller footprint. We used the transverse spatial degree-of-freedom because it can be controlled by simple geometric design, relieves the burden on the light source, and does not require non-standard materials, long delay lines, and high speed electronics, which is the case for time and frequency encoding. The high confinement of the silicon nitride allows for well separated modes that can be accessed by using geometry controlled selective phase matching. We demonstrated quantum interference using the higher order modes within a single multimode waveguide. We demonstrated both passive and active tuning of the interference between different modes while maintaining high visibility interference in the quantum regime.

To address the reconfiguration and resolution limitations of current optogenetic neural studies, we developed an implantable neural probe with an embedded reconfigurable nanophotonic switching network for creating high resolution spatiotemporal optical patterns. We use the same silicon nitride platform redesigned for the blue wavelength range. Using full phase control within a path interferometer network, we demonstrated a fully reconfigurable 1x8 switch that can control an array of microbeams to excite single neurons on a 20 microsecond timescale, much faster than neuron response times. We developed packaging techniques for the implantable nanophotonic chip for *in vivo* studies. We show for the first time precisely defined and repeatable neural spike patterns *in vivo* with unprecedented spatiotemporal resolution. Finally, we discuss how this platform can be extended for large-scale neural studies.

BIOGRAPHICAL SKETCH

Aseema Mohanty was born in Texas where she spent her entire childhood. With a combination of years of science projects based in her garage and kitchen and inspiration from a vibrant community of students, teachers, scientists, and engineers, Aseema attended and graduated high school from the Texas Academy of Mathematics and Science in 2007. During a summer internship at NASA, she discovered her fascination with light through laser-induced fluorescence studies of atmospheric re-entry materials. She went on to complete her bachelor's degree in the department of Electrical Engineering and Computer Science at the Massachusetts Institute of Technology (MIT). The close connections with fellow students and professors and fantastic opportunities for research and learning outside of the classroom made her experience at MIT invaluable. During her time there, she reconciled her love of two seemingly disparate fields of art and science which led to a passion for attacking challenging problems with creative design. Her undergraduate research focused on optoelectronic devices for renewable energy applications including thermophotovoltaics with Dr. Ivan Celanovic and organic photovoltaics with Professor Marc Baldo. Inspired by these research topics on light-matter interactions, she joined Professor Michal Lipson's group at Cornell University to study nanophotonics. With the support of a National Science Foundation Graduate Research Fellowship, her graduate research has focused on expanding the capabilities of the nanophotonics platform for visible wavelength applications including mode-division multiplexing for quantum information systems and switching networks for optical neural interfaces. The group's move from Cornell University to Columbia University allowed her to develop a close collaboration with Professor Adam Kepecs' neuroscience group at Cold Spring Harbor Laboratory. Under the supervision of

Michal Lipson and her energetic and supportive team, Aseema has been able to explore what it means to control and harness the flow of light for wildly different applications from quantum optics to neuroscience.

To my mother, father, brother, and partner, Deepali, for their eternal patience, support and love.

ACKNOWLEDGEMENTS

First, I would like to thank Professor Michal Lipson, my advisor, for her encouragement, trust and patience which allowed me to take on such challenging and eclectic projects. She is fearless when it comes to taking on new fields. During this time, I have learned how to enjoy being uncomfortable and navigating the unknown because this is essential to paving a new path. She has, also, taught me that communicating the importance of the research and engaging the public is essential to making progress in science and any field in general. Finally, Michal has created an open atmosphere that encourages collaboration and discussion that makes coming to the lab a joy every day.

I would like to thank my committee members, Professor Alexander Gaeta and Professor Clifford Pollock. I learned all things optics from their courses, from linear to nonlinear. Both Alex and Cliff have been a constant source of encouragement after every presentation and exam. Discussions with Alex have given me a better technical understanding and broad context of the field of optics. I admire Cliff's passion for teaching. Even as an established professor, he was flowing with energy and joy as he taught us how to build and align laser cavities in his class.

I had the pleasure of working closely with people from very different fields, quantum optics and neuroscience. First, I worked with Professor Paulo Nussenzveig from the University of Sao Paulo and Professor Sven Ramelow now at Humboldt University of Berlin on my quantum optics project who both helped me understand the broader context of this field. Their intuition and insight to understanding a seemingly mysterious topic were essential. I, also, had the privilege of getting to know Chaitali Joshi and Dr. Alessandro Farsi in the name of quantum through our weekly cake-with-a-side-of-quantum journal

club. Next, I worked with Dr. Qian Li and Professor Adam Kepecs from Cold Spring Harbor Laboratory on the neuroscience project. Both have given me an amazing crash course on neuroscience and inspired me to continue pursuing research in this field. I thank Adam for his dedication to technology development in neuroscience and allowing me to experiment within his lab. I, also, appreciate his guidance and fantastic discussions on everything ranging from machine learning to neuroscience. I thank Qian for her patience, energy and persistence which were essential to our successful collaboration on the neural experiment. I have never laughed so much while struggling with such challenging experiments. Finally, the people of the Marks building made me feel at home in their diverse and collaborative environment.

I would like to thank the organizations that funded my graduate research. I was supported by Cornell University's Lester B. Knight Fellowship and the National Science Foundation (NSF) Graduate Research Fellowship Program. The quantum optics project was funded by the NSF CIAN ERC. The neuroscience project was supported by an NSF EAGER grant. I also used the Cornell Nanofabrication Facility and the CUNY Advanced Science Research Center to fabricate my devices.

During graduate school, I have had the pleasure of being surrounded by the amazing individuals that make up the Lipson (previously Cornell) Nanophotonics Group. I thank Dr. Carl Poitras for setting up a framework that allowed such a large lab to run smoothly. I, also, thank Dr. Jaime Cardenas who taught me a great deal about the practical implementation of photonics in terms of design, fabrication, and testing. His advice on research and career direction has been very helpful. His advice on research and long term plans always came with a healthy dose of reality. In the early years, I learned all the basics of pho-

tonics and optics through discussion and debugging in the lab with the other members of the group while we were at Cornell University including Dr. Lucas Gabrielli, Dr. Lian-Wee Luo, Dr. Biswajeet Guha, Dr. Lawrence Tzuang, Dr. Mohammad Soltani, Dr. Raphael St-Gelais, and Dr. Felippe Barbosa. I admire each ones ability to boil down complex subjects to their essence. A special thanks to Lucas and Lian for getting me started in the cleanroom and making nanofabrication less daunting.

I worked closely with two people on my specific research projects. First, I would like to thank Dr. Mian Zhang for getting me started on my quantum optics project, specifically warning me of the many potential pitfalls. Mian taught me a great deal about setting up free-space optics setups and physics in general. Secondly, I would like to thank Dr. Amin Tadayon for working with me as we entered the foreign world of neuroscience. You have instilled the MacGyver spirit in me and taught me the importance of a tea-break.

There are many lab members that I had the pleasure of pursuing my degree with along side for many years at both Cornell University and Columbia University. To Dr. Romy Fain, your confidence and ability to reinvent yourself is something I strive towards. To soon-to-be Dr. Chris Phare, you are absolutely brilliant and driven, and I have had great pleasure debugging research problems with you. To Dr. Austin Griffith, Dr. Shreyas Shah, and Dr. Yoon Ho Daniel Lee, I did not know espresso could forge such a strong bond between people. It was great to start every morning with a cup in hand and a marker on the board.

I got to know the newer generation of lab members well during and after our transition to Columbia University. To Brian Stern, I always enjoy the discussion of modes, and your delivery is always impeccable. To Ipshita Datta, your cre-

ativity and insight on a variety of topics never ceases to amaze me and makes working with you incredibly fun. To Gaurang Bhatt, our bond grows stronger with every germanium diode we debug together (pun intended). To William Ji, thank you for all your help with the silicon nitride process. Your determination and work ethic has been very motivating. To Brian Lee, it was incredibly rewarding to see your hard work pay off after working with you when you joined as an undergraduate student. Those bridges were a work of art. To Moshe Zadka, thank you so much for always giving me very honest and sensible advice. Finally, to Oscar Jimenez, you are the warmest person I have ever met, and I appreciate the joy you bring to the lab every day. I hope I can pass on some of my experience for your future work. To the new folks in the lab including Dr. Utsav Dave, Dr. Tong Lin, Dr. You-Chia Chang, Dr. Sam Roberts, Euijae Shim, Mateus Zanarella and Min Chul Shin, I have already gotten to know you all in a short time and enjoy the perspective you bring from your previous labs and life.

There have been a few close friends within the lab that have had a profound impact on me during my graduate studies. To Dr. Avik Dutt, I will miss our seamless and endless conversation spanning the bosonic nature of light to mathematical derivations to life advice. It was a pleasure being your desk neighbor for many years, despite the bad puns. Your passion for science is infectious, and I look forward to having a close friend I can also collaborate with on research for many years. To Dr. Steven Miller, you always push me to look at things in a very different way both inside and outside the lab. I cherish your support and encouragement always, and it has been a pleasure exploring NYC with you. Finally, to Dr. Kevin Luke, I enjoyed picking apart the universe on the slope with you. You got me through my toughest times by making me laugh until it

physically hurt. Your sense of purpose and commitment to making the world a better place is inspiring.

Outside of the lab, a few people in particular made sure there was never a dull moment. To Dr. Radhika Patel and Pari Nene, you made Ithaca feel like home when I first started at Cornell. To Dr. Suren Jayasuriya and Dr. Ved Gund, I loved our late night ping-pong matches and discussions on philosophy and life.

Finally, I would like to thank my mother and father, Durgesh and Kishore Mohanty, for encouraging and nurturing my curiosity and independent thinking and to my brother, Dev Mohanty, for his unconditional support and mind-bending discussions. Finally, to my partner, Deepali Ravel for always believing in me, keeping me grounded, and inspiring me to work on problems that will have an important impact on the world.

My graduate school experience in both Ithaca and New York City has been the most inspiring and fun phase of my life so far, and this is entirely due to the people that surrounded me everyday who engaged in discussion, collaboration and support inside and outside of the lab. I will forever seek and create this type of environment because this energy is truly reflected everyone and their work.

TABLE OF CONTENTS

CHAPTER 1

INTRODUCTION

1.1 Nanophotonics for High Density Optical Channels

The integrated silicon photonics, or nanophotonics, platform was originally developed for optical interconnects for high bandwidth data transfer. The need to dramatically scale this platform for communications applications has led to active research in switching and multiplexing a large number of signals using different degrees-of-freedom of light such as path, wavelength, and the transverse spatial mode[1, 2, 3, 4, 5]. In recent years, extending the platform to use new materials has allowed for a new range of applications such as quantum optics, biosensing, and spectroscopy that span the visible to mid-infrared wavelength range[6, 7, 8, 9]. Fully utilizing this platform allows an unparalleled level of control over a large set of optical channels in waveguides with reconfiguration capability, low power consumption, and more stability which can be applied to this broad range of applications. This allows large table-top optical setups for quantum optics and microscopy to be miniaturized to the compact footprint of a nanophotonics chip.

1.2 Scaling up Photonic Quantum Systems

Photonic quantum information processing has the potential to revolutionize how we transfer information and solve large intractable problems using the quantum nature of light[10, 11]. In the free-space optical domain, experimental

demonstrations and theories have proven that quantum information processing can provide computational speed ups and enhanced security in communications channels. Chip-scale quantum optics allows us to take a table-top free-space optical setup with a large network of interferometers and miniaturize it to millimeter-scale, making its practical and commercial implementation possible. To encode information using photons, the community has typically used the path degree-of-freedom, which is implemented using single mode waveguides that are physically separated. Transformations on these sets of path-modes is done using standard optical interferometers[12, 6, 13, 14, 15]. Practical quantum computing will require building blocks that can manipulate other degrees-of-freedom that can drastically scale the number of modes such as time, frequency and transverse spatial modes within a single waveguide. Encoding within these high-dimensional degrees-of-freedom can reduce the footprint of the overall system, reduce losses due to waveguide crossings, and relieve resource requirements for the quantum photon sources and detectors.

1.3 Compact High Resolution Reconfigurable Optical Neural Interface

Like quantum computational systems, optical neural interfaces also demand an active reconfiguration of a large number of optical channels. To study the many connections ($\sim 10^{15}$) and functions of neurons in the brain on a single cell level requires a high resolution neural interface that is simultaneously non-invasive. The field of optogenetics transformed the way we study the brain by allowing genetic modification of neurons to be responsive to light[16]. This has al-

lowed some level of control and specificity that was not possible with electrical stimulation methods. However, current optical techniques for high resolution excitation (i.e. free-space microscopy) rely on techniques that are bulky and can only penetrate 1-2 mm into the brain due to the high scattering of visible wavelength light. To overcome this, typically optical fibers have been used to penetrate deeper into the brain. This approach floods the brain with light and excites many neurons, limiting the resolution and complexity of optical stimulation patterns. There is a significant need for a high resolution reconfigurable neural interface with a compact form factor that can be implanted within the brain.

1.4 Organization

Here in this dissertation, we show how to extend the multiplexing nanophotonic platform into the visible wavelength regime in order to address two areas that require high density optical channels: quantum optics and neural interfaces for optogenetics. We develop a platform based on low-loss silicon nitride waveguides that can be thermally tuned using integrated microheaters to introduce reconfigurability in the visible wavelength range. In Chapter 2, we discuss the integrated nanophotonics platform based on thermally-tuned silicon nitride, which includes basic background information and theory for integrated interferometers. In the following chapters, we show how nanophotonic optical channels can be used for both quantum interference and neuron activation within the brain. In Chapter 3, we discuss background information on quantum optics. In Chapter 4, we discuss our experimental work on mode-division multiplexing for quantum optics. In Chapter 5, we discuss background information

on neural interfaces for optogenetics studies including current technologies for light delivery into the brain. In Chapter 6, we will discuss our implantable nanophotonics platform for high spatiotemporal resolution optogenetics excitation *in vivo*. We will include the discussion and future work for each application within their respective chapters.

CHAPTER 2

INTEGRATED NANOPHOTONICS

2.1 Waveguides

The integrated nanophotonics platform is a system of orthogonal optical modes defined by confined light in waveguides. A waveguide can be formed by creating a channel with a material that has a refractive index, n_{core}, and surrounding it with a cladding material with refractive index, $n_{cladding}$ (see Fig. 2.1). For light to be guided in this situation, n_{core}, must have a higher index than $n_{cladding}$. The nanophotonics platform uses waveguides that have dimensions that are smaller or on the order of the wavelength of light, λ, so we must think in terms of wave optics and optical modes, rather than ray or geometric optics.

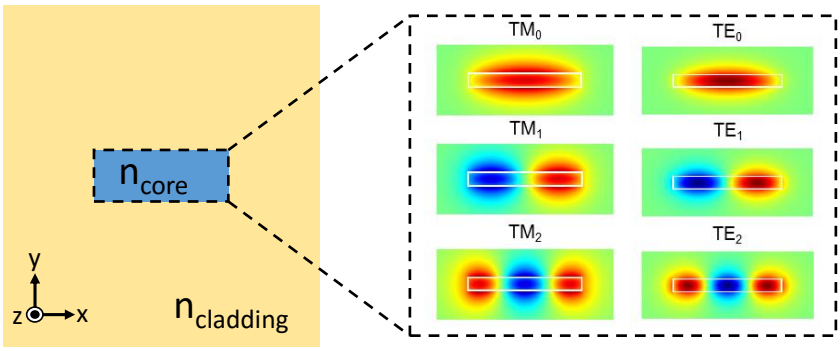

Figure 2.1: **Optical modes of a waveguide.** Left: Cross-section of a channel waveguide. Right: Numerical simulations of the transverse-electric (TE) and transverse-magnetic (TM) optical modes.

One can think of the channel waveguide as a potential well in two dimensions for the light. The light remains confined within the waveguide which

allows it to be guided by the waveguide as long as no abrupt changes such as a sharp bend occur. This potential well is defined by the boundary conditions given by the refractive index profile and Maxwell's equations. An optical mode is a solution to Maxwell's equations that satisfies its boundary conditions at all interfaces between different materials. This results in an eigenvalue equation in which the eigenvalues are the effective indices, n_{eff}, and the eigenvectors are the transverse spatial mode profiles. The propagation constants, β, can be derived from the effective indices as $\beta = k_0 n_{eff}$ where $k_0 = \frac{2\pi}{\lambda}$. If there are no perturbations to the waveguide, the light remains in this optical mode as it travels in space along the propagation direction with a phase velocity, $v_p = \frac{c}{n_{eff}}$, where c is the speed of light.

High index contrast between the core and cladding materials allow one to make compact and easily tailorable optical waveguide modes, but they are susceptible to high loss due to scattering at the interfaces between materials. The index contrast in a fiber is approximately 0.002. However, high index contrast waveguides have index contrasts of approximately 0.2 for silicon nitride and 0.4 for silicon waveguides with silicon dioxide cladding, which are two orders of magnitude higher. This allows one to highly confine light, so that the cross-sections are less than a wavelength and bends are on the order of 10-100 microns depending on wavelength. With higher index contrast, small changes to the geometry create larger changes to the effective index of the optical mode which can be used to tailor dispersion. We will use this feature in our mode-division multiplexing platform to manipulate the transverse spatial modes.

2.1.1 Transverse Spatial Waveguide Modes

The transverse spatial waveguide modes are orthogonal modes defined by their transverse spatial electromagnetic field distribution in the dimensions (x,y) perpendicular to their propagation axis (z) for a single wavelength (directions noted in Fig. 2.1). The optical mode solutions for a rectangular waveguide can be characterized as quasi-transverse-electric (TE) and quasi-transverse-magnetic (TM) because the polarization, or direction of their electric field, E, is not purely in one direction. A TE mode is defined as one with a dominant E_x and negligible E_y component, and a TM mode is defined as one with a dominant E_y and negligible E_x component. Figure 2.2 shows an example of this. For the rest of this dissertation, we will ignore this smaller component. However, it is important to keep in mind that this component can be used to couple modes of different polarizations by using these non-zero components. Depending on

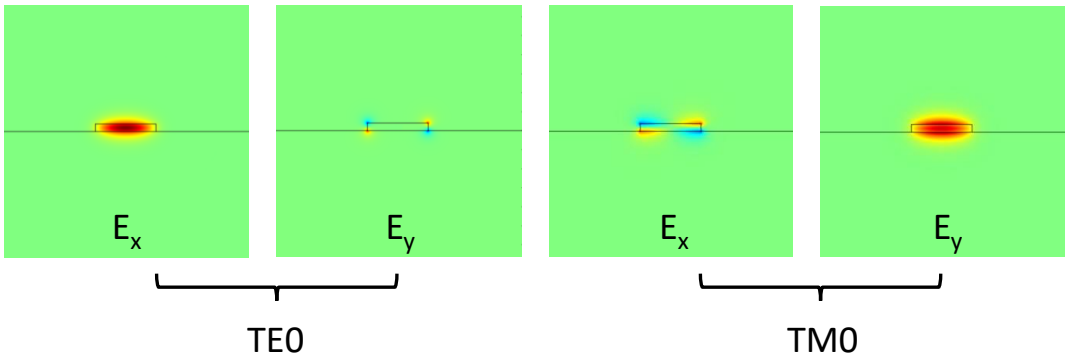

Figure 2.2: **Electric field of quasi-TE and quasi-TM modes.** Numerical simulations of dominant and non-dominant electric fields of the TE0 and TM0 modes.

the strength of the index contrast and size of the waveguide which essentially dictates the size of the potential well, there can exist multiple solutions to the

eigenvalue problem. This results in higher order transverse spatial modes with different propagation vectors. These TE_m and TM_m modes can be characterized into even modes which are symmetric around the x-axis and odd modes which are anti-symmetric around the x-axis, where m defines their order by the number of nodes in the x dimension. For simplicity, we will only discuss modes with nodes in the x dimension. However, with larger waveguide heights, there exist modes with nodes in both x and y dimensions.

High-index contrast waveguides allow us to control the propagation constant (and effective index) and dispersion of the optical mode by small changes to the geometry of the waveguide. In Fig. 2.3, we show how the propagation constants of the different modes changes with both width and height of the waveguide.

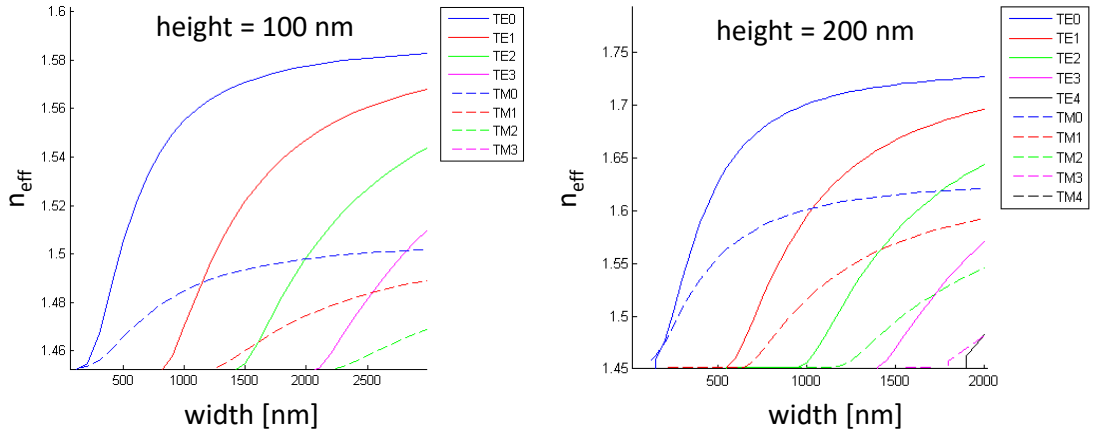

Figure 2.3: **Tailoring the effective index of high-index contrast waveguides.** The effective index of a silicon nitride waveguide near 800 nm wavelength as a function of width and height (Left: 100 nm and Right: 200 nm) of the waveguide. Note the maximum effective index for the fundamental modes.

The effective indices decrease with mode order because the higher order modes are less confined and experience more contribution from the cladding

refractive index. As the width of the waveguide increases, all the effective indices tend to saturate at a certain point because the solutions are approximating that of a slab waveguide which is infinite in the x dimension. As the height is increased, the effective indices of the different modes are spread out more between a higher max effective index value, also the TE and TM modes become closer to one another. At one point, when the height is larger than the width, the TM modes will have the higher indices than the TE modes. Here one can see when the waveguide height and width are the same, the TE and TM modes have the same effective index. The modes are still orthogonal to one another, as one can see because there is no avoided crossing which is a signature of coupled modes [17]. However, if there is any asymmetry in the refractive index profile of the waveguide such as non-vertical sidewalls, this could lead to coupling between TE and TM modes.

2.2 Mode Coupling

To perform tasks like switching or routing light in different directions, one must create structures that allow the modes to interact with one another and break their original orthogonality. This interaction is called coupling between modes. Here we will discuss coupling between two spatial optical modes. This includes but is not limited to coupling between modes in different adjacent waveguides, coupling between higher order modes within the same waveguide, or even coupling to radiation modes outside of the waveguide. This coupling arises from the non-zero overlap of two modes within the perturbed region.

Coupled-mode theory for weakly coupled modes has been derived in many

textbooks. Here we adapt the derivation from Haus[18]. Coupled-mode theory relates the complex amplitudes of modes a_1 and a_2 through a set of differential equations, where β_1 and β_2 are the uncoupled mode propagation constants and κ_{12} and κ_{21} are the coupling coefficients between the two modes.

$$\frac{da_1}{dz} = -j\beta_1 a_1 + \kappa_{12} a_2 \tag{2.1}$$

$$\frac{da_2}{dz} = -j\beta_2 a_2 + \kappa_{21} a_1 \tag{2.2}$$

The solution to these equations assuming that the waves $a_1(0)$ and $a_2(0)$ are launched at z=0 is the following:

$$a_1(z) = [a_1(0)(\cos\beta_0 z + j\frac{\beta_2 - \beta_1}{\beta_0}\sin\beta_0 z) + \frac{\kappa_{12}}{\beta_0} a_2(0)\sin\beta_0 z]e^{-j[\frac{\beta_1+\beta_2}{2}]z} \tag{2.3}$$

$$a_2(z) = [\frac{\kappa_{21}}{\beta_0} a_1(0)\sin\beta_0 z + a_2(0)(\cos\beta_0 z + j\frac{\beta_1 - \beta_2}{\beta_0}\sin\beta_0 z)]e^{-j[\frac{\beta_1+\beta_2}{2}]z} \tag{2.4}$$

where

$$\beta_0 = \sqrt{(\frac{\beta_1 - \beta_2}{2})^2 + |\kappa_{12}|^2} \tag{2.5}$$

and the original modes a_1 and a_2 are now mapped onto the supermodes of the coupled mode structure defined by $\beta_\pm$:

$$\beta_\pm = \frac{\beta_1 + \beta_2}{2} \pm \beta_0 \tag{2.6}$$

The supermodes are symmetric and anti-symmetric superpositions of the two uncoupled modes. The separation of the propagation constants is defined by the amount of coupling between the two original modes. We will not discuss the effects of avoided crossings on waveguide dispersion here because the work in this dissertation is for a single wavelength, but see Haus for a more detailed discussion[18].

If, initially, $a_1(0) = 1$ and $a_2(0) = 0$, the power coupled from a_1 to a_2 is:

$$|a_2(z)|^2 = |a_1(0)|^2 \left|\frac{\kappa_{21}}{\beta_0}\right|^2 \sin^2 \beta_0 z \tag{2.7}$$

For perfect phase matching where $\beta_1 = \beta_2$, this becomes:

$$|a_2(z)|^2 = |a_1(0)|^2 \sin^2 |\kappa_{21}| z \tag{2.8}$$

Significant power transfer can only occur if the two modes have the same propagation constants. The power oscillates between the two modes at a frequency defined by the coupling coefficient (see Fig. 2.4). Here we define the splitting

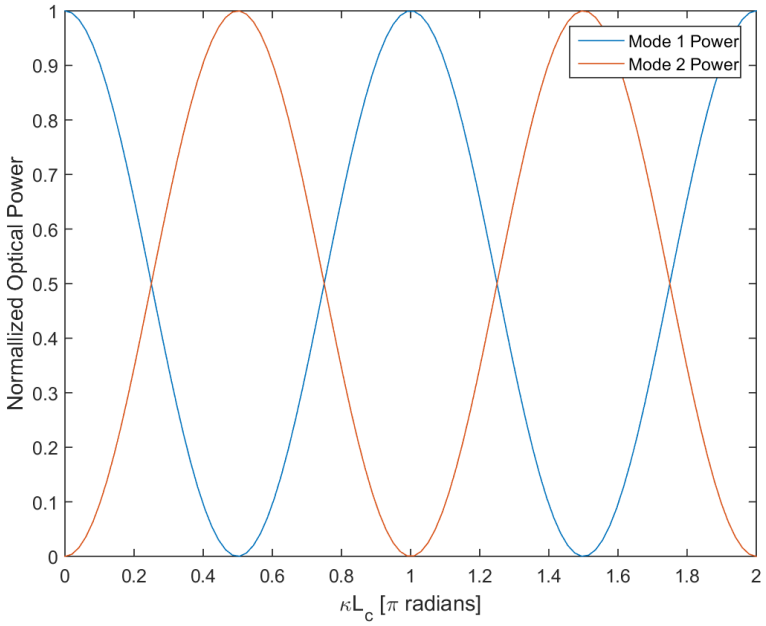

Figure 2.4: **Power transfer between perfectly phase matched optical modes.** Assuming initially there is only power in mode 1, the power transfers between the two modes sinusoidally as function of the coupling coefficient, κ, and coupling length, L_c.

ratio, η, as the ratio of power that remains in the same mode:

$$\eta = 1 - \frac{|a_2(z)|^2}{|a_1(0)|^2} = \left|\frac{\kappa_{21}}{\beta_0}\right|^2 \cos^2 \beta_0 z \tag{2.9}$$

For perfect phase matching where $\beta_1 = \beta_2$, this becomes:

$$\eta = \cos^2 |\kappa_{21}| z \tag{2.10}$$

2.2.1 Coupling Mechanisms

Any perturbation to the modes will break the orthogonality and allow them to interact and couple. The coupling coefficient, κ, which defines the interaction between the two modes comes from overlap of the two modes in the perturbed region. There are many ways to do this, but we will discuss two ways to couple modes in this dissertation that are often used in integrated photonics devices.

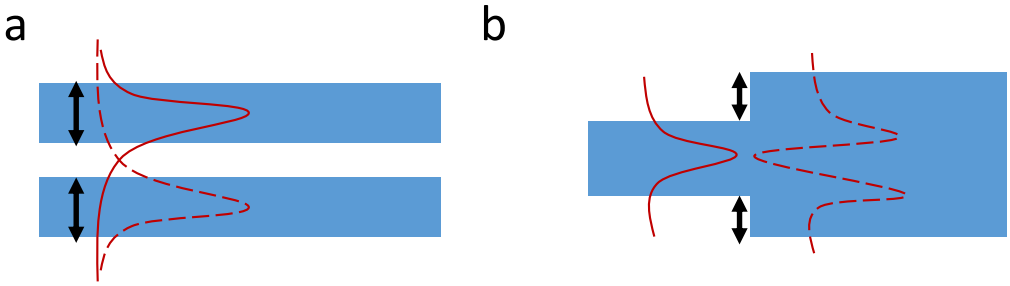

Figure 2.5: **Coupling due to mode overlap between mode 1 (solid line) and mode 2 (dotted line).** a) Evanescent tails of two modes have a non-zero overlap within the region of perturbation indicated by the black lines. b) The two modes have a non-zero overlap in the region of perturbation indicated by black lines.

Evanescent Coupling

Evanescent coupling is typically used for coupling modes between two waveguides. The waveguides are placed close enough to one another, so that the

evanescent tail of the mode of one waveguide overlaps with the mode of the adjacent waveguide (see Fig. 2.5a). This leads to the coupling coefficient $|\kappa_{21}|$ or $|\kappa_{12}|$ which is defined per unit length as seen in the previous section. Typically, The length of the coupling region, or the length of interaction, determines the overall power coupled, as seen in Eq. 2.10. These modes are typically phase-matched through modifying the width of the waveguide.

Periodic Perturbation

Periodic perturbation is used for coupling modes with different propagation vectors. This can be done for modes within a single waveguide, to radiation modes, between modes of different polarizations, and between adjacent waveguides. The perturbation allows a non-zero overlap of the two modes at the interface of the original waveguide section and the perturbed waveguide section, which leads to coupling (see Fig. 2.5b). The perturbation is achieved typically by a change in waveguide dimension. However, this can be implemented using any refractive index change that the mode will experience.

To do this efficiently, or to achieve significant power transfer using this method, one must match the propagation constants by introducing this coupling with a frequency defined by the propagation constant mismatch. The coupled mode equations can be rewritten to include this space variation along the propagation axis. If we assume a perfect sinusoidal frequency variation, then Eq. 2.1 and Eq. 2.2 become:

$$\frac{\mathrm{d}a_1}{\mathrm{d}z} = -j(\beta_1 - \frac{\pi}{\Lambda})a_1 + \kappa_{12}a_2 \tag{2.11}$$

$$\frac{da_2}{dz} = -j(\beta_2 + \frac{\pi}{\Lambda})a_2 + \kappa_{21}a_1 \tag{2.12}$$

Which leads to a new phase mismatch, $\Delta\beta$ that depends on the spatial frequency of the perturbation, Λ:

$$\Delta\beta = \beta_1 - \beta_2 - \frac{2\pi}{\Lambda} \tag{2.13}$$

Therefore, to phase match these two modes, one must use the following spatial frequency:

$$\Lambda = \frac{2\pi}{\Delta\beta} \tag{2.14}$$

The coupling occurs at each perturbation, so we can convert $|\kappa_{21}|$ (coupling per length) to κ (coupling per period) to get from Eq. 2.10 the splitting ratio:

$$\eta = \cos^2 \kappa N \tag{2.15}$$

where N is the number of periods.

In effect the spatial modulation gives the modes an effective propagation constant that is shifted from its unmodulated version. The wave is given spatial sidebands, much like with temporal modulation. The sinusoid has a single spatial frequency which allows for coupling to one other mode. For multiple spatial frequencies, this allows for coupling to multiple different modes. This is the new type of coupling mechanism we introduce for higher order modes in this dissertation.

2.3 Beamsplitters

A beamsplitter, in the most general sense, takes two optical modes and splits the power between them. In free-space optics this is commonly a glass cube

with a partially reflecting interface along the diagonal. In integrated photonics, we can create a beamsplitter with arbitrary splitting ratios, η, using the coupling principles from the previous section (see Eq. 2.10). In general a two-mode beamsplitter relates the input mode amplitudes, a_{i1} and a_{i2}, by the following equation:

$$\begin{bmatrix} a_{o1} \\ a_{o2} \end{bmatrix} = \begin{bmatrix} \sqrt{\eta} & \sqrt{1-\eta} \\ \sqrt{1-\eta} & -\sqrt{\eta} \end{bmatrix} \begin{bmatrix} a_{i1} \\ a_{i2} \end{bmatrix} \tag{2.16}$$

In free-space, the two modes are two different paths as shown in Fig. 2.6, where there is a certain probability that the power will stay within the same mode, it is transmitted, or converted to the other mode, it is reflected. The special case of a 50:50 beamsplitter occurs when this splitting ration $\eta = 0.5$. This is commonly used in most interference structures that require even splitting.

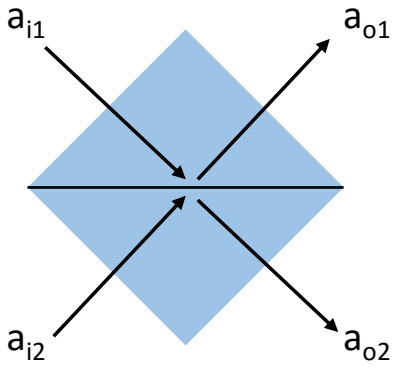

Figure 2.6: **Inputs and Outputs of a Beamsplitter.** Light that is input into a_{i1} is partially reflected and exits through a_{o1} and partially transmitted and exits through a_{o2}. The same occurs for light that is input through all the other ports according to Eq. 2.16.

2.3.1 Directional Couplers

In integrated photonics, the most common beamsplitter is a directional coupler. As discussed in the previous section, two waveguides can couple with one another by interaction through their evanescent tails of the mode. In Fig. 2.7a-b, there is an example of power transfer between two waveguides. The splitting ratio depends on the interaction length and follows Eq. 2.10. For full power, the length of this coupling region is $L_{full} = \frac{\pi}{2\kappa}$. For a 50:50 beamsplitter, the length of this coupling region is $L_{half} = \frac{\pi}{4\kappa}$. The coupling gap, or the gap between the two waveguides, determines the coupling coefficient, κ.

Although directional couplers are commonly used, they are still sensitive in terms of wavelength, polarization, and fabrication. For example, Fig. 2.7c-d shows how the splitting ratio deviates the designed value of 0.5 as the structure grows in dimension and the wavelength changes. Here the growth factor is a multiplication factor for all the dimensions to mimic the shrinking and swelling that can occur during fabrication. The 50:50 power transfer point for a directional coupler sits on a steep slope, so if one deviates from this point in either direction, the splitting ratio becomes more unbalanced.

2.3.2 Multimode Interferometer

A beamsplitter can also be constructed from a multimode interferometer (MMI). The MMI consists of waveguides that enter a larger multimode section (see Fig. 2.8a). In this case the abrupt perturbation causes the input waveguide modes to be mapped onto the modes of a wider section called the MMI. Due to the nearly quadratic nature of the propagation constants of the higher order modes, there

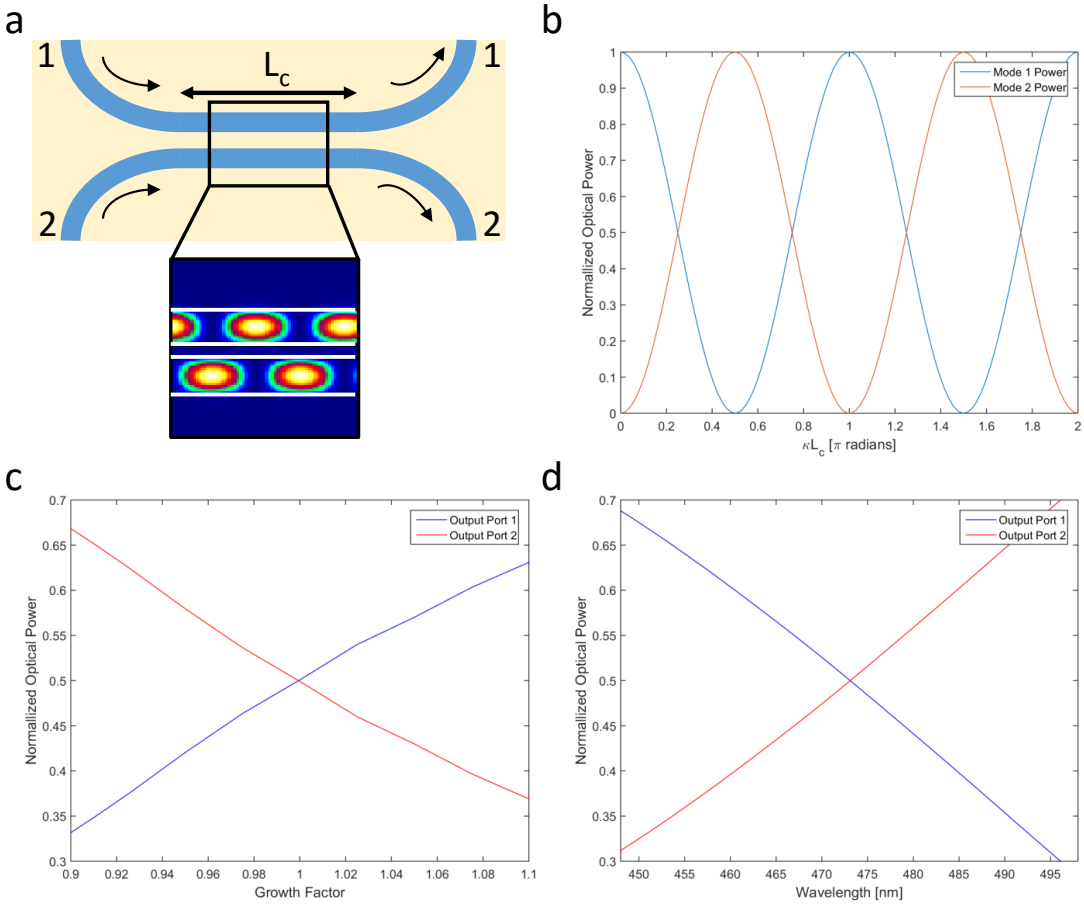

Figure 2.7: **Performance of a Directional Coupler.** a) Schematic of a directional coupler with coupling length, L_c. b) Shows optical power transfer between two modes when light is input into mode 1. c) Shows the effect of a growth factor on the splitting ratio. d) Shows the effect of wavelength on the splitting ratio designed for 473 nm.

is a self-imaging phenomena that results from the mode beating. If the device is cut along the length at specific locations, one can create a 50:50 beamsplitter. See Fig. 2.8a-b for an example of this mode beating phenomena.

Although it is more difficult to design a variable splitting ratio, it has the advantage of being more tolerant to wavelength, polarization, and fabrication. Typically, the width of the waveguide is fixed, and the width and length of

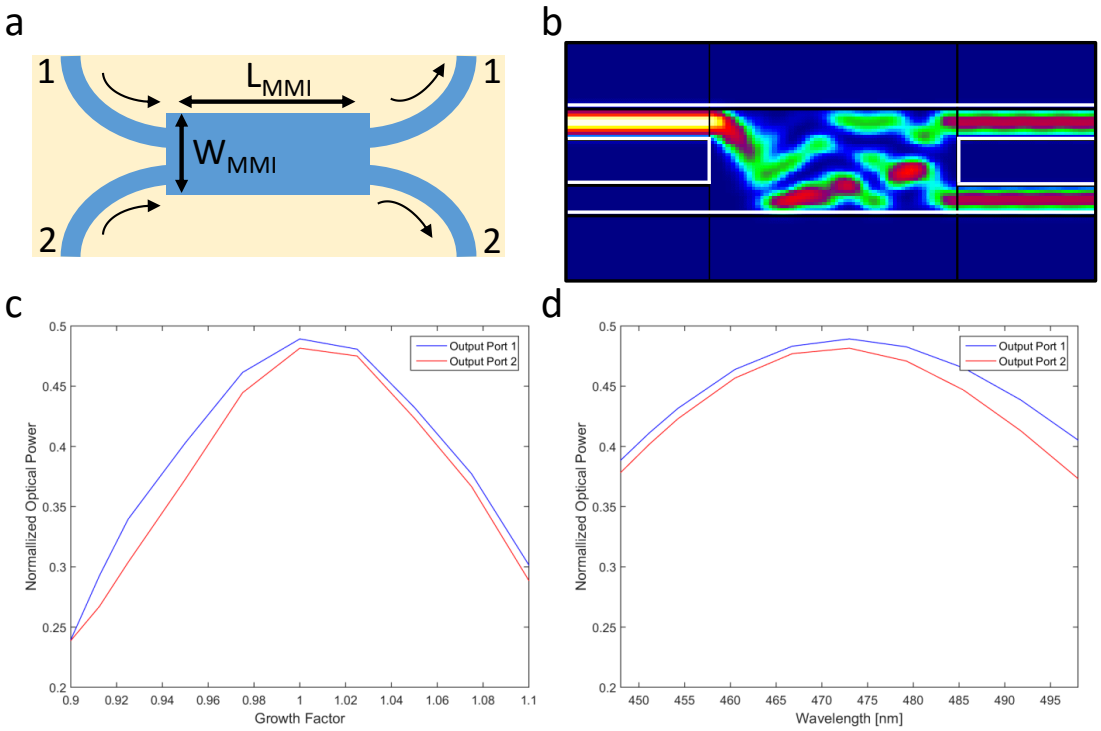

Figure 2.8: **Performance of a Multimode Interferometer (MMI) Coupler.** a) Schematic of a MMI with width, W_{mmi}, and length, L_{mmi}. b) Numerical simulation of the mode beating within a 50:50 MMI coupler when light enters through mode 1. c) Shows the effect of a growth factor on the splitting ratio. d) Shows the effect of wavelength on the splitting ratio designed for 473 nm.

the MMI is varied in simulation to find an optimal splitting ratio. Deviation from the optimal point for a 50:50 beamsplitter using an MMI only makes the beamsplitter more lossy, but it keeps the splitting ratio even. This is ideal in many cases for good extinction within an interferometer.

2.3.3 Gratings

Gratings use the principle of periodic perturbation to couple the forward and backward propagating modes and to couple waveguide modes to radiation modes. For example, gratings can be used to couple a guided mode with β_1 to a radiation mode exiting the waveguide at a certain angle with β_2:

$$\beta_1 = \frac{2\pi n_{eff}}{\lambda} \tag{2.17}$$

$$\beta_2 = \frac{2\pi n_{cladding} \sin(\theta)}{\lambda} \tag{2.18}$$

The period of the grating is used to determine for which angle the two modes are phase matched.

$$\Delta\beta = \beta_1 - \beta_2 - \frac{2\pi}{\Lambda} \tag{2.19}$$

$$sin(\theta) = \frac{\Lambda n_{eff} - \lambda}{n_{cladding}\Lambda} \tag{2.20}$$

Gratings can also be used to couple higher order modes to one another within the same waveguide, which we show in this dissertation.

2.4 Path-based Interferometers

Tuning the phase and, therefore, the interference between two paths form the basis of switching and routing light in integrated photonics. Interferometers have been primarily formed using optical modes defined by their path. With

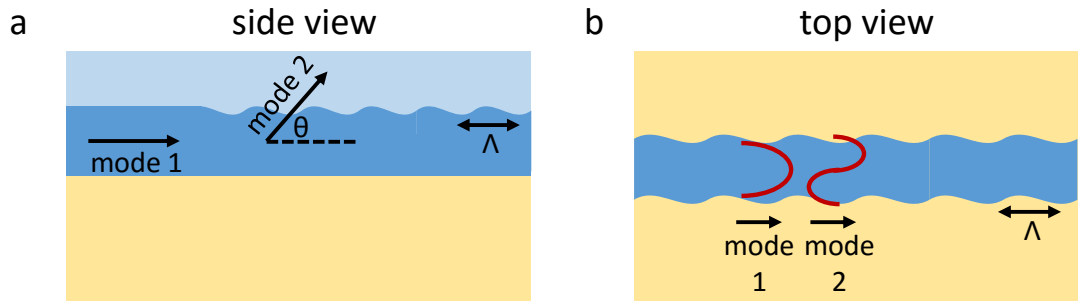

Figure 2.9: **Gratings using periodic perturbation for mode coupling.** a) Schematic of coupling a guided mode to a radiation mode using periodic perturbation. b) Schematic of coupling two guided modes of different orders using periodic perturbation.

combinations of beamsplitters and phase shifters, one can achieve arbitrary transformations of many path modes.

2.4.1 Mach-Zehnder Interferometers

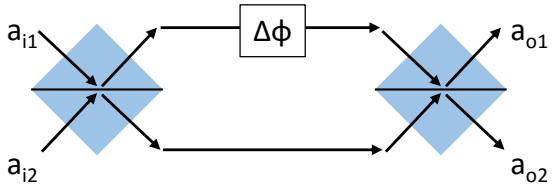

Figure 2.10: **Schematic of a Mach-Zehnder Interferometer.**

The Mach-Zehnder interferometer (MZI) is one of the most commonly used interferometers for switching. MZI's are typically broadband, so they are used for routing many wavelength channels at once or for applications without tunable or narrow linewidth lasers. This consists of a 50:50 beamsplitter, a phase shifter to introduce a phase difference between two arms, and another 50:50

beamsplitter (see Fig. 2.10). The phase difference, $\Delta\phi$, can be achieved through a change in refractive index, Δn, or path length difference, ΔL, as follows:

$$\Delta\phi = \frac{2\pi}{\lambda}\Delta nL = \frac{2\pi}{\lambda}n\Delta L \tag{2.21}$$

This allows one to fully switch the power from one arm to the other. For a non-ideal beamsplitter ($\eta \neq 0.5$) with negligible loss, one can use a transfer matrix calculation to determine the power transfer as a function of phase difference, $\Delta\phi$:

$$\begin{bmatrix} a_{o1} \\ a_{o2} \end{bmatrix} = \begin{bmatrix} \sqrt{\eta} & \sqrt{1-\eta} \\ \sqrt{1-\eta} & -\sqrt{\eta} \end{bmatrix} \begin{bmatrix} e^{-j\Delta\phi} & 0 \\ 0 & 1 \end{bmatrix} \begin{bmatrix} \sqrt{\eta} & \sqrt{1-\eta} \\ \sqrt{1-\eta} & -\sqrt{\eta} \end{bmatrix} \begin{bmatrix} a_{i1} \\ a_{i2} \end{bmatrix} \tag{2.22}$$

Here if power is put in a_{i1}, then the power in the bar-port, a_{o1}, and the cross-port, a_{o2}, can be tuned by the applied phase difference, $\Delta\phi$ (see Fig. 2.11):

$$a_{01}^2 = 2\sqrt{\eta(1-\eta)}\sin^2\left(\frac{\Delta\phi}{2}\right) \tag{2.23}$$

$$a_{02}^2 = 1 - 2\sqrt{\eta(1-\eta)}\sin^2\left(\frac{\Delta\phi}{2}\right) \tag{2.24}$$

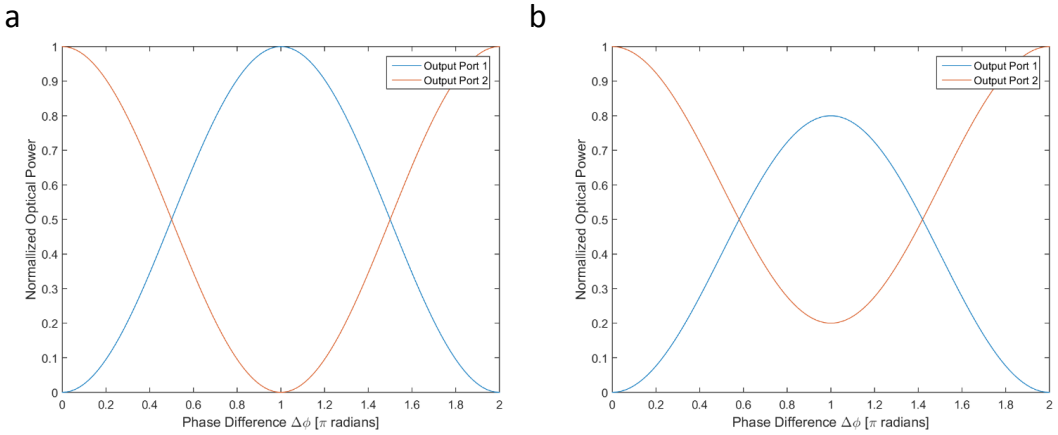

Figure 2.11: **Power transfer in MZI** a) Ideal MZI in which $\eta = 0.5$ b) Non-ideal MZI in which $\eta = 0.2$

If the power is input through a_{i2}, the two outputs are reversed. A π phase shift is necessary to switch all the light from one port to the other. Here, one can see the extinction ratio is related to the splitting ratio, η.

$$Extinction = 10 \log \frac{a_{01}^2}{a_{02}^2} \tag{2.25}$$

We can also define a visibility, V_{mzi}:

$$V_{mzi} = 2\sqrt{\eta(1-\eta)} \tag{2.26}$$

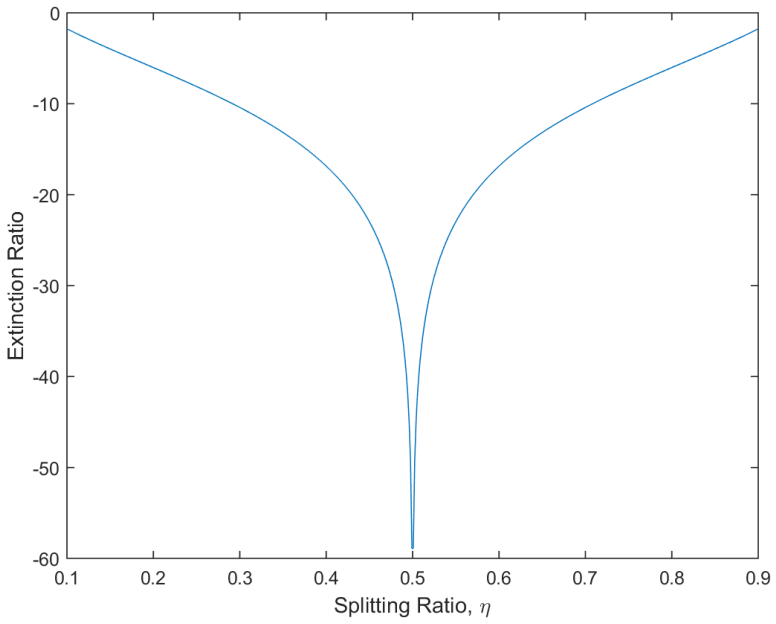

Figure 2.12: **MZI Extinction Ratio (dB scale) as a function of splitting ratio, η.** The maximum value extinction ratio here is limited by the sampling in the plot.

2.4.2 Large Interferometer Networks for Multiplexing Signals

By cascading these 2x2 beamsplitters and phase shifters, we can create larger networks of interferometers to perform tasks such as routing and switching. This can be thought of as multiplexing signals using the path degree of freedom. Multiplexing (De-multiplexing) is a way of combining (separating) many signals together in a shared medium. Large 32x32 switches for reconfigurable path switching has been demonstrated involving 1024 MZI's, and they fit into a compact footprint of 11 mm by 25 mm[3, 19]. Careful design strategies are taken to ensure path-independent insertion loss and that the power consumption remains low regardless of the switching route. The typical extinction ratios which determine the amount of crosstalk between the channels are on the order of 20 dB which are good for optical communications applications.

2.5 Other Degrees-of-Freedom for Multiplexing

2.5.1 Wavelength or Frequency

Optical modes of different wavelengths within the same waveguide can be used as independent parallel optical channels. Wavelength-division multiplexing (WDM) has been used in optical communication for many years. Specifically, optical interconnects using WDM provide a high bandwidth and low power consumption solution . The nanophotonic platform uses wavelength-sensitive structures such as microring resonators, arrayed waveguide gratings and MZI interleaver structures to multiplex and demultiplex approximately 10 wave-

length channels with 20 dB crosstalk [1].

2.5.2 Transverse Spatial Mode

Similarly, the transverse spatial modes within a multimode waveguide can be used as independent parallel optical channels as well. Recently, mode-division multiplexing on the nanophotonics platform has become an active area of research in order to further scale the optical interconnects without the need for additional laser sources[20, 21, 22]. The laser is typically the most power-consuming component and the dominant packaging cost in silicon photonic tranceiver systems. Typically, the transverse spatial modes have been considered a nuisance in photonic device design because unwanted conversion to these higher order modes typically leads to unwanted crosstalk and loss that degrades the performance of the typical path interferometer. However, with careful design, nanophotonic structures on a high index contrast waveguide platform can be used to convert between modes in a controlled way[23, 24, 25, 26]. We use these principles to design a mode-division multiplexing platform for quantum interference in this dissertation.

2.5.3 Time

Time-division multiplexing schemes which utilizes fixed delays between different channels to multiplex signals have been proposed[27, 28]. Typically, these delays require long lengths of waveguides that translate into a time delay. These delay lines can introduce significant loss. Alternatively, short pulses with low

timing jitter could be used as well. However, this requires complex configurations of high speed electronics.

2.5.4 Polarization

Due to the nature of the quasi-TE and quasi-TM modes on the waveguide platform, this degree-of-freedom cannot be treated in the same way polarization is treated in free-space optics. In a rectangular waveguide, all the TE and TM modes have different propagation vectors and effective indices depending on the refractive index profile as we discussed previously. One can think of the TE and TM modes as additional transverse spatial modes with a different polarization. To convert between different polarizations one must create a non-zero overlap between the two polarizations which typically requires an asymmetric perturbation[29]. One can also work with square waveguides in which these indices are the same, but one must control the coupling between the two polarizations very carefully. This tends to only be used in low-index contrast waveguides where this conversion remains small.

2.6 Visible-Wavelength Platform

2.6.1 Low-loss Silicon Nitride

Traditionally integrated nanophotonics has used silicon waveguides because it was developed originally to be fabricated alongside electronics using conventional complementary metal-oxide-semiconductor (CMOS) fabrication tech-

nologies. However, the bandgap of silicon is around 1 eV, so it begins to absorb at wavelengths below 1100 nm. Many materials begin to absorb in the visible wavelengths. In this dissertation, we use a silicon nitride waveguide platform which has a transparency window from 400 nm - 7 μm.

However, the overall loss is a combination of both material absorption and propagation loss which is a result of the lithography and etching process. Low loss high confinement silicon nitride structures have been demonstrated for applications such as biological particle and ion trapping, nonlinear optics, quantum optics, and spectroscopy in a wide wavelength range from the visible to mid-infrared. Losses as low as 0.0043 dB/cm in the near-infrared wavelength range and 0.6 dB/cm at 600 nm have been reported for low-pressure-chemical-vapor deposited silicon nitride [30, 31]. We will show how it can be used for quantum optics at 808 nm and optogenetic neural excitation at 473 nm. For quantum optics, low optical losses are necessary due to the inefficiency of single photon sources and the inability to amplify signals. For optogenetics neural excitation the loss limitations are not as stringent. However, the shorter wavelength range, 473 nm, has much stronger scattering losses from sidewall roughness along the waveguides due to Rayleigh scattering, which is proportional to $\frac{1}{\lambda^4}$. Etched sidewalls have a surface roughness of around 5 nm, which can be improved to about 1 nm with multipass electron beam lithography techniques[30].

2.6.2 Thermo-Optic Phase Tuning

The thermo-optic effect can be used to tune the phase of light on the silicon nitride platform. Although smaller than in silicon, the thermo-optic coefficient of

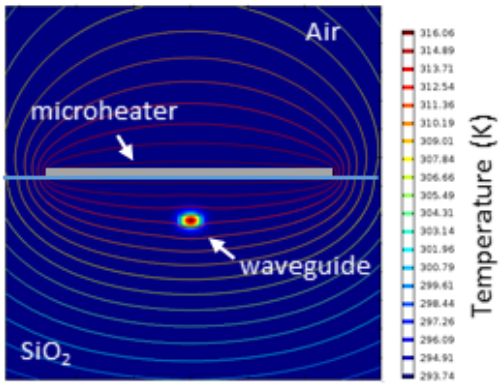

Figure 2.13: **Thermo-optic phase shifter.** Numerical simulation of temperature gradient from the microheater overlaid with the optical mode of a waveguide.

silicon nitride, $\frac{dn}{dT} \sim 4 \times 10^{-5} K^{-1}$ can create large phase shifts in compact structures without inducing loss. The typical switching times, τ, are in the microsecond timescales. For applications that can tolerate moderate frequencies (50-100 kHz) and operation powers (10 mW), thermo-optic tuning is ideal.

Typically, an integrated microheater is a resistive element that sits above the cladding of the waveguide and uses joule heating to induce a temperature change within the waveguide (see Fig. 2.13). There is a minimum distance required to ensure the optical mode does not interact with the metal which will lead to absorption. Typically the temperature change, ΔT_π, needed is about 10-30 K for a π phase shift which is necessary to switch the light between two ports of a MZI (see Eq. 2.27). The temperature of the heater is proportional to the power dissipated by the resistor.

$$\Delta T_\pi = \frac{\lambda}{2L\frac{dn}{dT}} \tag{2.27}$$

We can denote the power to give this π phase shift as P_π which is proportional to the thermal conductance of the waveguide, G [32]. However, the switching

speed, τ, is inversely proportional to the G by a factor H, heat capacity of the waveguide structure [32].

$$P_\pi = \Delta T_\pi G \tag{2.28}$$

$$\tau = \frac{H}{G} \tag{2.29}$$

$$FOM = P_\pi \tau = \Delta T_\pi H \tag{2.30}$$

This leads us to a Figure of Merit (FOM) for a thermo-optic heater that is related to the temperature change required and the heat capacity, H [32]. This heat capacity is effectively proportional to the entire heated structure's volume. This includes the distance of the heater to the waveguide and the waveguide's volume. The length is canceled out by the denominator of ΔT_π.

There is a trade-off between the power, P_π, and the switching time, τ. Basically, for efficient heating of the waveguide, the heat should not be able to escape quickly. However, that is exactly necessary for fast operation. For low power and fast switching speeds, the FOM should be small. For the same material platform and wavelength, the way to achieve this is a smaller heat capacitance, H. This can be achieved by bringing the microheater closer to the waveguide and minimizing the cross-section of the waveguide. There are also new developments in light-recycling that can allow for multiple passes through the phase shifting area without increasing the heating volume.

For practical implementation of these microheaters, the major concern is the amount of power that can be delivered before breakdown of the microheater. It is suspected that the breakdown occurs due to poor deposition quality of the heaters which leads to electromigration at high currents. The length, height, and width of the microheater is determined by the resistance required for moderate

current and voltage operation, limited by the breakdown phenomena and the power supply.

In this work, we used both electron-beam evaporated nickel and sputtered platinum integrated microheaters. The breakdown powers were approximately 600 mW for the nickel and 1.5-2 W for the platinum. It is suspected that the sputtered platinum was better quality due to the lower achievable deposition pressures and chamber cleanliness in our particular facility.

2.7 Fabrication

The typical process flow for the thermally tuned silicon nitride platform is shown in Fig. 2.14. We start with a silicon wafer that has been thermally oxidized to have a layer from 2-5 μm thick of buried silicon dioxide which will serve as the bottom cladding for the waveguide. Next, we deposit low-pressure chemical vapor (lpcvd) silicon nitride which will serve as the waveguide layer. We choose lpcvd silicon nitride because it is the closest to stoichiometric silicon nitride with few impurities which has been demonstrated to show the lowest losses from the visible to the mid-infrared wavelengths. Then, we pattern the photonic structures using ma-N 2400 series resist and electron beam lithography. Finally, we etch the waveguides using $CHF_3 : O_2$ gases in a ratio of 52:2. We anneal the silicon nitride waveguides in a 1200 °C nitrogen ambient furnace which removes residual impurities. Next, we deposit a thin layer of high temperature lpcvd silicon dioxide to ensure the best quality silicon dioxide cladding is near the surface of the waveguide. Finally, we deposit a thicker layer approximately 2 μm of plasma enhanced chemical vapor deposited silicon dioxide to

complete the top cladding layer of the waveguide.

The integrated microheaters are patterned using a lift-off process which uses LOR and SPR resists and contact photolithography. The metal layer is a double layer process in which first NiCr, Ni, Cr, or Pt are used to form the microheater above the waveguide, and next, routing wires and contacts are formed using a low-resistivity metal such as Al. A single layer metal process can also be used with a metal with moderate resistivity like Pt. The microheaters are formed with a highly resistive narrow width section, and the routing wires can be formed using lower resistance wider sections of the same metal.

Finally, if inverse tapers are being used, for efficient coupling we use an etched facet process in which instead of dicing through the waveguides, the cladding is etched about 3 μm away from the end of the waveguides.

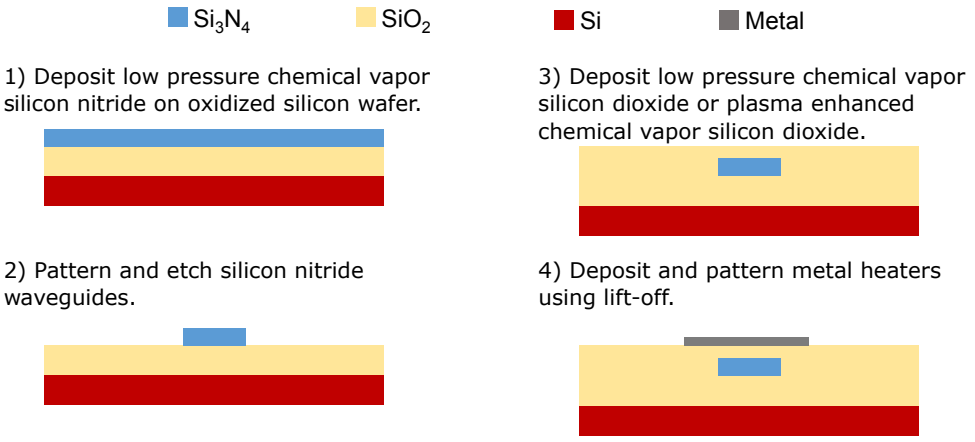

Figure 2.14: **Basic fabrication process flow for thermally tuned silicon nitride nanophotonic platform.**

CHAPTER 3

QUANTUM OPTICS

3.1 Introduction

Quantum systems use unique quantum mechanical properties such as superposition and entanglement to dramatically enhance a wide-range of quantum information processing applications such as quantum computing and simulation, quantum communication, and quantum metrology [33, 34, 35]. These systems require proper preparation and manipulation of quantum states. There are a number of physical implementations being pursued such as photon, trapped ion, superconducting, spin, neutral atoms, and topological systems. In the recent years, superconducting circuits and trapped ions have made significant progress. For example, IBM demonstrated a 16-qubit computer based on superconducting conducting circuits which can perform algorithms for public use. Although these superconducting circuits have been the easiest to implement because they rely on well-developed electronics fabrication, the states have short coherence times and require low temperatures around 20 mK[36].

Developing scalable photonic quantum systems is an active area of research. Information using single photons can be encoded in many different degrees of freedom of the optical field. Additionally, communication systems already rely on optics for long-haul information transport through fiber optics and more recently, optical interconnects in data centers. The main advantage of these single photon systems is that they are relatively free of noise leading to long coherence times, compared with other systems[33]. This means that they are less affected by their environment which can cause errors in computation or communica-

tion. However, this comes at price in that it is difficult for one photon to act on another photon and requires a strongly non-linear medium. Despite these limitations, many quantum applications are being pursued actively and drive the need for scalable photonic quantum systems.

3.1.1 Integrated Photonic Quantum Systems

The integrated nanophotonics platform for quantum optics dramatically improves the efficiency, cost, scalability, flexibility and performance of photonic quantum systems[37]. It takes table-top optics that are large, bulky, and unstable and miniaturizes them to a chip which is on the millimeter-scale, more stable, and power efficient. There are three main components to a photonic quantum system: single photon sources, transformations using interferometers, and single photon detectors.

Currently deterministic single photon emitters are the current bottleneck in scaling up photonic quantum systems. A single photon emitter emits exactly one photon into a specific optical mode on-demand. The goal is to be able to generate many of these single photons that are indistinguishable which will be necessary for quantum interference. This can be done using a variety of methods such as atomic transitions from cold atoms, fluorescent atomic defects, and quantum dots[38]. However, the most common method that is used is by heralding one of two photons that are produced during a nonlinear process such as spontaneous parametric downconversion and spontaneous four-wave mixing. However, since this scheme is inefficient due to its probabilistic nature. Therefore, there is active research in improving the photon purity, efficiency,

and indistinguishability of single photon sources based on deterministic emitters.

To perform transformations on a large set of single photons, current photonic quantum systems rely on path-encoded interferometers as were discussed in Chapter 2. However, multiplexing schemes in different degrees-of-freedom are currently being used to encode more information per photon because it is a scarce resource. Previously, quantum multiplexing on an integrated platform had been limited to time-bin and polarization-bin encoding because all the building blocks based on active switching was available[39, 40]. Frequency encoding has been actively pursued for many year because this would allow us to take advantage of wavelength-division multiplexing from the classical communications domain[41, 42, 43, 44]. However, it requires large nonlinear effects. Despite these challenges many groups have made significant progress, making frequency encoding a viable option. In this dissertation, we utilize the transverse spatial mode to increase the dimensionality of photonic quantum systems. We show that simple geometric design of the waveguide will allow conversion and interference between different modes.

The final component of the photonic quantum system is a single photon detector with a high detection efficiency, low dead time, and low timing jitter. These single photon detectors are primarily based on avalanche photodiodes and superconducting nanowires[45, 46]. The avalanche photodiodes are based on silicon technology and are limited to visible wavelengths. The superconducting nanowires can operate from the visible to the mid-infrared wavelengths. However, they need to be cooled to 1.5-4K, which is a disadvantage.

Quantum Computing and Simulation

Quantum computation and simulation demands the most scalability in terms of resources of quantum systems. In 2001, a scheme for linear optical quantum computing requiring only single photon sources, basic linear optical components, and detectors was proposed[10]. There are also cluster state quantum computing schemes that utilize large entangled states of qubits[42, 47]. In general, quantum computation requires preparation of stable qubits (logical quantum bits), manipulation of these bits with error correction, and measurements. All of this needs to be done on a massive scale for universal quantum computing.

The major issue with quantum system technologies is they need to overcome decoherence, or coupling to their environment, which results in errors. There has been a lot of work towards error-correcting methods based on redundant coding[48]. For each logical qubit there is multiple error-correcting qubits necessary to store extra information. One can make measurements on the error correcting qubits without measuring the logical qubit which would affect its state. This leads to fault-tolerant computing. However, this significantly increases the number of qubits necessary. There is also a limit to adding extra qubits for fault tolerance because it may introduce additional errors to a point that this is prohibitive.

Peter Shor's algorithm for factoring prime numbers is an example in which a quantum computer is expected to surpass a classical computer in terms of computational power [33, 48]. There have been estimates that for every qubit, or logical quantum bit, 3600 additional physical qubits are required for error-correcting[49]. To factor a 2000 bit prime number, the size that is typically used

in RSA encryption, would require 4000 logical qubits which results in 20 million physical qubits. To date the largest number that has been factorized using a photonic quantum system has been the number 21, so there is a significant need in scaling up quantum systems[50].

Alternatively, one could scale up to build systems of hundreds of qubits without error correction, which would still be useful for quantum simulation. Quantum simulation needs 50-100 qubits to simulate phenomena in the fields of chemistry, material science, and any other quantum system[48, 51]. Only recently, in May 2017, boson sampling was demonstrated for 5 photons[52].

Quantum Communication

Quantum key distribution systems theoretically provides perfect security for transmission of encryption keys and are already available commercially[34]. However, a current limit for quantum communication is the loss along the fiber during long-haul transmission. Due to the quantum no-cloning theorem, a signal cannot simply be amplified limiting transmission to only hundreds of kilometers. A quantum repeater must be used to regenerate a quantum state without introducing any measurement that might destroy it[35, 53, 54].

Quantum Metrology

Quantum metrology uses enhanced sensitivity of quantum states to improve precision measurements in biological systems, lithography, and atomic clocks[48]. This includes operations as large as the Laser Interferometer Gravitational-Wave Observatory (LIGO) which uses the detection of squeezed

light to detect gravitational waves[35].

3.2 Photonic Quantum States

A single photon can be thought of as a single excitation of the fundamental mode of the quantized electromagnetic field. This photon state can be defined by any degree of freedom (path, transverse spatial field, frequency, and time) that was discussed in Chapter 2. These are the states that can be manipulated and transmitted for quantum computation and communication.

The Hamiltonian of this quantized electromagnetic field system has a form that is similar to the simple harmonic oscillator, and therefore the number state representation can be used [55]. In the number state representation, using Dirac notation, $|n\rangle_j$ represents a single frequency quantized field containing n photons, and j identifies its mode in a particular degree of freedom. For example, $|2\rangle_{TE0}$ means the state that contains two photons in the fundamental TE mode of a waveguide. The creation, $a^\dagger$, operators can be used to convert between number states using the following[55]:

$$|n\rangle = \frac{1}{(n!)^{\frac{1}{2}}}(a^\dagger)^n|0\rangle \tag{3.1}$$

3.2.1 The Quantum Bit

An example of a useful quantum state is the quantum bit, or qubit. In classical computing, information is stored in 1's and 0's. However, the superposition principle of quantum mechanics allows one to store information in qubits which

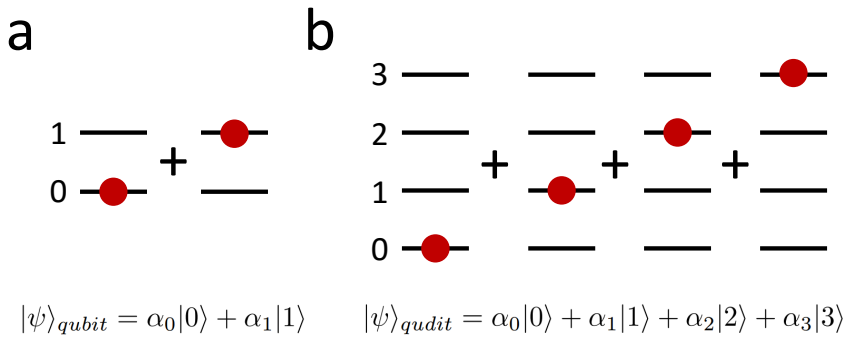

Figure 3.1: **Visual representation of a) qubit and b) qudit.**

allow the state to be both 1 and 0 simultaneously (see Fig. 3.1). The state, $|\psi\rangle$, of a qubit can be represented as follows:

$$|\psi\rangle_{qubit} = \alpha_0|0\rangle + \alpha_1|1\rangle \tag{3.2}$$

where α_0 and α_1 represent the probability amplitude coefficients of each pure state. The normalization condition requires that all the probabilities add to 1:

$$|\alpha_0|^2 + |\alpha_1|^2 = 1 \tag{3.3}$$

In a multilevel system with d levels, one can create a qudit with probability amplitude coefficients α_0, α_1, α_2, and α_3:

$$|\psi\rangle_{qudit} = \alpha_0|0\rangle + \alpha_1|1\rangle + \alpha_2|2\rangle + \alpha_3|3\rangle \tag{3.4}$$

These states can be created in many different ways using the photonics system. For example, the simplest case is a waveguide fundamental TE0 mode with either 0 or 1 photon.

$$|\psi\rangle_{qubit} = \alpha_0|0\rangle_{TE0} + \alpha_1|1\rangle_{TE0} \tag{3.5}$$

Similarly, a photon in superposition among the higher order modes (TE0, TE1, TE2, and TE3) of a multimode waveguide could be represented in the following way.

$$|\psi\rangle_{qudit} = \alpha_0|1\rangle_{TE0} + \alpha_1|1\rangle_{TE1} + \alpha_2|1\rangle_{TE2} + \alpha_3|1\rangle_{TE3} \tag{3.6}$$

3.2.2 Unitary Transformations using a Beamsplitter

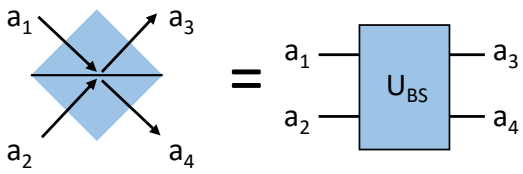

Figure 3.2: **Unitary transformation using a beamsplitter.**

Quantum computation and communication protocols rely on unitary transformations of quantum states. A unitary transformation ensures that the transformation conserves the total probability, where U and $U^\dagger$ represent the unitary matrix and its adjoint and $U^\dagger U = UU^\dagger = I$. The beamsplitter is a commonly used 2x2 unitary transformation in optics. Any arbitrary NxN unitary transformation can be performed with a combination of 2x2 beamsplitters and phase shifters [56]. In the quantum formalism using Dirac notation, the classical electromagnetic field amplitudes from Eq. 2.16 can be replaced by creation operators, so a unitary operation can be represented by U_{BS}:

$$\begin{bmatrix} a_1^\dagger \\ a_2^\dagger \end{bmatrix} = U_{BS} \begin{bmatrix} a_3^\dagger \\ a_4^\dagger \end{bmatrix} = \begin{bmatrix} \sqrt{\eta} & \sqrt{1-\eta} \\ \sqrt{1-\eta} & -\sqrt{\eta} \end{bmatrix} \begin{bmatrix} a_3^\dagger \\ a_4^\dagger \end{bmatrix} \tag{3.7}$$

We can now use the creation operator $a_j^\dagger$ to represent a photon created in mode j. We will represent the input modes before the beamsplitter by a_1, a_2, the output modes after the beamsplitter a_3, a_4. However, these modes can represent any type of mode such as transverse spatial modes, which we will show in the next chapter.

3.2.3 Hong-Ou-Mandel Interference

The most basic example of quantum interference is that of two single photons. Hong-Ou-Mandel interference is the quantum interference of two indistinguishable photons on a beamsplitter[57]. Here we use the configuration from Fig. 3.2.

When a single photon is incident on either port, the state can be written as:

$$|1\rangle_1|1\rangle_2 = a_1^\dagger a_2^\dagger|0\rangle|0\rangle \tag{3.8}$$

From Eq. 3.8 and the transformation from Eq. 3.7, substituting for a_1 and a_2:

$$\begin{aligned} a_1^\dagger a_2^\dagger|0\rangle|0\rangle &= (\sqrt{\eta}a_3^\dagger + \sqrt{1-\eta}a_4^\dagger)(\sqrt{1-\eta}a_3^\dagger - \sqrt{\eta}a_4^\dagger)|0\rangle|0\rangle & (3.9)\\ &= (\sqrt{\eta(1-\eta)}a_3^{\dagger 2} + \eta a_3^\dagger a_4^\dagger - (1-\eta)a_4^\dagger a_3^\dagger - \sqrt{\eta(1-\eta)}a_4^{\dagger 2})|0\rangle|0\rangle & (3.10)\end{aligned}$$

We know that the creation operators a_3, a_4 commute if the input states are indistinguishable, which leads to the HOM output state:

$$a_1^\dagger a_2^\dagger|0\rangle|0\rangle = (\sqrt{\eta(1-\eta)}a_3^{\dagger 2} + (2\eta-1)a_3^\dagger a_4^\dagger - \sqrt{\eta(1-\eta)}a_4^{\dagger 2})|0\rangle|0\rangle \tag{3.11}$$

$$|\psi\rangle_{HOM} = \sqrt{2\eta(1-\eta)}|2\rangle_3|0\rangle_4 + (2\eta-1)|1\rangle_3|1\rangle_4 - \sqrt{2\eta(1-\eta)}|0\rangle_3|2\rangle_4 \tag{3.12}$$

In the last two lines we use the relation:

$$a^{\dagger 2}|0\rangle = a^\dagger|1\rangle = \sqrt{2}|2\rangle$$

The term with a_3, a_4 corresponds to the probability amplitude of coincidences, so the probability of coincidence can be written as:

$$P_q(|1\rangle_3|1\rangle_4) = (2\eta-1)^2 \tag{3.13}$$

This means that when $\eta = 0.5$, the probability of coincidence goes to 0. This is assuming that the two photons are distinguishable in every other degree of

freedom (spectral, polarization, etc.). Here we are calculating the output state of the HOM interferometer at 0 path length delay between the two arms.

In the classical case, we get coincidences if both photons are reflected and both photons are transmitted. Essentially, in the case that the two photons are distinguishable, they're creation operators do not commute. One can see from Eq. 3.11, the probabilities of the two cases add:

$$P_{cl}(|1\rangle_3|1\rangle_4) = \eta^2 + (1-\eta)^2 \tag{3.14}$$

As we change the path delay between the two arms and measure coincidences, there is a dip in coincidences at zero path delay compared with large path delays (classical case). The visibility of this dip, known as the Hong-Ou-Mandel (HOM) interference is the following:

$$V_{HOM} = \frac{P_{cl}(|1\rangle_3|1\rangle_4) - P_q(|1\rangle_3|1\rangle_4)}{P_{cl}(|1\rangle_3|1\rangle_4)} \tag{3.15}$$

This shows that when the two path lengths (and all other degrees of freedom of the two photons) are the same and the beamsplitter is 50:50, the visibility should be 1. As we delay the two arms relative to each other, we approach the classical visibility of 0.

For two classical or distinguishable photon pairs, there should be no dip. However, there is a special case limit of the visibility being less than 0.5 for classical beams[58].

Input and output losses for each channel should not affect the visibility because this loss would affect both the classical and quantum probabilities similarly. Basically, the total number of coincidences will be decreased when you lose one of the pair. If there is an asymmetric loss within the beamsplitter itself, there is a possibility of visibility degradation.

3.2.4 Hong-Ou-Mandel Peak

Now, if we send one output of the Hong-Ou-Mandel interferometer through another beamsplitter, we should expect an increase in coincidences after the second beamsplitter. After, the first beamsplitter in the HOM interferometer, there are no coincidences at these arms because the two photons are going together to either one of the inputs together.

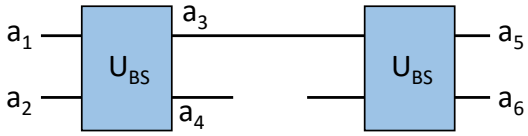

Figure 3.3: **HOM peak configuration.**

From Eq. 3.12, the output state for having the two photons go to either of the two arms is the following:

$$|\psi\rangle_{HOM} = \sqrt{2\eta(1-\eta)}|2\rangle_3|0\rangle_4 - \sqrt{2\eta(1-\eta)}|0\rangle_3|2\rangle_4 \tag{3.16}$$

From this, we can calculate the probabilities of getting two photons in either arm for the HOM, or quantum case, as:

$$P_q(|2\rangle_3|0\rangle_4) = P_q(|0\rangle_3|2\rangle_4) = 2\eta(1-\eta) \tag{3.17}$$

Now if we compare this to the classical case, when have two photons at the same output which means we have a reflection and transmission:

$$P_{cl}(|2\rangle_3|0\rangle_4) = P_{cl}(|0\rangle_3|2\rangle_4) = \eta(1-\eta) \tag{3.18}$$

We should expect an increase in the probability of two photons in the individual

output arms by a factor of 2 in the quantum case as opposed to the classical case:

$$V_{HOMpeak} = \frac{P_q}{P_{cl}} = 2 \tag{3.19}$$

This is known as the HOM peak.

3.2.5 NOON State Interference

Two-photon interference on the MZI

Another interesting example of quantum interference is the NOON state interferometer in which the period in two-photon quantum interference is half that of classical (or 1-photon) interference. This quantum enhanced phase sensitivity is the ultimate precision in estimating phase differences[59].

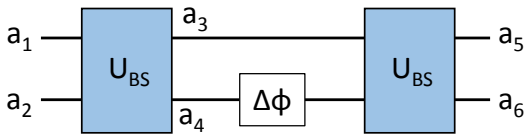

Figure 3.4: **NOON State Configuration.**

We will represent the input modes before the BS1 by a_1, a_2, the modes in the two arms of the MZI by a_3, a_4, and the modes after BS2 by a_5, a_6. The incident state is equivalent to one photon in each input port of BS1:

$$|1\rangle_1|1\rangle_2 = a_1^\dagger a_2^\dagger|0\rangle|0\rangle \tag{3.20}$$

Now, we know from the beamsplitter matrix from before that (assuming

50:50):

$$\begin{bmatrix} a_1^\dagger \\ a_2^\dagger \end{bmatrix} = \frac{1}{\sqrt{2}} \begin{bmatrix} 1 & 1 \\ 1 & -1 \end{bmatrix} \begin{bmatrix} a_3^\dagger \\ a_4^\dagger \end{bmatrix} \tag{3.21}$$

Hence, from Eq. 3.20, substituting for a_1 and a_2 in terms of the modes inside the MZI arms a_3, a_4, we get for the state inside the MZI arms:

$$a_1^\dagger a_2^\dagger |0\rangle|0\rangle = \frac{a_3^\dagger + a_4^\dagger}{\sqrt{2}} \frac{a_3^\dagger - a_4^\dagger}{\sqrt{2}} |0\rangle|0\rangle \tag{3.22}$$

$$= \frac{1}{2}(a_3^{\dagger 2} + a_3^\dagger a_4^\dagger - a_4^\dagger a_3^\dagger - a_4^{\dagger 2})|0\rangle|0\rangle \tag{3.23}$$

We know that the creation operators a_3, a_4 commute, so the two terms in the middle cancel out, leading to the expected state for HOM interference:

$$\frac{1}{2}(a_3^{\dagger 2} + a_3^\dagger a_4^\dagger - a_4^\dagger a_3^\dagger - a_4^{\dagger 2})|0\rangle|0\rangle = \frac{1}{2}(a_3^{\dagger 2} - a_4^{\dagger 2})|0\rangle|0\rangle \tag{3.24}$$

$$= \frac{1}{\sqrt{2}}(|2\rangle_3|0\rangle_4 - |0\rangle_3|2\rangle_4) \tag{3.25}$$

In the last line we have used the relation,

$$a^{\dagger 2}|0\rangle = a^\dagger|1\rangle = \sqrt{2}|2\rangle$$

Now, if we introduce a phase difference ϕ for the lower arm $a_4 \rightarrow a_4 e^{-i\phi}$ with respect to the upper arm a_3, we can write the state incident on BS2 as:

$$\frac{1}{2}(a_3^{\dagger 2} - e^{2i\phi} a_4^{\dagger 2})|0\rangle|0\rangle \tag{3.26}$$

Using the transformation for BS2:

$$\begin{bmatrix} a_3^\dagger \\ a_4^\dagger \end{bmatrix} = \frac{1}{\sqrt{2}} \begin{bmatrix} 1 & 1 \\ 1 & -1 \end{bmatrix} \begin{bmatrix} a_5^\dagger \\ a_6^\dagger \end{bmatrix} \tag{3.27}$$

Eq.3.26 becomes,

$$= \frac{1}{4}\left[(a_5^\dagger + a_6^\dagger)^2 - e^{2i\phi}(a_5^\dagger - a_6^\dagger)^2\right]|0\rangle|0\rangle \tag{3.28}$$

$$= \frac{1}{4}\left[(1 - e^{2i\phi})(a_5^{\dagger 2} + a_6^{\dagger 2}) + 2(1 + e^{2i\phi})a_5^\dagger a_6^\dagger)\right]|0\rangle|0\rangle \tag{3.29}$$

$$= \frac{1}{2\sqrt{2}}\left[(1 - e^{2i\phi})(|2\rangle_5|0\rangle_6 + |0\rangle_5|2\rangle_6)\right] + \frac{1}{2}(1 + e^{2i\phi})|1\rangle_5|1\rangle_6 \tag{3.30}$$

Thus, the probability of coincidence is $\left|\frac{1}{2}(1 + e^{2i\phi})\right|^2 = \cos^2\phi = (1 + \cos 2\phi)/2$. This has a period of π instead of the regular MZI which has a period of 2π.

One photon interference in an MZI

Now we will go through the same line of thought except the input state has a 0 for mode 2:

$$|1\rangle_1|0\rangle_2 = a_1^\dagger|0\rangle|0\rangle \tag{3.31}$$

Hence, from the first beamsplitter using Eq. 3.21 and Eq. 3.31, substituting for a_1 in terms of the modes inside the MZI arms a_3, a_4, we get for the state inside the MZI arms:

$$a_1^\dagger|0\rangle|0\rangle = \frac{a_3^\dagger + a_4^\dagger}{\sqrt{2}}|0\rangle|0\rangle \tag{3.32}$$

$$= \frac{1}{\sqrt{2}}(|1\rangle_3|0\rangle_4 + |0\rangle_3|1\rangle_4) \tag{3.33}$$

In the last line we have used the relation:

$$a^\dagger|0\rangle = |1\rangle$$

Now, if we introduce a phase difference ϕ for the lower arm $a_4 \rightarrow a_4 e^{-i\phi}$ with respect to the upper arm a_3, we can write the state incident on BS2 as:

$$\frac{1}{\sqrt{2}}(a_3^\dagger + e^{i\phi}a_4^\dagger)|0\rangle|0\rangle \tag{3.34}$$

Finally, using the second beamsplitter Eq. 3.27 and Eq. 3.34 becomes,

$$= \frac{1}{2}\left[(a_5^\dagger + a_6^\dagger) + e^{i\phi}(a_5^\dagger - a_6^\dagger)\right]|0\rangle|0\rangle \tag{3.35}$$

$$= \frac{1}{2}(1 + e^{i\phi})(|1\rangle_5|0\rangle_6 + \frac{1}{2}(1 - e^{i\phi})|0\rangle_5|1\rangle_6 \tag{3.36}$$

Thus, the probability of detecting a single photon in the upper arm is $\left|\frac{1}{2}(1 + e^{i\phi})\right|^2 = \cos^2(\phi/2) = (1 + \cos\phi)/2$. This has a period of 2π

CHAPTER 4

MODE-MULTIPLEXING PLATFORM FOR QUANTUM OPTICS

4.1 Introduction

Integrated quantum optics has drastically reduced the size of table-top optical experiments to the chip-scale, allowing for demonstrations of large-scale quantum information processing and quantum simulation[12, 60, 13, 15, 61, 14, 62]. However, despite these advances, practical implementations of quantum photonic circuits remain limited because they consist of large networks of waveguide interferometers that path encode information but do not easily scale. Increasing the dimensionality of current quantum systems using higher degrees of freedom such as transverse spatial field distribution, polarization, time and frequency to encode more information per carrier will enable scalability by simplifying quantum computational architectures[63], increasing security and noise tolerance in quantum communication channels[64, 65], and simulating richer quantum phenomena[66]. These degrees of freedom have previously been explored in free-space and fiber quantum systems to encode qudits and implement higher-dimensional entanglement[67, 68, 69, 70, 71].

Currently, integrated quantum photonic circuits are primarily limited to path encoding information, but the use of a higher-dimensional Hilbert space within each path will increase the information capacity and security of quantum systems[1]. Higher dimensionality allows one to encode more information per photon, relieving resource requirements on photon generation and

[1]Parts of this chapter have been published and adapted from work licensed under CC BY 4.0[72].

detection[64, 65]. Consequently, this leads to more efficient logic gates and noise resilient communications, making quantum systems more scalable and practical.[34, 63] In integrated schemes, a few demonstrations have been developed for polarization [73] and time[74]. In free-space optics, orbital angular momentum and Hermite-Gaussian modes have both been used to encode information within a higher-dimensional space as qudits (d-level logic units)[67, 68, 69, 70, 71]. The higher order waveguide modes in a multi-mode interferometer have been used to passively mix single-mode inputs for quantum interference and transfer polarization and path-encoded states[75, 76]. However, the spatial modes have never been controlled individually to encode quantum information to date[77, 78]. The transverse spatial degree of freedom is an untapped resource that can be manipulated using simple photonic structures and does not require exotic material properties.

In the classical regime, the orthogonal spatial modes of an integrated waveguide have been shown to dramatically scale data transmission rates[20, 21, 79, 22, 80]. A waveguide can support many co-propagating modes, which can be used as parallel channels within a single waveguide. Progress in the field has overcome the challenge of achieving controlled coupling while avoiding unwanted coupling between different modes, for example in bends and tapers[81, 17]. Mode conversion based on waveguide structuring has significant potential in the quantum regime [24, 82, 25].

Here, we demonstrate a scalable platform for photonic quantum information processing using waveguide quantum circuit building blocks based on the transverse spatial mode degree of freedom: spatial mode multiplexers and spatial mode beamsplitters. A multi-mode waveguide is inherently a densely

packed system of spatial and polarization modes that can be coupled by perturbations to the waveguide. We design a multi-mode waveguide consisting of three spatial modes (per polarization) and a nanoscale grating beamsplitter to show tunable quantum interference between pairs of photons in different transverse spatial modes. We also cascade these structures and demonstrate NOON state interferometry within a multi-mode waveguide. We show that interference between different transverse spatial waveguide modes and active tuning can be achieved with high visibility using this platform. These devices have potential to perform transformations on more modes and be integrated with existing architectures, providing a scalable path to higher-dimensional Hilbert spaces and entanglement.

4.2 Hong-Ou-Mandel interference using transverse spatial waveguide modes

In order to show the potential utility of the integrated transverse spatial degree of freedom for scalable quantum information processing, we demonstrate Hong-Ou-Mandel (HOM) interference between two different quasi-transverse electric (TE) waveguide modes (TE0 and TE2). HOM interference is a useful proof of principle because it is the basis of many other quantum operations such as higher-dimensional entanglement, teleportation, quantum logic gates, and boson-sampling[12, 60, 13, 15, 83, 70, 71]. In the original HOM experiment, a path beamsplitter is used to combine two originally orthogonal paths of two single photons, making them indistinguishable. The probability amplitudes of the two cases that contribute to detection of the two photons in coincidence de-

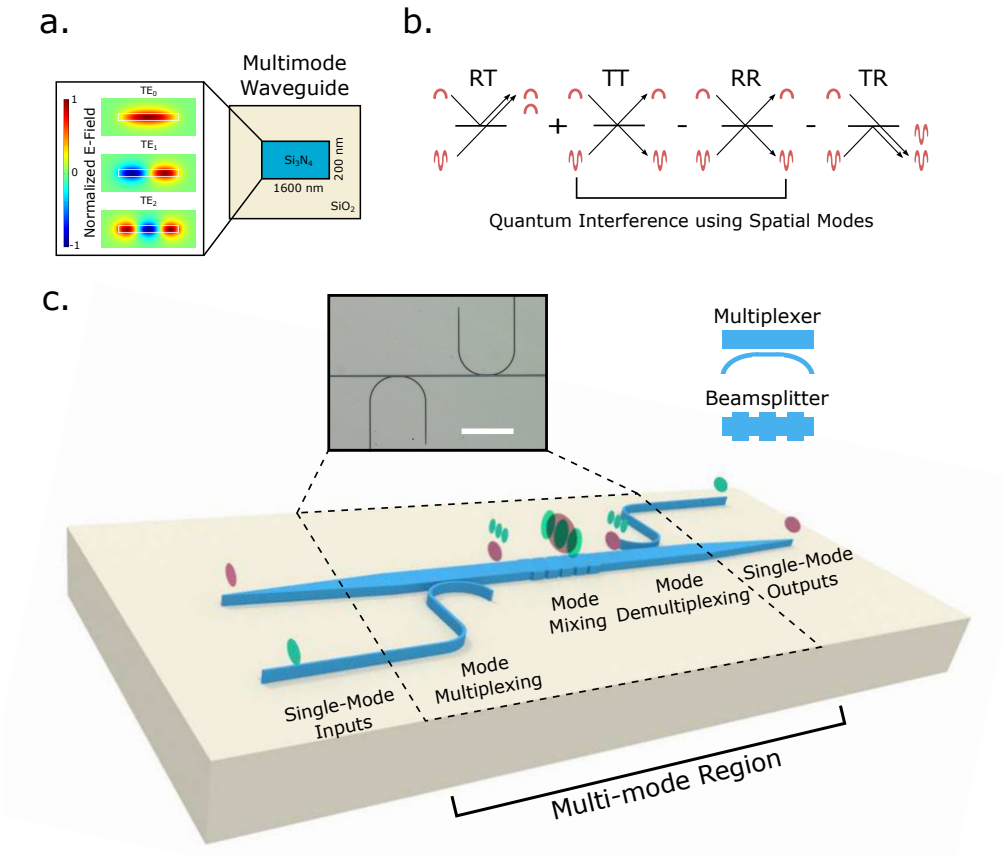

Figure 4.1: **Quantum Interference using a Spatial Mode Beamsplitter.** a) Simulation of transverse spatial modes in a multi-mode waveguide. b) Schematic shows interference between two indistinguishable photons incident on the two input ports (or modes) of a beamsplitter, where the two input ports are the two spatial modes of a waveguide (TE0 and TE2). The four cases of probability amplitudes in which TE0 and TE2 are reflected (R) or transmitted (T) are added or subtracted based on the unitary transformation of a beamsplitter. The arrows indicate whether the photons remain in the same mode or convert to the other mode. The destructive interference of the two cases that result in coincidences (RR and TT) leads to the characteristic HOM interference. c) Schematic showing chip implementation of spatial mode multiplexing (asymmetric directional coupler) and spatial mode beamsplitter (nanoscale grating). The colors indicate the mode order within the multi-mode region of the device (red is TE0, green is TE2). The color also shows the path that transfers single-mode inputs and outputs to the different spatial modes within the multi-mode waveguide. Wavelength (808 nm) and polarization (TE) are identical within each path. The inset shows a microscope image of the device. Scale bar is 160 μm.

structively interfere owing to the bosonic nature of photons, if the two paths are indistinguishable.[57] As an example, we consider a silicon nitride multi-mode waveguide with a sub-micron cross-section containing six modes: three spatial modes per polarization (see Fig. 4.1a). In our experiment, we replace the path beamsplitter with a spatial mode beamsplitter and replace the two paths with two spatial modes within a multi-mode waveguide (see Fig. 4.1b). The spatial mode beamsplitter couples two different spatial modes, resulting in a superposition of the two spatial modes. Mode coupling leads to interference within the waveguide between the cases in which both photons remain in their original modes or both couple to opposite modes (cases RR and TT in Fig. 4.1b). Visibility of the interference in coincidences is a measure of the equal splitting in the beamsplitter and indistinguishability of the two paths in every degree of freedom including transverse spatial mode.

The key building blocks required to demonstrate HOM interference are a spatial mode multiplexer for generating the different spatial modes and a spatial mode beamsplitter for interfering the spatial modes, which both rely on selective mode coupling by phase-matching in our design. The spatial mode multiplexer allows us to generate orthogonal spatial modes within the multi-mode waveguide without cross-talk between the modes, which would reduce the interference visibility. We couple pairs of photons from a spontaneous parametric downconversion (SPDC) source into single-mode silicon nitride waveguides that couple into a multi-mode waveguide (see Methods and Fig. 4.1c). Finally, the photons are sent to the spatial mode beamsplitter where they are equally split between the two modes, coupled into single-mode output waveguides, and the fundamental mode fields are detected as coincidences. We use a silicon nitride platform because the high core-cladding (Si_3N_4/SiO_2) index con-

trast allows one to strongly vary the propagation constants of different spatial modes by varying the waveguide dimensions, which is essential for selective mode coupling. The silicon nitride platform is attractive for integrated quantum information processing because its transparency window spans the visible to mid-infrared wavelength range and has been used to demonstrate non-classical light sources[84, 85].

4.3 Selective mode coupling by phase-matching

To demonstrate the spatial mode multiplexer, we use an asymmetric directional coupler to selectively couple the fundamental mode in a single-mode waveguide to a specific higher-order mode in an adjacent multi-mode waveguide. The asymmetric directional coupler uses two different waveguide widths to phase-match light propagating in different modes within adjacent waveguides, allowing for efficient coupling.[20, 21, 79, 22] In Fig. 4.2a, the horizontal red line indicates where the effective indices of different higher-order modes in waveguides of different widths match. For example, to excite the TE2 mode in the multi-mode waveguide using the TE0 mode in a single-mode waveguide with 420 nm width, we choose the multi-mode waveguide width of 1.6 μm.

To demonstrate the spatial mode beamsplitter, we use a nanoscale grating structure to selectively couple different higher-order spatial modes within a multi-mode waveguide. The period of the grating structure provides a momentum change that accounts for the phase mismatch between the two different spatial modes[86]. In Fig. 4.2a, the vertical red line indicates the phase mismatch (Δn_{eff}) between modes within a single waveguide, $\Lambda = \lambda/\Delta n_{\text{eff}}$ where Λ is

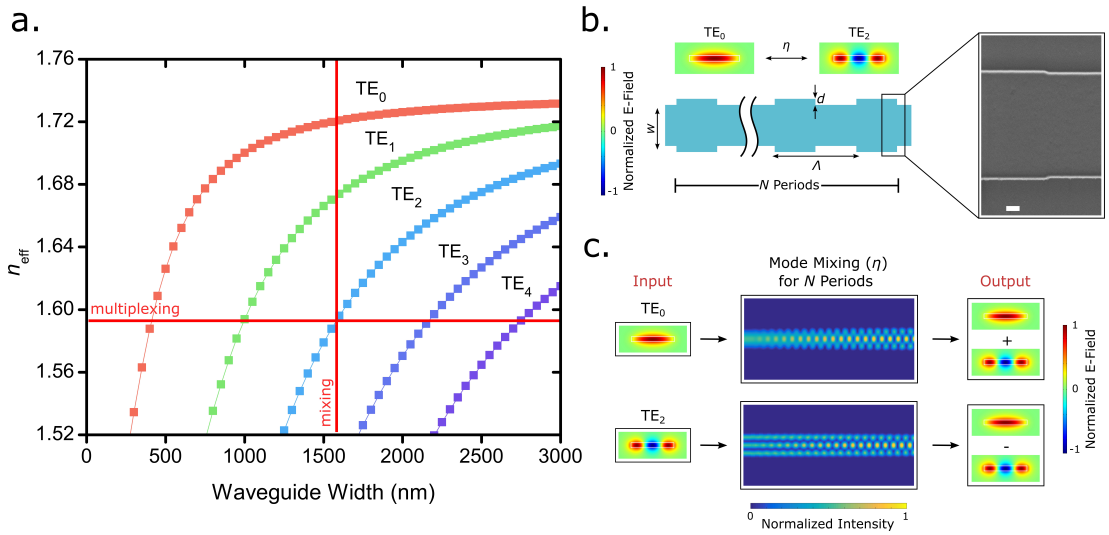

Figure 4.2: **Design of Spatial Mode Beamsplitter.** a) Si_3N_4 dispersion for a multi-mode waveguide with 190 nm height. Horizontal red line shows phase-matching for waveguides with different widths for spatial mode multiplexing. Vertical red line shows phase-matching between modes in a single waveguide for the spatial mode beamsplitter. b) Symmetric grating structure for coupling the TE0 and TE2 modes. The period is defined by the difference in effective index between the modes in a particular waveguide. The period (Λ) is 6.675 μm, and grating depth, d, is 24 nm. The width, w, is 1600 nm and height is 190 nm. Inset: SEM of fabricated grating structure. Scale bar is 200 nm. c) Simulation of mode conversion in a 50:50 splitter for $\eta = 0.5$, where $N = 20$ periods and all other dimensions are the same as in b.

the period of the grating, λ is the wavelength, and n_{eff} is the effective index of the mode. For example, to couple TE0 and TE2, $\Delta n_{\text{eff}} = 0.12$ and $\Lambda = 6.675$ μm. We define the splitting ratio, η, as the probability of coupling to the same mode, and 1-η as the probability of coupling to the opposite mode. This splitting ratio can be tuned from 0 to 100% if the two modes are perfectly phase-matched. This splitting ratio (η) depends on the coupling coefficient (κ) determined by the overlap of the two modes within the perturbed region (grating depth, d) and

the length of the coupling interaction (or the number of periods, N) as follows: $\eta = \cos^2(\kappa N)$ (see Fig. 4.2b and Eq. 2.15). We use Finite Element Method (FEM) and EigenMode Expansion to determine the phase-matching and splitting ratios. Figure 4.2c shows a simulation of a 50:50 coupler between TE0 and TE2. Beamsplitters with tunable splitting ratio are crucial building blocks for photonic quantum simulation circuits[51, 13, 15] and for reconfigurable quantum circuits for quantum metrology and processing[60].

We use silicon nitride waveguides to implement the spatial mode multiplexer and spatial mode beamsplitter. The device has inverse tapers (~170 nm) to mode match to 2 μm spot size of tapered fibers. The single-mode waveguides are 190 nm tall and 420 nm wide. The single-mode waveguide is tapered adiabatically (100 μm long taper) to the multi-mode waveguide, which is 190 nm tall and 1600 nm wide. We use COMSOL and FIMMWAVE software packages to simulate the mode profiles and coupling. The asymmetric directional coupler has a coupling length of 18 μm between the single-mode and multi-mode waveguide. The perturbation needed to couple the modes in the multi-mode waveguide is quite small, about 24 nm, in order to remain within the weak coupling regime, but large enough to yield reasonable device lengths. For gratings with 24 nm depth, the coupling coefficient is ($\kappa = 0.041$) per period. The simulation shows approximately 50:50 coupling for N=20, corresponding to a device length of about 133 μm for our specific geometry. We estimate the loss in the device excluding coupling losses to be 0.2 dB. To characterize the on-chip beamsplitters and fiber beamsplitters, the classical splitting ratios (η) were measured using an 808 nm diode laser source.

To fabricate the device, we deposit 190 nm of low-pressure chemical vapor

silicon nitride on a silicon wafer with 4 μm of thermal oxide. Then, we pattern with electron beam lithography and etch the waveguides. We finally clad the devices with 300 nm of high temperature oxide and 2 μm of plasma enhanced chemical vapor deposited silicon dioxide. For the cascaded device with the integrated phase shifter, we fabricate the heater (50 nm Ni) and contact pads (200 nm Al) using a metal lift-off process.

4.4 HOM Experimental Setup

The Hong-Ou-Mandel interference experiment consists of three main parts: a spontaneous parametric downconversion (SPDC) source, the interferometer chip, and coincidence detection (see Fig. 4.3).

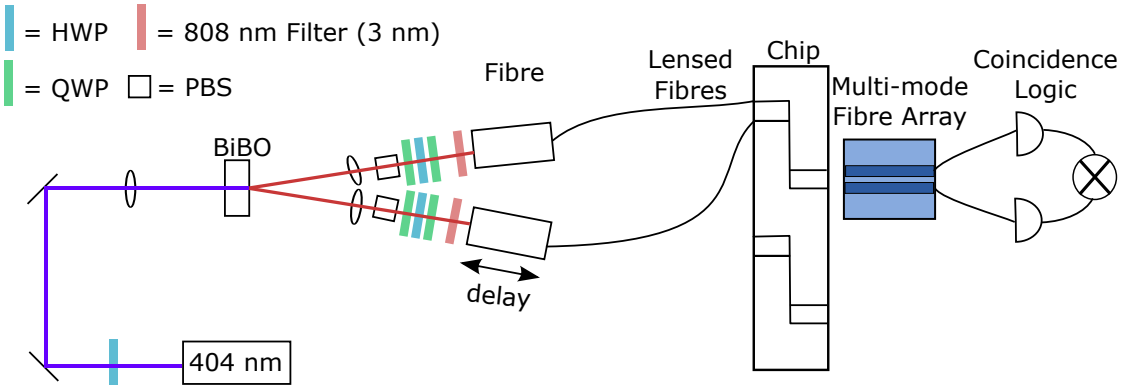

Figure 4.3: **Spontaneous Parametric Down Conversion (SPDC) source and coincidence counting setup.** The photon pair source is coupled to the chip using lensed fibres and coupled to the coincidence counting setup using a fibre array. The polarization is filtered using a series of a half-wave plate (HWP), quarter-wave plate (QWP), and polarizing beamsplitter (PBS).

4.4.1 Spontaneous Parametric Downconversion Source

We use a Type I non-collinear spontaneous parametric downconversion source which generates a pair of photons with half the energy of a photon from a pump source using a second-order nonlinear process[87]. Due to momentum conservation, the pairs of photons are emitted at an angle along a cone. Here we use a 404 nm diode laser to pump a BiBO (Bismuth Borate, Newlight Photonics) crystal that produces a 3° cone with photon pairs at 808 nm. We use one lens to focus the laser onto the crystal. We collect the pair of photons parallel to the table using a fiber coupler assembly that consists of two stages sitting on top of one another. The top stage aligns an aspheric lens to the collecting 780 HP fiber which is used to match the generated photon beam to the mode diameter of the fiber, 5 μm. This sits on top of a larger stage that moves the entire assembly to correct its position along the generated SPDC cone.

To produce a pair of indistinguishable photons, our collection optics must filter at the correct position along the cone and correct for any changes in polarization as the pairs travel within the fibers. The two arms have full polarization control using a set of quarter-half-quarter waveplates and a polarization beamsplitter for further filtering. Finally, we use a set of narrow linewidth (3 nm) filters centered at 808 nm to help filter the same wavelength photons from the cone. Optimizing the angle on these filters is essential because it determines the wavelength that is transmitted.

The alignment of the setup is done by back-propagating red lasers through the fiber coupler assemblies at the 3° angle and intersecting them at the center of the BiBO crystal. We use one of these arms as a delay with a 6 mm range. The delay must be large enough to account for any mismatch in path lengths before

the beamsplitter and also be large enough to cover the entire coincidence dip. The SPDC source HOM visibility was characterized using a single-mode fibre beamsplitter, and we measured a visibility of 92 ± 1.9% and coherence width of 194 ± 10 μm. We attribute this reduced visibility primarily to spectral differences between the two arms. With 60 mW of input laser power, we produced a source pair rate of ~ 9000 counts per second through the fiber beamsplitter which introduced some loss.

4.4.2 Coupling to the Interferometer Chip

The two photons are coupled into the two inputs of the interferometer chip using lensed fiber. It is essential to have good coupling from the source because amplifiers cannot be used in these types of experiments. Here we use 780HP lensed fibers (Oz Optics) with a 2 μm spot size which are mode-matched to the inverse tapers. For optimal coupling, we use two input stages adjacent to one another to have three degrees of freedom of alignment to the input of the chip. Finally, we use a butt-coupled multimode fiber array to collect the photons from the chip to send to the coincidence logic.

4.4.3 Coincidence Detection

After the interferometer, the two photons are sent to the coincidence logic detection system. This consists of two single photon counting modules (SPCM-AQRH, Excelitas). Each SPCM consists of an avalanche photodiode that triggers a TTL pulse when a photon is incident. These pulses are sent to the coincidence

logic (Roithner TTM8000). When a pulse is registered on either channel, if another pulse is registered on the other channel within a certain time window, a coincidence is registered. In our case, the coincidence time window, τ_c, is 2 ns. Since our signal depends on these coincidences, care must be taken to minimize accidental coincidences that occur randomly between two signals. The accidental coincidence count rate, c_{acc} can be calculated from the single count rates, n_1 and n_2 on either arms: $c_{acc} = 2n_1n_2\tau_c$.

To optimize the visibility of the HOM interference, we optimize the coincidence rate with respect to this accidental count rate. This is achieved by controlling the polarization, wavelength filter angle, and fiber coupler position, so that the two photons being coupled from the source are indistinguishable in every degree of freedom. It is important that once counts are detected, to check that the power dependence of the coincidences are linear because for every high energy photon a single pair should be generated. Multiphoton pair generation can lead to a degradation of the visibility. The experiment is conducted in the dark and the detectors are covered to reduce the dark counts on the detectors.

4.5 Hong-Ou-Mandel interference visibility measurements

We observe a high HOM visibility of 90 ± 0.8% between photons sent through the TE0 and TE2 mode channels. In Fig. 4.4a, coincidences with accidentals subtracted are plotted against relative path length difference between the two input arms, and the best Gaussian fit is indicated by the red curve. The visibility is calculated using the following expression $V_{HOM} = 1 - \frac{C_{min}}{C_{max}}$ where C_{min} is the minimum coincidence rate and C_{max} is the maximum coincidence rate (see

Eq. 3.15). The device with splitting ratio near 1/2 (where $N = 20$), yields the highest visibility of $90 \pm 0.8\%$ with a coherence length of $168 \pm 10\ \mu$m, which we estimate from the width of the coincidence dip. This device is primarily limited by the source visibility, which we measure to be 92% due to spectral mismatch of the two arms. With an ideal source, this device could have a high visibility of 99% with a measured splitting ratio of $\eta_{\text{exp}} = 0.55$. In Fig. 4.4b, we show mea-

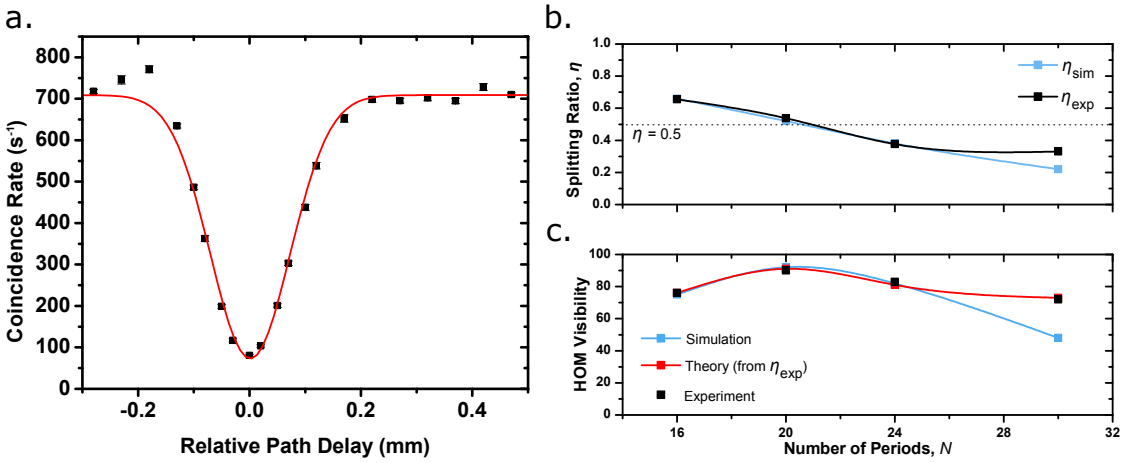

Figure 4.4: **Hong-Ou-Mandel Interference between TE0 and TE2.** a) We show the coincidence rate (accidentals subtracted) of the two output arms as we delay one input arm. The red line is a Gaussian fit to the experimental data. The HOM visibility is $90 \pm 0.8\%$. The error bars indicate the standard error of measurement and are not visible because they are smaller than the data points. b) Comparison between experimental and simulation of the splitting ratio as the number of periods (N) is varied. Error bars on experimental data are smaller than data points. c) Corresponding HOM visibility as the number of periods (N) is varied.

sured splitting ratios near 1/3, 1/2, and 2/3 for devices with different numbers of coupling periods, which agree well with simulations. These ratios have been of particular importance in path-encoded implementations of controlled-NOT gates in quantum photonic circuits[12]. Note that the device with the longest

coupling interaction does not produce as much splitting as predicted by simulations, which is most likely due to residual phase mismatch. As expected, we show that the experimental HOM visibilities depend on the splitting ratios measured and agree well with their theoretical visibilities from the measured splitting ratios (see Fig. 4.4c). To show that this method easily extends to other modes of different parities, we also demonstrate a visibility of 78±0.3% between TE0 and TE1. We use an asymmetric grating for a structure that is limited to 78% by its splitting ratio, $\eta_{exp} = 0.64$ (see Fig. 4.5).

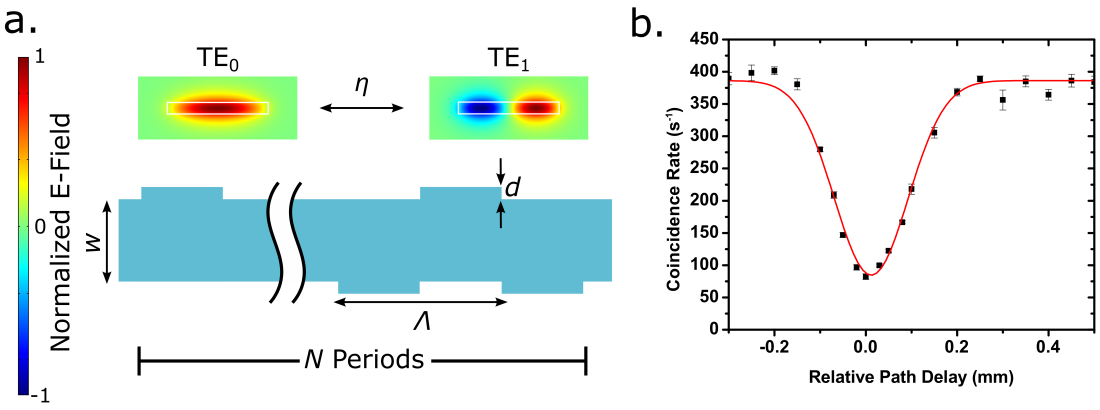

Figure 4.5: **Hong-Ou-Mandel Interference between TE0 and TE1.** a) Schematic of asymmetric grating to couple even to odd modes. The period (Λ) is 8 μm, number of periods (N) is 8, and grating depth, d, is 24 nm. The width, w, is 1010 nm and height is 190 nm. This corresponds to a splitting ratio $\eta = 0.64$. b) We show the coincidence rate (accidentals subtracted) of the two output arms as we delay one input arm. The red line is a Gaussian fit to the experimental data. The HOM visibility is 78 ± 0.3%. The error bars indicate standard error of measurement.

To further confirm the observed Hong-Ou-Mandel effect, we measure photon coalescence enhancement at the individual output arms of the HOM interferometer[70, 71]. We expect a doubling of the probability of case TR (TE0 Transmitted, TE2 Reflected) and RT (TE0 Reflected, TE2 Transmitted) in the

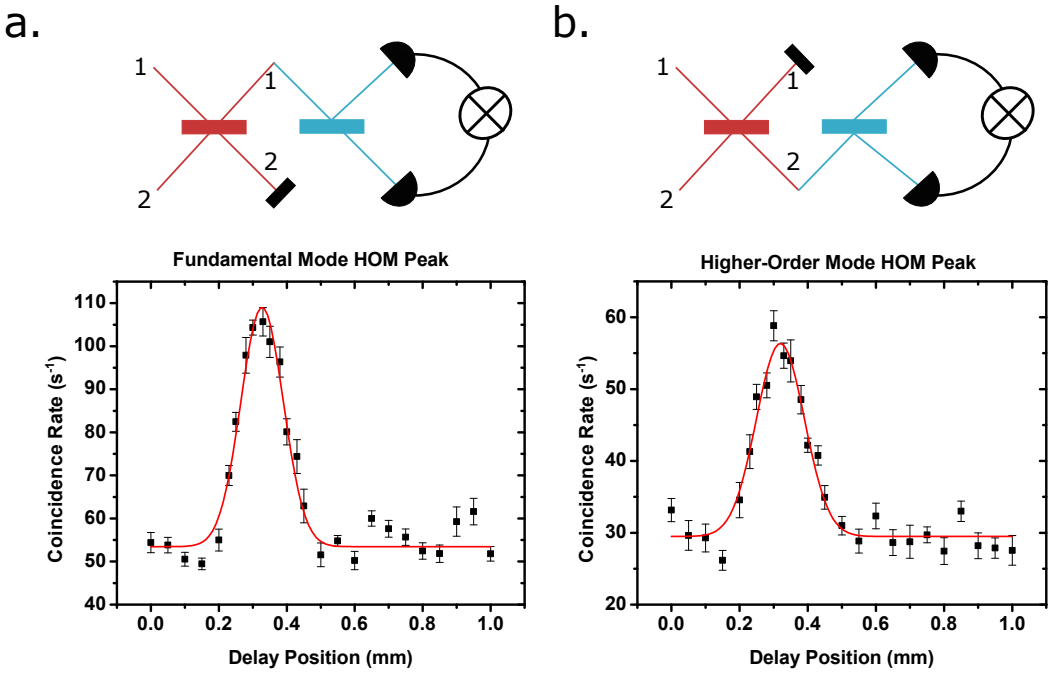

Figure 4.6: **Hong-Ou-Mandel Peak Interference.** Top: Schematic shows HOM peak experiment arrangement. Red indicates on-chip spatial mode beamsplitter, and blue indicates fiber beamsplitter. Pairs of photons are simultaneously coupled into the fundamental mode (input port 1) and higher-order mode (input port 2) of the on-chip spatial mode beamsplitter. To determine the fundamental mode HOM peak, the photons from the fundamental mode (output port 1) are sent to a fiber beamsplitter, and coincidences are measured using detectors and coincidence logic. The same is done for the higher-order HOM peak using output port 2. a) Coincidence rate of the fundamental mode output arm after the fiber beamsplitter. There is a peak in coincidences due to HOM bunching. b) Coincidence rate of the higher-order mode output arm after the fiber beamsplitter.

HOM experiment in comparison to the experiment with distinguishable photons (see Fig. 4.1b). We use a fiber beamsplitter at the individual output arms of the spatial mode beamsplitter ($\eta = 0.55$) and measure coincidences. Figure 4.6 show a peak in coincidences for both the fundamental and higher-order mode output port with a visibility of 2 ± 0.02 that matches well with theory. The visibility is calculated using the following expression $V_{HOMpeak} = \frac{C_{max}}{C_{min}}$ where C_{min} is the minimum coincidence rate and C_{max} is the maximum coincidence rate (see Eq. 3.19). The width of the multi-mode HOM peak is $166 \pm 10\,\mu$m, and the width of the single-mode output is $147 \pm 10\,\mu$m. This effect has been used as a basis for quantum cloning experiments[70].

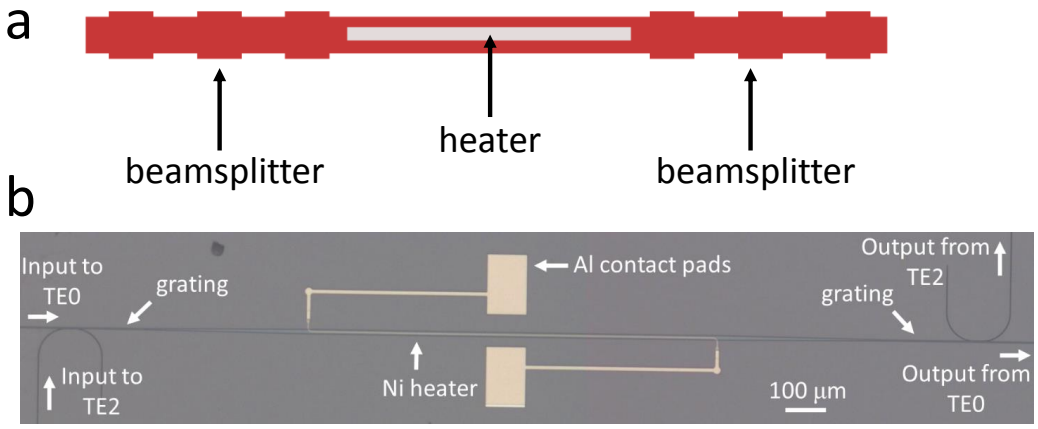

Figure 4.7: **NOON State Device Configuration.** a) MZI is formed using two beamsplitters and a phase shifter. b)This microscope image of the NOON state device shows how the Mach-Zehnder interferometer is formed. First, the two inputs are sent to the mode multiplexer which sends one input to the fundamental mode (TE0) and the second input to the higher-order mode (TE2). Next, the two modes are mixed at the spatial mode beamsplitter (or nanoscale grating). The two modes are then sent to the phase shifter (Ni heater). Finally, the two modes are mixed at a second spatial mode beamsplitter and sent to single-mode outputs through the mode demultiplexer. Scale bar is 100 μm.

4.6 NOON interference visibility measurements

Finally, to show these structures can be cascaded and actively tuned, we fabricate a Mach-Zehnder structure to create a NOON state interferometer based on our spatial mode beamsplitter[59]. The HOM interferometer and phase shifter produces the NOON state described by: $\frac{1}{\sqrt{2}}(|2\rangle_1|0\rangle_2 + e^{2i\phi}|0\rangle_1|2\rangle_2)$ where ϕ is the phase between the two modes of the interferometer and the subscripts 1 and 2 refer to the different modes. NOON states are more generally written as $\frac{1}{\sqrt{2}}(|n\rangle_1|0\rangle_2 + e^{in\phi}|0\rangle_1|n\rangle_2)$ and provide increased phase sensitivity, ϕ, by $\frac{1}{n}$ for quantum metrology over the standard quantum limit of $\frac{1}{\sqrt{n}}$[59]. In our experiment, the Mach-Zehnder structure consists of two gratings separated by a phase shifter, a length of waveguide and heater. Within the phase shifter, the waveguide is tapered out to 10 μm width which gives a larger differential in phase shift between the fundamental and higher order modes as the heater is tuned (see Fig. 4.7).

In Fig. 4.8, we show measurements of the classical interference by inputting a single arm of the SPDC source into the device and measuring the single counts of both output arms, which show the classical Mach-Zehnder fringe as expected. This specific device ($\eta_{\text{exp}} = 0.66$) has a classical visibility of $82 \pm 8\%$ with a period of about 1.3 ± 0.082 W, which corresponds to the power of the heater. The relatively high powers required to achieve a differential phase shift between the higher-order modes requires further optimization. Simulations and extended discussion on this point are included in the discussion section. We then measure the two-photon interference, or NOON state interference, by measuring coincidences when both arms of the SPDC source are input into the device with no path delay. We observe a visibility of $86 \pm 1\%$ with a period of 0.64 ± 0.005 W,

about half of the classical interference (see Eq. 3.30). The visibility is calculated using the following expression $V_{NOON} = \frac{C_{max}-C_{min}}{C_{max}+C_{min}}$ where C_{min} is the minimum coincidence rate and C_{max} is the maximum coincidence rate. In addition to the increased phase sensitivity, this demonstrates the active tunability of this device, which could be useful in state preparation for quantum simulators [51, 13, 15].

4.7 Discussion

4.7.1 Visibility Degradation due to Loss and Cross-talk

The primary sources of visibility degradation, aside from the non-ideal spontaneous parametric downconversion source, are the asymmetric loss of the spatial mode beamsplitter and the cross-talk of the mode multiplexer.

The cross-talk originates from the residual coupling away from the optimal phase matching point. In our case, we measure a cross-talk of less than -29 dB from the mode multiplexing. This leads to a non-ideal splitting ratio which degrades the visibility by approximately 0.002%. We also show that these devices can be cascaded and maintain high visibility through tapering structures consisting of a larger number of modes. For the quantum NOON state, we measure a visibility of 86 ± 1%. The splitting ratio (η) for this device is 0.66 which results in an ideal visibility of $2\sqrt{\eta(1-\eta)}$ which is about 94.7%. If we take into account our source visibility of 92%, the estimated visibility is 87% which is within the error of our measurement. There is no significant degradation of the quantum visibility due to additional spatial modes in the NOON state interferometer, and this degradation comes solely from the deviation of the splitting ratio from 0.5.

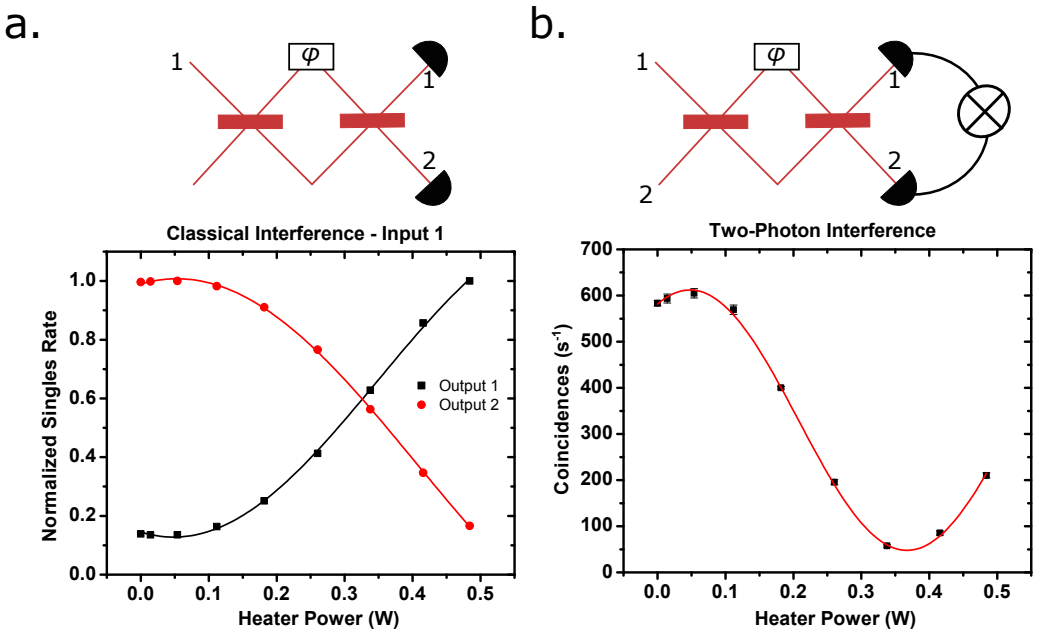

Figure 4.8: **NOON Interference.** Schematic shows NOON interference experiment arrangement. Red indicates the on-chip spatial mode beamsplitter. Pairs of photons are simultaneously coupled into the fundamental mode (input port 1) and higher-order mode (input port 2) of the on-chip spatial mode beamsplitter. The two photons are sent to the spatial mode phase shifter based on an integrated microheater which applies a phase shift (ϕ) between the fundamental and higher-order modes. Finally, coincidences are measured using detectors and coincidence logic. a) Classical Mach-Zehnder interference is shown as a function of heater power which applies the phase shift. b) NOON interference is shown as a function of heater power. The period of the quantum interference is half that of the classical interference. The error bars indicate standard error of measurement for all plots.

The loss that contributes to the degradation of the visibility comes from an asymmetry in the loss between the supermodes (or coupled modes) within the beamsplitter. Here, we follow the derivation from Atwater for a lossy beamsplitter[88]. The theoretical maximum visibility is:

$$V = 1 - 2\cos^2 \Delta\theta \tag{4.1}$$

where $\Delta\theta$ comes from the phase difference between the reflected and transmitted modes. As derived in Atwater, the phase difference is:

$$\Delta\theta = 2\tan^{-1}(e^{\frac{\pi\Delta n_{\mathrm{i}}}{2\Delta n_{\mathrm{r}}}}) \tag{4.2}$$

where Δn_{i} is the difference of the imaginary effective index of the supermodes, and Δn_{r} is the difference of the real effective index of the supermodes. We estimate $\Delta n_{\mathrm{r}} = 1.6 \times 10^{-3}$ which we calculate from our coupling coefficient. As a worst case scenario, we attribute all of the 0.2 dB loss to the difference in the imaginary effective index to get $\Delta n_{\mathrm{i}} = 2.19 \times 10^{-5}$. We estimate this degrades the visibility by less than 0.1%. This is an overestimate of the difference in loss between the supermodes because the supermodes should have similar interactions with the sidewalls of the waveguide. The sidewall roughness from etching is the primary source of scattering loss. This can be further improved by using a waveguide width that is larger which minimizes the sidewall interaction further.

4.7.2 Improving the Noon State Structure

The power required for this phase shift could be reduced by bringing the heater closer to the waveguide. In Fig. 4.9, we show COMSOL numerical simulations

that calculate the temperature distribution and uses the thermo-optic coefficient to recalculate the effective index of the optical mode, which we use to calculate the relative phase shift of different modes. For example, according to Fig. 4.10a if the distance is changed to 1.2 μm away, which still does not affect the optical mode, the heater power for a π phase shift is reduced by more than half.

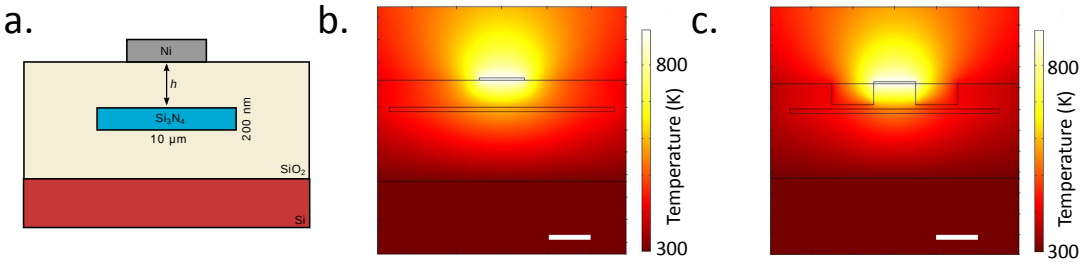

Figure 4.9: **Thermo-Optic Phase Shifter Cross-Section.** a) Schematic shows the cross-section of the thermo-optic phase shifter which consists of a heater placed above the waveguide with a heater distance of h. The thermo-optic effect changes the refractive index of materials as a function of temperature, which leads to an accumulation of additional phase. In this experiment, the phase shifter consists of a waveguide region that is increased to 10 μm with a heater above the waveguide with SiO_2 cladding, where h is 2.3 μm. The heater is made of Ni, and the contact pads are made of Al. b) FEM simulation of heat distribution from the heater where h is 1.2 μm. Simulation is shown for a heater distance of 1.2 μm which doubles the heater efficiency. Scale bar is 2 μm. c) FEM heat distribution from the heater with a heater distance of 1.2 μm and air trenches to provide stronger gradient in temperature across the waveguide. The air trenches are indicated here by the rectangles adjacent to the heater. This strong thermal gradient across the waveguide leads to a greater relative phase shift between the fundamental and higher-order modes of the waveguide. Scale bar is 2 μm.

If we compare the relative phase shift between the TE0 and TE2 modes in a multi-mode waveguide and the relative phase shift between two single-mode waveguides used in path-encoding using the same path length and heater dis-

tance, the power required for a π phase shift in the multi-mode waveguide is about 7 times larger (see Fig. 4.10b). This occurs because the modes are spatially co-located, and the thermo-optic refractive index change affects both modes to some degree. However, one should note that this is the first proof-of-principle demonstration using a simple design technique. The efficiency of the differential phase shift induced by the heaters can be improved using the techniques we discuss here. In this work, we address this issue by using a localized micro-heater. As shown in Fig. 4.10c, we used a heater width of 2 μm which shows the most efficient phase shifter. The heater power is reduced by 80% by using a heater that is 2 μm rather than 10 μm because the heat is localized and heats the TE0 mode more than TE2.

To reduce this power even further, trenches can be used to provide a stronger thermal gradient across the waveguide and apply a greater phase shift between the different modes. In Fig. 4.10d, we show that the trenches reduce the power by 25% for an overall power reduction of about 90% from the results of this experiment.

Our analysis here has been limited to thermo-optic phase tuning. However, other electro-optic effects could be more localized. Further research in this area should include intermediate structures that utilize the inherently different coupling coefficients to apply larger differential phase shifts between the spatial modes.

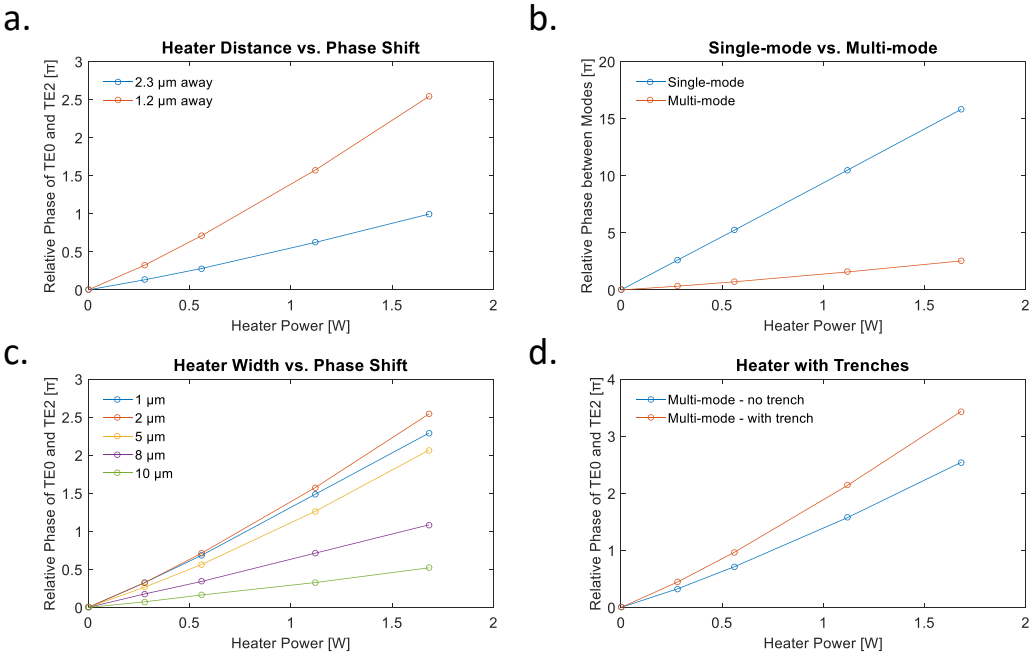

Figure 4.10: **Numerical Simulations of Thermo-Optic Phase Shifting.** a) Shows the calculated relative phase shift between TE0 and TE2 for two different heater distances as a function of heater power. The heater power for a π phase shift is reduced by more than half by decreasing the heater distance from 2.3 μm to 1.2 μm. b) Shows the calculated relative phase difference between two single-mode paths and two spatial modes within a multi-mode waveguide as a function of heater power. The heater power required for a π phase shift is about 7 times larger for the multi-mode phase shifter than a single-mode phase shifter because the heat within the multi-mode waveguide interacts with all the spatial modes to some extent. c) Shows the relative phase shift between TE0 and TE2 for different heater widths as a function of heater power. In this experiment, we address the phase shifter efficiency issue by using a localized heater with a width of 2 μm. The plot shows this is the optimal heater width for a 10 μm wide waveguide. The heater power required for a π phase shift is reduced by 80% when the width is decreased from 10 μm to μm. d) Shows the relative phase shift between TE0 and TE2 for a structure with and without trenches as a function of heater power. Air trenches surrounding the heater provide a strong thermal gradient across the waveguide which increases the relative phase between the spatial modes. The power required for a π phase shift is reduced by 25% by adding the air trenches.

4.7.3 Scalability of Platform

In this work, we show a step perturbation that has a frequency response that includes additional higher order frequencies. Because we have limited our multi-mode waveguides to the three lowest-ordered modes, these higher frequency components do not pose problems. When dealing with a larger number of modes that require couplings given by multiple spatial frequency components, a sinusoidal perturbation would ensure less cross talk between the modes. These devices for two-mode couplings could be cascaded to create arbitrary transformations between modes. This initial demonstration between two modes can be extended to make arbitrary n-dimensional unitary matrix transformations on a set of modes, which is essential for quantum information processing and simulation[89].

Arbitrary NxN mode transformations can be made using cascaded 2x2 beamsplitters and phase shifters[56]. In the mode multiplexing platform proposed, gratings can be used as 2x2 beamsplitters and short lengths of waveguide can be used as passive phase shifters. The gratings can be designed using selective phase matching. No extra components are necessary because the waveguide modes are co-propagating and do not need additional routing.

Here, we show a design and numerical simulation for a three mode splitter based on 2x2 splitters using a single multi-mode waveguide with the same dimensions as the device in the main text (height = 200 nm, width = 1.6 μm) that contains three modes (TE0, TE1, and TE2). The design consists of three grating sections that couple two modes with different ratios depending on the grating depth, d, and period, Λ (see Fig. 4.11a). Here we use two asymmetric gratings to couple even to odd modes (TE0-TE1 and TE1-TE2) and a symmetric grating

to couple two even modes (TE0-TE2); the final transfer matrix is theoretically as follows where $b = e^{(\pm j2\pi/3)}$:

$$U = \frac{1}{\sqrt{3}} \begin{bmatrix} 1 & 1 & 1 \\ 1 & b & b^* \\ 1 & b^* & b \end{bmatrix} \tag{4.3}$$

The network of 2x2 beamsplitters offers the most flexibility and control of the NxN transformation. Using this approach, we can compare the estimated footprint of the path-encoded platform and the mode-encoded platform for a larger number of modes. Assuming silicon nitride waveguides with oxide cladding, the footprint of a path-encoded beamsplitter based on a 2x2 multi-mode interferometer (MMI) structure with S-bends is approximately 1000 μm^2. We estimate the area of the mode-encoded beamsplitter using FEM simulations for the width scaling and an estimate of the coupling coefficient. For five modes, the path-encoded structure is about 15 times larger than the mode-encoded structure for the same number of operations. We estimate the ratio of the footprint of a path-encoded system to a mode-encoded system with increasing number of modes (see Fig. 4.12). This ratio saturates because we have only included horizontal higher-order modes which increases the width of the waveguide.

However, a compact MMI splitter for 4x4 can be made[90]. In this case, the footprint is about 4 times larger than the mode-encoded version in our work (using 2x2 transformations), and this ratio slowly increases with the number of modes. This occurs because as the width of the MMI is increased to incorporate more modes, the length to form the constructive images increases as well. To our knowledge for $N > 4$, it becomes difficult to experimentally realize an MMI with

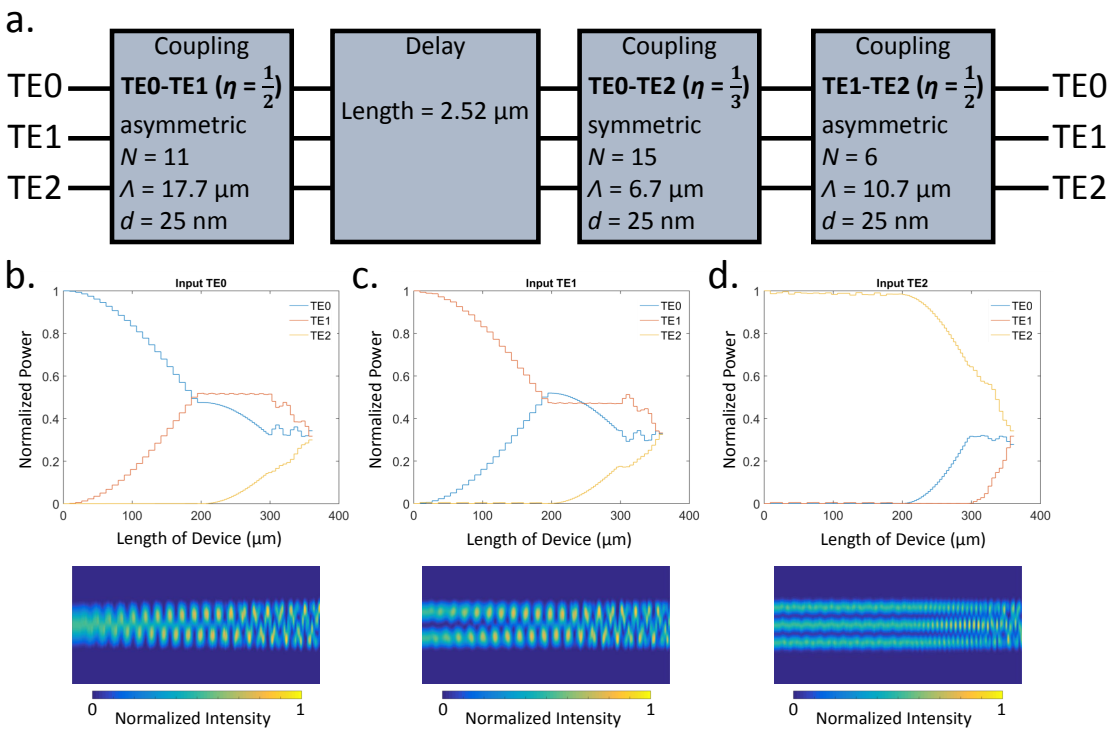

Figure 4.11: **Three Mode Splitter Example.** a) Design of a three mode splitter using cascaded two mode couplings. The parameters are given for asymmetric or symmetric gratings as defined in the main text (see Fig. 2 and Fig. 4 from main text). b) Numerical simulation of the normalized mode powers when TE0 is input into device from part a. Below is the total normalized intensity distribution along the structure. c)Numerical simulation of the normalized mode powers when TE1 is input into device from part a. Below is the total normalized intensity distribution along the structure. d)Numerical simulation of the normalized mode powers when TE2 is input into device from part a. Below is the total normalized intensity distribution along the structure.

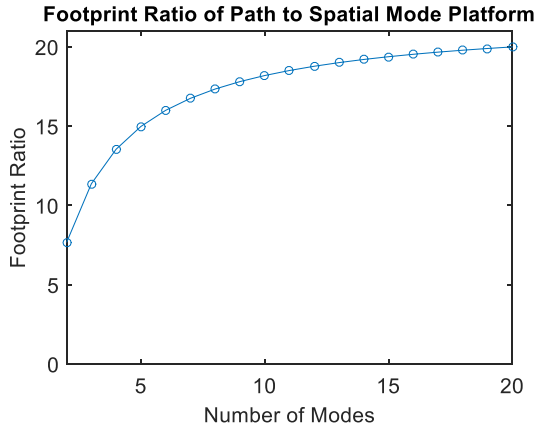

Figure 4.12: **Footprint comparison of path to spatial mode encoding using 2x2 transformations.** We compare the ratio of system footprints for the same number of 2x2 operations as a function of the number of modes. We assume silicon nitride waveguides with 200 nm height and a path-encoded beamsplitter with 55 μm $\times$ 18 μm.

a balanced output and low insertion loss due to phase errors in the multi-mode section and the approximation necessary for the re-imaging principle. Ideally, these MMI structures are simple structures, but they are primarily limited to symmetric splitting transformations. It has been suggested in literature to use gratings similar to those proposed in our work within the multi-mode section of the MMI to control the modes and produce variable splitting ratios[91]. Hence, the techniques we suggest here can be leveraged to improve path-encoded MMI designs as well.

There are many routes to scaling our mode-multiplexing platform even further by simply changing the geometry of these structures. Currently, in the mode-multiplexing community, the number of modes is increased by slightly increasing the width of the waveguide. However, by increasing the height of the waveguide, we can increase the number of modes while keeping the footprint

constant. For example, if the 200 nm height of the silicon nitride waveguide in this paper is increased to 600 nm, twice as many modes are included, which can approximately halve the footprint.

The true potential of this platform can be realized by taking advantage of the fact that since these modes are co-propagating within the same waveguide, any mode can be accessed at any point without extra bends or waveguide crossings that induce loss. Multiplexed gratings can be used to simultaneously perform multiple couplings between different modes within the multimode waveguides. This can dramatically reduce the mode-encoded footprint to that of a single stage. These footprints can be as small as 40 μm^2, making them about 100 times smaller for the same number of modes of a path-encoded system[24, 25, 80]. The challenge will be to make compact devices such as these that are still highly tunable.

4.8 Conclusion

Assuming 5 nm fabrication tolerance on dimensions, we can realistically expect to multiplex at least 15 modes within a silicon nitride waveguide[92]. This number of quantum modes corresponds to a Hilbert space with a dimensionality of $15^2 = 225$ for a two-waveguide system. Higher-index materials will increase the number of modes that can be multiplexed. These designs could also be made more compact by using multiplexed gratings in which the perturbation has multiple spatial frequency components and strengths to design arbitrary transformations of the modes[24, 82, 25, 80]. This same analysis can be extended to the quasi-transverse magnetic TM polarized spatial modes, and adi-

abatic tapers and asymmetric gratings can be used to convert between TE and TM polarized modes[29, 76]. Combining spatial mode encoding with polarization and path encoding can further increase the Hilbert space of the integrated waveguide platform.

We show that these structures are tunable and can be cascaded while preserving high visibility quantum interference, which will be key to building larger networks. Multi-mode waveguides can be used with other degrees of freedom to encode information within a high-dimensional Hilbert space using only linear passive devices within a small footprint. These miniaturized systems with high information density could eventually be interfaced with spatial mode multiplexing in fiber and free-space systems for quantum information processing and could be specifically useful in quantum repeaters, memories, and simulators.

CHAPTER 5

NEURAL INTERFACE FOR OPTOGENETICS

5.1 Introduction

The brain is the most complex organ in our body, controlling our behavior, learning, thoughts, movements, and senses. The field of neuroscience aims to understand brain function, taking approaches that range from studying the biochemistry of synapses to large-scale fMRI studies of blood flow to different regions of the brain and finally to studying behavior. Understanding the underlying biology of the brain, as well as the ways this biology can be perturbed, is essential for understanding neurological disorders and developing new treatment strategies.

In recent years, new technologies have advanced both understanding and treatment of such diseases. For example, there has been significant interest in the application of treatments like deep brain stimulation, in which electrodes send high frequency electrical impulses to regions of the brain to modify neural activity, to neurodegenerative diseases like Alzheimer's, Parkinson's, and Huntington's disease, which are characterized by the loss of neuron function and subsequent loss of memory, the ability to think, or movement control. Indeed, deep brain stimulation was FDA-approved in 2007 as an effective treatment for Parkinson's disease with less side effects than medication. Strategies like deep brain stimulation may be similarly effective in treating other diverse neurological conditions, such as depression and obsessive-compulsive disorder.

In addition to addressing neurological diseases, the field of brain-machine

interfaces have made significant progress in creating neuroprosthesis for individuals who have been paralyzed or physically disabled. A brain machine interface uses inputs and outputs of neural activity within the brain connected to hardware and software external to the brain to provide prosthetic limb function that has been lost by purely analyzing neural activity [93]. The goal is to find discriminatory features in the neural signals to represent users' intentions, such as a movement of the arm.

The brain consists of a complex network of neurons that has been relatively unexplored on a systems level. To make the matter even more complicated, the network is constantly evolving as one learns and experiences, which is termed neural plasticity. There have been many fundamental studies that have been done using single neuron patch clamp methods to learn about the basic unit cell of the brain, the neuron [94]. However, to study the brain as a system, we need tools that can match the scale and hierarchy of the brain [95]. To study the brain circuit on a systems level, the signal timing and spatial connections between individual neurons and ensembles of neurons must be understood. Developing these types of tools ranging from large scale extracellular neural recordings to applying wide-field microscopy techniques for visualizing neural activity has been an active area of research for many years. All of these techniques are working toward a mutual goal of developing a neural interface in which we can deliver inputs and outputs to study the brain to allow us to correlate brain function with behavior.

These neural interfaces should work at a spatiotemporal timescale that matches that of the brain. The human brain consists of approximately 100 billion, or 10^{11}, neurons connected by even more synapses[96, 97]. The neuron

size and density changes across different animals and hierarchy. For example, for a mouse, a commonly used animal model in neuroscience, each neuron is approximately 15-20 microns and spaced about 30 microns apart. Their visual cortex has layers defined by different cell types and density of connections. The fundamental neuron signal, the action potential, which is a change in electrical membrane potential of a neuron typically has frequency components between 0.6-6 kHz. The firing frequency of a single neuron is often between 25-50 Hz. However, there are other higher frequency timescale such as gamma oscillations which occur between 50-200 Hz[98, 99].

5.2 Optogenetics as a Tool for Neuroscience

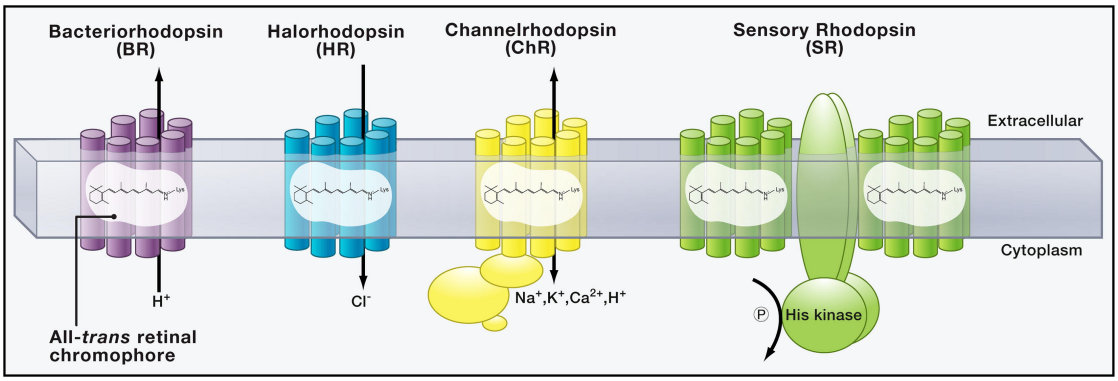

Figure 5.1: **Light-activated ion channels for optogenetics**. Reprinted with permission from [100] Copyright 2011 Elsevier Inc.

Optogenetics provides the ability of light to control neural activity and behavior to understand brain function on a millisecond timescale. Specifically, light can be used to control the precise activation and inhibition of genetically modified neurons. This has allowed for direct, fast and cell-specific targeting of neural populations that was not possible with electrical stimulation

methods[16, 101]. Several recent studies have shown the potential of optogenetics for basic research as well as therapeutic applications. For example, optogenetic control of neurons was used in the ventral tegmental area to differentiate specific reward-related functions of dopaminergic and GABAergic neurons[102]. For therapeutics, optogenetic stimulation of the mouse medial frontal cortex was shown to reduce depressive-like behaviors[103]. Finally, it was shown that optogenetically-controllable motor neurons can be generated in vitro from stem cell precursors and implanted into mice, where they can control muscle function[104].

Light-activated ion channels are introduced to the neurons through genetic modification[100]. The most commonly used channel is Channelrhodopsin-2 (ChR2) which is a light-activated cation channel of the most commonly used for activation of a neuron. Halorhodopsin a light-activated chloride pump that is activated by yellow light that is typically used for inhibition of a neuron. There are many more variants which have been extensively used and studied (see Fig. 5.1). Their excitation spectrums lie within the visible wavelength range from 400-600 nm. The most common, ChR2, peaks in the blue wavelength range around 473 nm (see Fig. 5.2).

5.3 Light Scattering and Absorption in the Brain

The two main challenges in delivering light to different regions of the brain is a combination of absorption and scattering by different components within the tissue. Both mechanisms attenuate light and limit the depth at which one can image and deliver light. The absorption is primarily dominated by water which

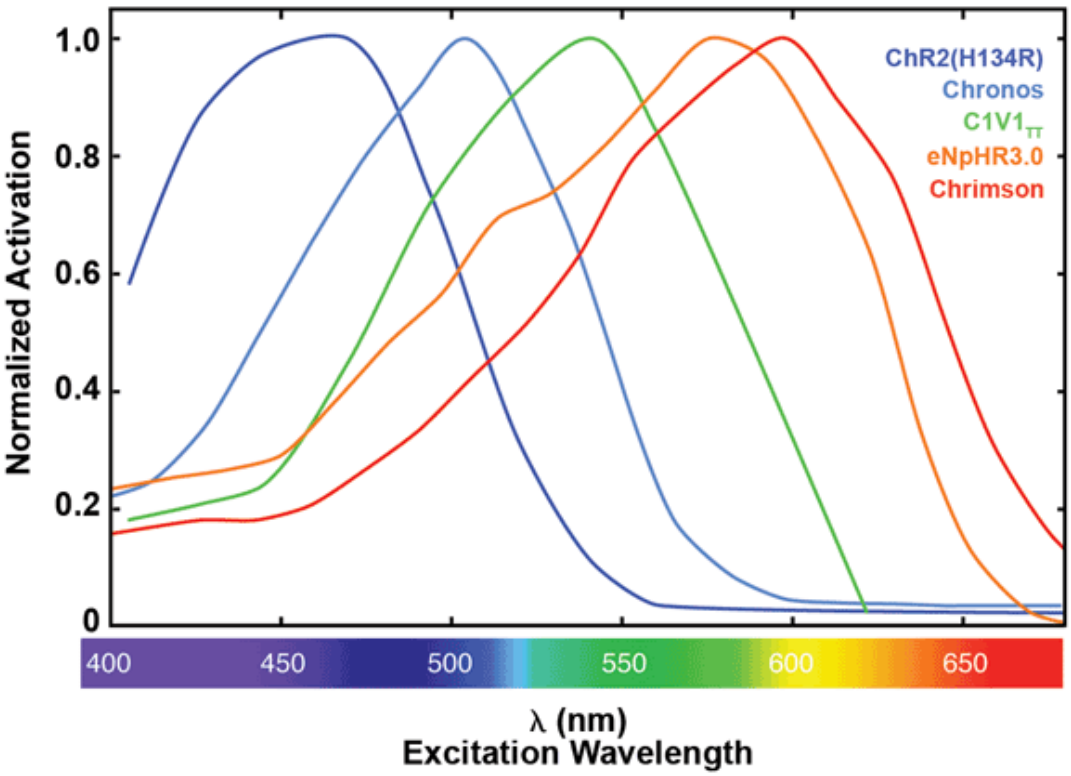

Figure 5.2: **Excitation spectrum for common opsins [105].**

is lowest at 418 nm and increases for both longer and shorter wavelengths (see Fig. 5.3). This in addition to the availability of fluorophore and opsins is why the visible wavelength range from 400 nm - 600 nm is ideal for imaging and optogenetic excitation.

However, the primary source of attenuation within the brain is due to Mie scattering from cell bodies and fibers and this dominates at these shorter wavelengths[106]. This limits free-space microscopy methods to studies using the surface of the brain, cultured cells, brain slices, or small transparent organisms such as *C. elegans*[107, 108]. If both the absorption and scattering are taken into account, one can see that at 473 nm, where the ChR2 response peaks, the penetration depth is about 100 μm.

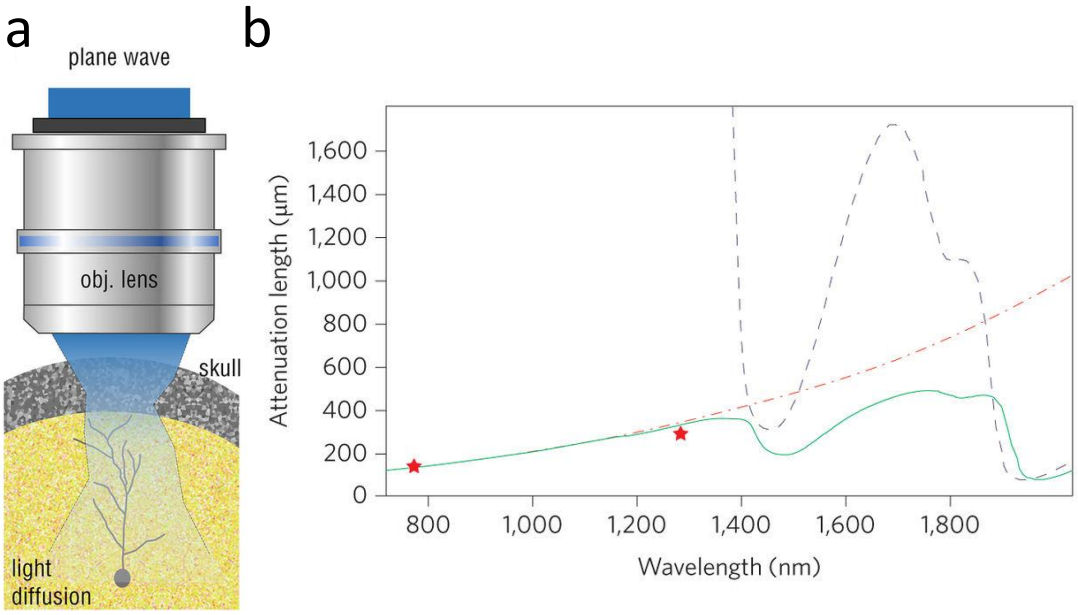

Figure 5.3: **Light Scattering in the Brain.** a) Shows degradation of a focal spot from an objective due to light scattering (reprinted from [109] which is work licensed under CC BY 4.0). b) Light attenuation as a function of wavelength due to absorption (blue dotted line) and scattering (red dotted line) and combination (solid green line). Reprinted with permission from [107] Copyright 2013 Macmillan Publishers Limited, part of Springer Nature.

5.4 Typical Optogenetics Experiment

To overcome this issue, the typical optogenetics experiment uses a single fiber for light delivery for input neural stimulation and metallic wires for output neural recordings to combine deep-brain excitation with electrophysiology methods, which will be discussed later in the chapter[110]. Typically, 200 μm multimode fiber is used which provides a cone of light depending on its numerical aperture (NA), typically ~0.6 NA which has a divergence around 52°. This is used to flood a specific region of the brain. Only the neurons that have been

genetically modified can be stimulated by light. This can be designed to target specific cell types. However, considering the density of neurons within the brain, this technique targets many neurons simultaneously. This synchronous activity across a large population is not physiological. Again, the holy grail to studying the interconnections of the brain, there is a great need for complex light stimulation that has high temporal resolution with single cell excitation capabilities.

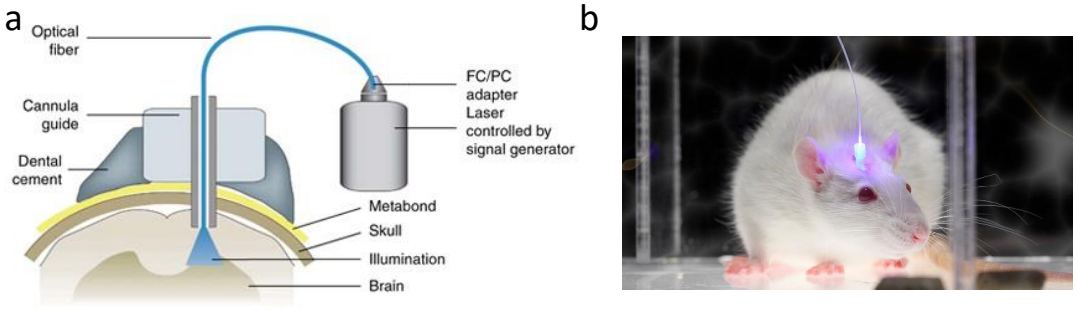

Figure 5.4: **Typical Optogenetics Experiment with Fiber** a) Light delivery using fiber into the brain (reprinted with permission from [111] Copyright 2010 Macmillan Publishers Limited, part of Springer Nature). b) Fiber attachment for a freely moving mouse during an optogenetics behavior experiment[112].

5.5 Light-delivery Methods for Patterned Optical Excitation

There have been many techniques making progress towards addressing this issue to create a high spatiotemporal resolution light source that can generate complex illumination patterns deeper within the brain.

Free-space Microscope

Optical techniques using free-space microscopes such as multiphoton excitation can extend penetration depths up to 0.7 mm for two-photon and 1.3 mm for three-photon excitation into the surface of the brain[107]. For example, for two-photon excitation, a widely used optical imaging technique, a high power pulse of longer wavelength light (700 - 1000 nm) is needed for two-photon absorption to occur within the opsin or fluorophore near 350 nm - 500 nm. Typically, a red-shifted opsin such as C1V1 near 550 nm is used because the calcium indicators for imaging and recording neural activity also have absorption spectrums around 460 nm. High energy pulses are necessary because multiphoton absorption is based on a nonlinear optical process which is more efficient at higher intensities. The probability of excitation goes as the optical power squared. This allows for a more localized and deeper excitation centered around the focal spot because out of focus light excitation is eliminated. However, even with three-photon imaging, the technique is limited to 1.3 mm. A major issue for using two-photon techniques for optogenetic excitation is the fact that the highly focused spot is smaller than the neuron cell body and cannot activate an action potential. Therefore, a scanning technique must be used which limits the speed of stimulation to 11 ms per action potential [113, 114].

To increase the lateral resolution of the focal spot using multiphoton excitation without sacrificing the axial resolution which eliminates the need for scanning, a powerful technique called temporal focusing is used to decrease the time necessary for activation to millisecond level[115, 116]. Typically, it is still difficult to have a large field of view while maintaining the high temporal resolution.

Spatial light modulators (SLM) have demonstrated the most promise in

terms of reconfigurability for creating patterned light or tunable focusing capabilities. However, they are typically composed of liquid crystals which limit their frame rates to 60 Hz. Recently, SLM's based on liquid-crystal-on-silicon have faster frame rates of up to 300 Hz and have been used for imaging but have not yet been used for excitation[117]. Acousto-optic 3D deflector systems which could potentially operate in the 10 kHz range have also been used for imaging[118, 119]. Other free-space optics components such as galvanometers are limited to speeds of 10 Hz and piezoelectric resonant systems are limited to speeds of 100 Hz or lower due to the inertia of large objectives and mirrors.

Although these techniques provide control over large volumes of neurons, at this point they are not implantable and therefore do not allow experiments deep within the brain or in freely behaving animals.

Fiber

Another approach is to use a fiber that can selectively activate different depths of the brain. A tapered and nanostructured fiber probe has been used to excite the dorsal versus ventral striatum of a freely moving mouse by selectively exciting different spatial modes within the fiber[120, 121]. Different modes are excited by scanning a mirror using a galvanometer to input the light at different angles. Depending on the angle of light and the mode that is excited the light exits at different depths. The number of emitters is limited to the number of modes in the fiber and if there is sufficient power when excited at an angle (~10 modes). Also, the resolution is limited by how selectively a mode can be excited. Typically, in fibers this is difficult to achieve since the fiber core has low index contrast. In this case the resolution was limited to about 100-500 μm. The

speed is limited by the method of excitation of these modes, which is a around 10 Hz for a galvanometer and becomes difficult to multiplex many points.

Micro-LEDs

To further increase the scalability and resolution of these emitters, micro-LEDs embedded on implantable probes have been used as a multichannel light source that can deliver patterned optical stimulation with resolution down to 50 um in a freely moving mouse [122, 123, 124, 125]. They have a large beam divergence[126]. Although these micro-LEDs can be made micron-scale, their optical output is highly diverging (~70°) making it difficult to excite with single cell resolution. Their electrical nature creates two problems for scalability: (1) their necessary proximity to the exposed neural recording sites creates an electrical artifact that interferes with recordings and (2) they generate heat within the brain at higher optical powers and switching speeds that can disrupt natural neural processes. At frequencies of 30 Hz, the temperature change is 0.5° [124]. This increases above biologically safe values at higher frequencies. These micro-LEDs have been made on flexible substrates and wireless which enable unique experiments on freely moving mice [127].

Waveguides

Another method for light delivery is using waveguides that have been lithographically defined to provide a way to deliver light with high resolution without introducing a heat source inside of the brain. This allows the light to be delivered to specific locations without heat-generating electronics directly near

the neural recording sites. In the past, the waveguides have been large and made of materials like Su8 and SiON, which are difficult to scale and create active photonic devices that are reconfigurable due to the lack of control of the higher order modes [128, 129, 130, 131]. Recently there have been demonstrations of high confinement waveguides made in SiN which have the potential to be scaled. These have been passive waveguides. All of these techniques require external reconfigurable light sources. This could be done by coupling lasers or LED's to individual waveguides, or using the same methods for scanning beams used for free-space microscopy methods. Recently, a photonic probe has been developed to generate patterns using a wavelength selective arrayed waveguide grating (AWG) structure, which allows light of different wavelengths to be sent to different grating outputs [132]. This probe relies on the active switching of wavelengths using an external tunable wavelength filter. If a high-speed acousto-optic tunable filter had been used as suggested, the power requirements of the filter limits the device to about 10 outputs. We will introduce integrated reconfiguration capabilities to this platform in this dissertation in the following chapter.

5.5.1 Tools for Recording of Neural Response

Optogenetics has been used to study the brain at many space and time scales as discussed before. In addition to high spatiotemporal light delivery, we need to be able to record the neural response with this same resolution. Since the focus of this dissertation is a novel platform for optical excitation, we will only briefly cover neural recording tools. However, they have been extensively reviewed elsewhere.

The action potential, or the single neuron response, is a rapid change in voltage across the neuron cell membrane. The membrane potential is maintained by a balance of ions inside and outside of the cell and the change is mediated by the nonlinear response of voltage gated ion channels [133]. This membrane potential can change from -70 mV (resting) to 40 mV within a millisecond. These action potentials are triggered by inputs from other neurons that bring the membrane potential up above a certain threshold.

Electrophysiology Methods

Primarily electrophysiology methods have been used to study neural activity because it provides a direct measurement of the electrical signals produced by a neuron when an action potential is fired[134, 135, 94, 136]. Electrical methods have provided the highest signal to noise ratio and temporal resolution to resolve individual neural spikes. To study the brain circuit on a systems level, the signal timing and spatial connections between individual neurons must be understood.

Extracellular neural recordings in which an electric potential change is measured outside of the neuron has been the most extensively used recording method in systems level neuroscience because it allows one to study individual neurons for weeks during behavioral studies. This allows one to correlate repeated behaviors with recorded neural patterns to begin to understand the underlying circuit. Since, the extracellular recording is not a direct measurement of the membrane potential, but rather the potential outside, this means the potential changes detected are an order of magnitude smaller, approximately 100 μV. Typically, a microelectrode, or metallic wire, is placed near the neurons to

detect this signal relative to a ground signal that is farther away (i.e. on top of the brain).

The impedance of this microelectrode, around 1 MΩ, determines the noise and distance at which a neuron signal can be picked up[136]. Because the signal is so small, it is important to have low noise recordings. Typically, a low impedance microelectrode, with a larger exposed tip, has lower noise. However, this allows recordings from a larger area, or more neurons. In this case, one has to use a method called spike sorting to distinguish responses from individual neurons. Spike sorting is a method in which different components of the spike waveform are used to identify individual neurons.

The primary issue with electrophysiology methods for neural recording is that it is difficult to differentiate different cell types and exact locations from which the signals have been received. However, extracellular single unit recordings from large-scale arrays of fabricated electrodes have been the dominant tool for systems level neuroscience[135].

Optical Imaging Methods

All-optical methods in which two-photon techniques have been used for optogenetic stimulation and neural recordings based on Ca indicator and Voltage dye imaging [137, 138, 139, 140, 141, 142]. Typically, Ca imaging uses a fluorescent indicator such as GCaMP6 or GCaMP3 to image intracellular calcium ions that flow during an action potential during neural activity, they are typically excited around 460 nm[114]. The major limitation of Ca indicator imaging is that the neural activity is detected indirectly by the flow of

ions whose kinetics are slower, 50-1000 ms, than the actual action potential spikes which occur at a millisecond timescale. This makes it difficult to use calcium imaging to accurately resolve individual spike waveforms and represent spike timing in a network[141]. However, a new class of voltage indicators are being explored which promise timescales comparable to electrophysiological measurements[141].

In addition to the physiological limitation of the speed, there have been many efforts to increase the speed and field of view of the imaging apparatus. An excellent example of this was recording neural activity from two planes simultaneously using a spatial light modulator (SLM) and galvanometers[117]. The field of view is quite large (300 μm by 300 μm), and can capture images over an axial range of 500 μm. This can be used to switch between different holograms at up to 300 Hz. 3D acousto-optic imaging systems have been developed with sub-millisecond resolution as we previously discussed[118, 119].

CHAPTER 6

RECONFIGURABLE VISIBLE NANOPHOTONICS PLATFORM FOR *IN VIVO* HIGH RESOLUTION OPTOGENETICS

6.1 Introduction

The ability to deliver and shape visible light within biological systems with high spatial and temporal resolution will enable novel optical techniques for fundamental scientific research and its application to medicine [143]. The large size of reconfigurable table-top optical devices prevents many of the promising applications of optics to be implemented *in vivo* for biological studies or for medical diagnostics. In neuroscience, it prevents the use of optogenetics to understand the spatial and temporal role of neural activity deep within the brain[115, 114, 113, 121, 122]. Nanophotonics enables miniaturized optical devices to control the phase and amplitude of light and, therefore, the shape and direction of multiple optical beams in a highly scalable way to potentially address these issues [5, 144, 145, 4, 7, 146, 147, 148, 149]. However most reconfigurable nanophotonics devices have only been demonstrated in the near-infrared spectral range, where the tolerances in fabrication due to the longer wavelengths are high. Here we show the first reconfigurable nanophotonic platform in the visible wavelength range to control multiple micron-scale beams and demonstrate its use in the brain to generate unprecedented neural spike patterns *in vivo* with high spatial and temporal precision[1]. We use integrated microheaters to electrically tune the phase of light within a nanoscale interferometer network to create optical beams that are reconfigurable within 20 mi-

[1]Parts of this chapter are currently being prepared as a manuscript for publication and have been presented[150].

croseconds. We use these complex spatiotemporal beam patterns to drive individual neurons reliably with frequencies up to 200 Hz. This shows how we can use light to generate a repeatable neural pattern that could be used to correlate neural activity with different brain functions and behaviors. This demonstration of the full phase and amplitude control of visible light using nanophotonics is the first step towards a compact platform for steering and shaping optical beams for biological applications. This platform is highly scalable because of the ability to multiplex optical signals using multiple degrees-of-freedom of light which has been extensively used in the telecommunications industry. The ability to combine our reconfigurable nanophotonics platform with integrated electronics could lead to large-scale studies in neuroscience and other biomedical fields.

Implantable probes based on nanophotonic technology have the potential to generate scalable high-resolution spatiotemporal optical patterns for neural excitation; however, recent works have been limited to passive devices that depend on slow and inefficient table-top optics for reconfiguration. Nanophotonics uses high index contrast materials and the coherent nature of light to create subwavelength structures such as waveguides to confine, guide, and manipulate light in compact structures. Because these structures are created using nanofabrication techniques utilized by the CMOS industry, nanophotonic structures can be created on a massively parallel scale with flexible layout and integrated with electronics [5, 3, 4, 7]. Neural probes based on arrays of passive waveguide and grating structures using silicon nitride and SU-8 have been developed for minimally invasive multi-point neural excitation [151, 152, 153, 154, 132]. These nanophotonic probes use grating emitters to emit a coherent and collimated beam of light with divergence angles of <1° en-

abling single cell resolution excitation. However, these passive probes cannot generate complex spatial and temporal patterns with high enough resolution because they require external table-top optical components such as galvanometers, piezoelectric actuators, tunable filters, tunable micro-mirrors for reconfiguration, which are typically slow (10-100 ms).

6.2 Active Visible Nanophotonic Platform

We demonstrate an active nanophotonics platform in the visible wavelength range for creating high-resolution spatiotemporal patterns, which uses the increased sensitivity of confined light to small refractive index changes to create fast electrically tunable waveguide structures. A minimal change in the refractive index (<1%) is required for full and fast reconfiguration of a micron-size device. This refractive index change leads to a phase change in light that can be exploited by interferometers, gratings, metasurfaces, phased array structures to switch, steer, and shape optical beams. Driven by the telecommunications industry, near-infrared modulators, switches and reconfigurable filters based on active nanophotonics have been demonstrated with speeds beyond a GHz and networks with up to 1024 components with minimal footprint [3, 147, 155, 19].

In the visible range from 400 to 600 nm relevant to optogenetic excitation, there have been no demonstrations of active photonic devices due to their sensitivity to fabrication tolerances. Interferometric-based devices require good control of polarization and spatial modes for good extinction. In the visible wavelength range these typical fabrication tolerances become closer to the wavelength, which makes them more sensitive to errors[92].

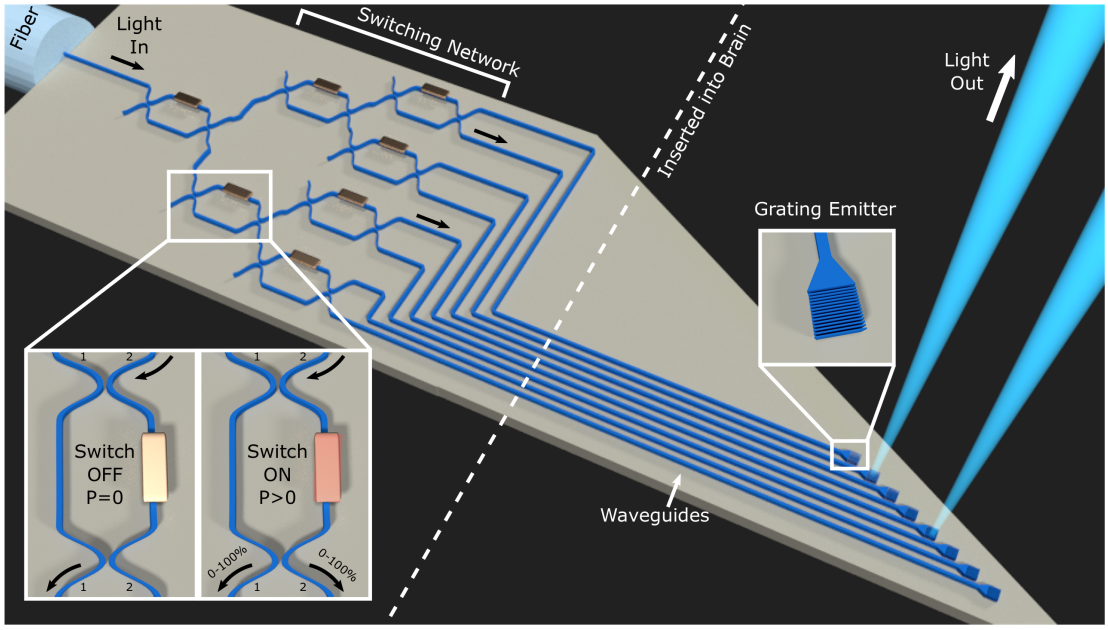

Figure 6.1: **Nanophotonic switch for optogenetic neuromodulation.** a) Schematic of the nanophotonic neural probe. The light enters the structure through a single waveguide at the top. Next, it is routed through the nanophotonic switching network based on 1x2 switches to the 8 grating emitters located at the tip of the probe where the light is emitted out of plane for depth-specific optogenentic control *in vivo*. The routing network remains outside the brain. Inset: Shows a single 1x2 microswitch that routes light between two ports. When the switch is off (P = 0, left), if light enters through input port 2, the light exits through output port 1. As the power on the switch is increased (P ¿ 0, right), the light can be continuously tuned between output port 1 and output port 2 from 0 to 100%, until the light is completely in port 2. If the light enters through input port 1, light exits through output port 2 by default and can be continuously tuned to exit through output port 1.

We use fabrication tolerant design of silicon nitride nanophotonic structures which are transparent in the visible wavelengths. We use high confinement waveguides with a width of 350 nm and height of 200 nm. Low loss high confinement silicon nitride structures have enabled applications such as biological particle and ion trapping, nonlinear optics, quantum optics, and spectroscopy in a wide wavelength range from the visible to mid-infrared. Losses as low as 0.0043 dB/cm in the near-infrared wavelength range and 0.6 dB/cm at 600 nm have been reported [30, 31].

In order to introduce reconfigurability to this platform, we use the thermo-optic effect to reconfigure interferometric switches at speeds suitable for studying neural processes. We place a microheater above the waveguide to induce a localized change in temperature within the waveguide. We exploit this change in index, $\frac{dn}{dT} \sim 4 \times 10^{-5} K^{-1}$, to control the phase of light which allows for switching when embedded in an interferometer. The relatively high-index contrast of silicon nitride allows us to make compact structures, which allow for efficient and fast microheaters with milliwatt and microsecond operation [32]. The thermo-optic effect is fast enough for most biological processes including neuron activation [16]. Specifically, the visible wavelength regime allows one to create smaller devices and bring the microheater closer to the waveguide without inducing loss which improve the microheaters efficiency and speed.

The platform consists of an implantable silicon probe with an embedded nanophotonic micro-switch network located outside of the brain that determines the spatial distribution of 473 nm light beamed out of the probe for neural excitation. Figure 6.1 shows the schematic of the implantable probe based on the silicon nitride waveguide structures. Light is input through a fiber at the

top of the device into a single waveguide which is sent to the switching network based on cascaded 1x2 micro-switches. Depending on the power applied to this analog switch, the light can be output from the two output ports from 0-100% (See inset of Fig. 6.1). The output of the routing network is sent to grating emitters located at the bottom of the probe that send the light outward to excite the neurons. By cascading multiple 1x2 switches, we create an 8-channel probe by creating a 1x8 switching network with waveguides that lead to 8 grating emitters. In order to ensure that negligible temperature change occurs in the brain tissue, the switching network is located on the same chip but outside of the brain tissue during insertion. This defers from previous demonstrations of micro-LED-based probes, in that routing waveguides allow for the electrical control to be well separated from the emitters themselves. This avoids electrical and thermal issues that could disrupt brain activity or neural recordings.

6.2.1 Device Design

Each 1x2 switch is composed of a balanced silicon nitride Mach-Zehnder interferometer which has a platinum microheater that provides the refractive index change in one arm to induce a phase change from 0 to π. The 200 nm height and 350 nm width of the silicon nitride waveguides ensures that the structure is primarily single mode. We place the microheater as close above the waveguide before the mode is perturbed to improve the efficiency of the microheater, which is 660 nm (see Fig. 6.2a). The temperature falls off at approximately 30 μm away, so we keep the other arm of the Mach-Zehnder interferometer at least this distance away (see Fig. 6.2b). In this particular device, we use a distance of 160 μm and a length of 300 μm. The length of this arm is determined by current

and voltage rating of the power supply that will be used as described in Chapter 2.

To create high extinction 1x2 switches, we design fabrication tolerant beamsplitters using multimode interferometers (MMI's). As seen in Chapter 2, the extinction of an interferometer is determined by how close the beamsplitter's splitting ratio is to 50:50 (see Eq. 2.25). The deviation from the peak operation point of a multimode interferometer still keeps the splitting ratio balanced while its overall loss increases. However, deviation from the peak operational point of a directional coupler makes the splitting ratio unbalanced in both directions which creates an unbalanced splitting ratio, but has lower loss. Therefore, we choose an MMI because it remains balanced, and high extinction, over a large wavelength range. The MMI width is 1.2 μm and length is 12.6 μm (see Fig.6.2c for numerical simulation of this structure).

The gratings are designed to be apertures to emit a beam of collimated light around 20 μm diameter. They are designed to emit light $\sim 1^{\circ}$, using Eq. 2.20, so we use a period of 260 nm. We use adiabatic tapers to increase the waveguide to the size of the grating.

A few design measures were taken to mediate the coupling and propagation losses. Because we use butt coupling at the input, a horn taper is used that starts with a waveguide width of 3 μm (fiber core size) and tapers down to the single mode width. Inverse tapers in which the mode is expanded using a narrow waveguide are difficult to construct at these wavelengths due to limitations in fabrication. We broaden the width of the waveguides to 700 nm for the long waveguides that travel down the shank for 5 mm to reduce the scattering losses from the side walls and stitching effects from field boundaries during electron

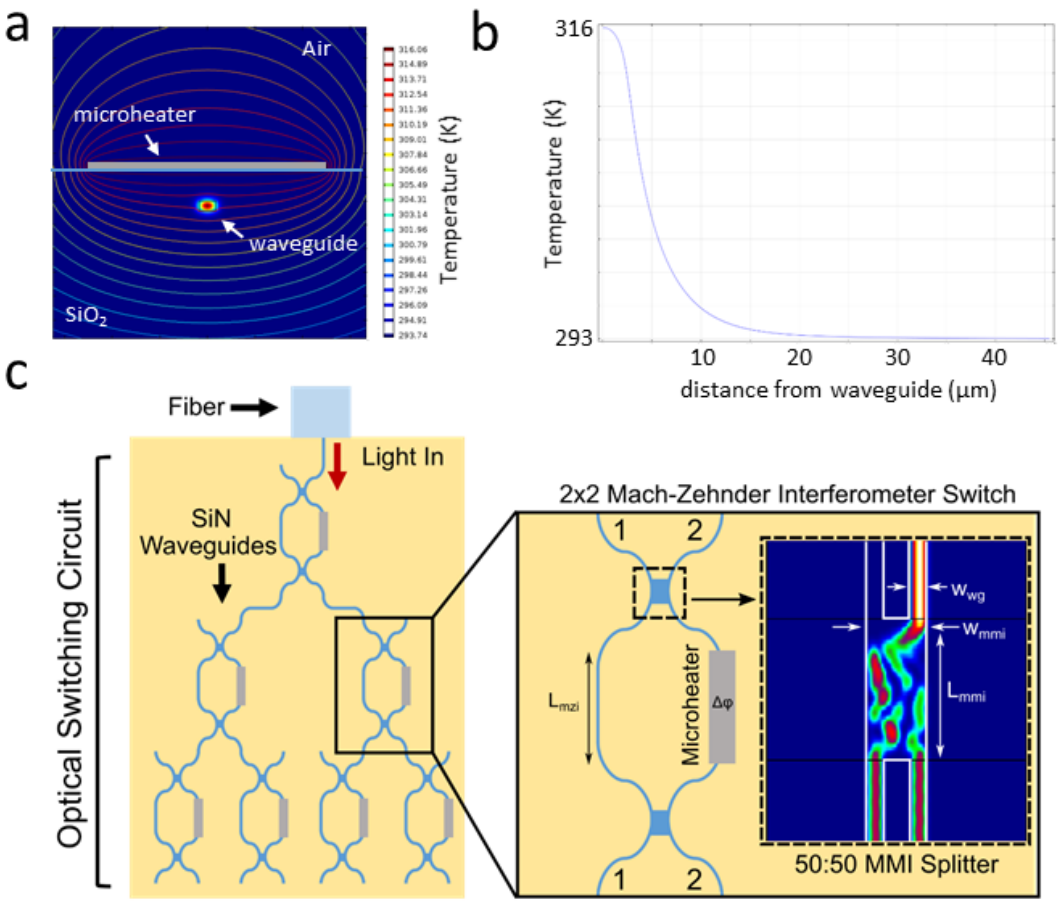

Figure 6.2: **Thermo-Optic Switch Device Design.**The thermo-optic switch is based on a Mach-Zehnder Interferometer (MZI) created using SiN waveguides and a Pt microheater. The phase difference $\Delta\phi$ is proportional to the change in index and L_{mzi}. For the splitter we use a multimode interferometer (MMI), with a length L_{mmi} of 12.6 μm and w_{mmi} of 1.2 μm. An MMI uses higher order modes and the self-imaging principle to create fabrication tolerant, compact, and fairly polarization insensitive structures for splitting light. The inset shows a numerical simulation (Eigenmode Expansion Method, FIMMWAVE software) of the normalized intensity of the light when light is input through port 2. The structure behaves identically, if light is input through the port 1 instead.

beam lithography.

6.3 Device Fabrication and Packaging for *In Vivo* Experiment

To show bidirectional neural interfacing *in vivo*, we performed simultaneous light stimulation and extracellular recording by packaging the device with tungsten recording electrodes aligned near the grating emitters. Here we show an overview of the packaging of the device (see Fig. 6.3). The first four steps are the same as described in Chapter 2. In addition, we thin the chips using backside Bosch etching with a protective polymer called Protek-25.

6.3.1 Electrical Packaging

A printed circuit board (PCB) is designed to route the electrical control from the switches to a pin connector which can be accessed via ribbon cable. First, we attach the chip to the printed circuit board using uv-curable adhesive (NOA-61). The chip must be mounted carefully to ensure the tip extends past the PCB (about 4 mm), so it can be inserted. Similarly, the leveling of the chip must be flat to prevent difficulties in fiber packaging. Next the chip is wire bonded to the PCB traces using aluminum wire, which works well with platinum contacts. The wire bonds are covered in uv-curable adhesive, similar to the glob-top method used in standard electrical circuit packaging. This is critical to ensure the wire bonds are protected from water and saline which can cause corrosion to the metal wires and damage the wire bonds. Special precaution is taken to prevent the adhesive from covering the waveguide input facet using a cover-

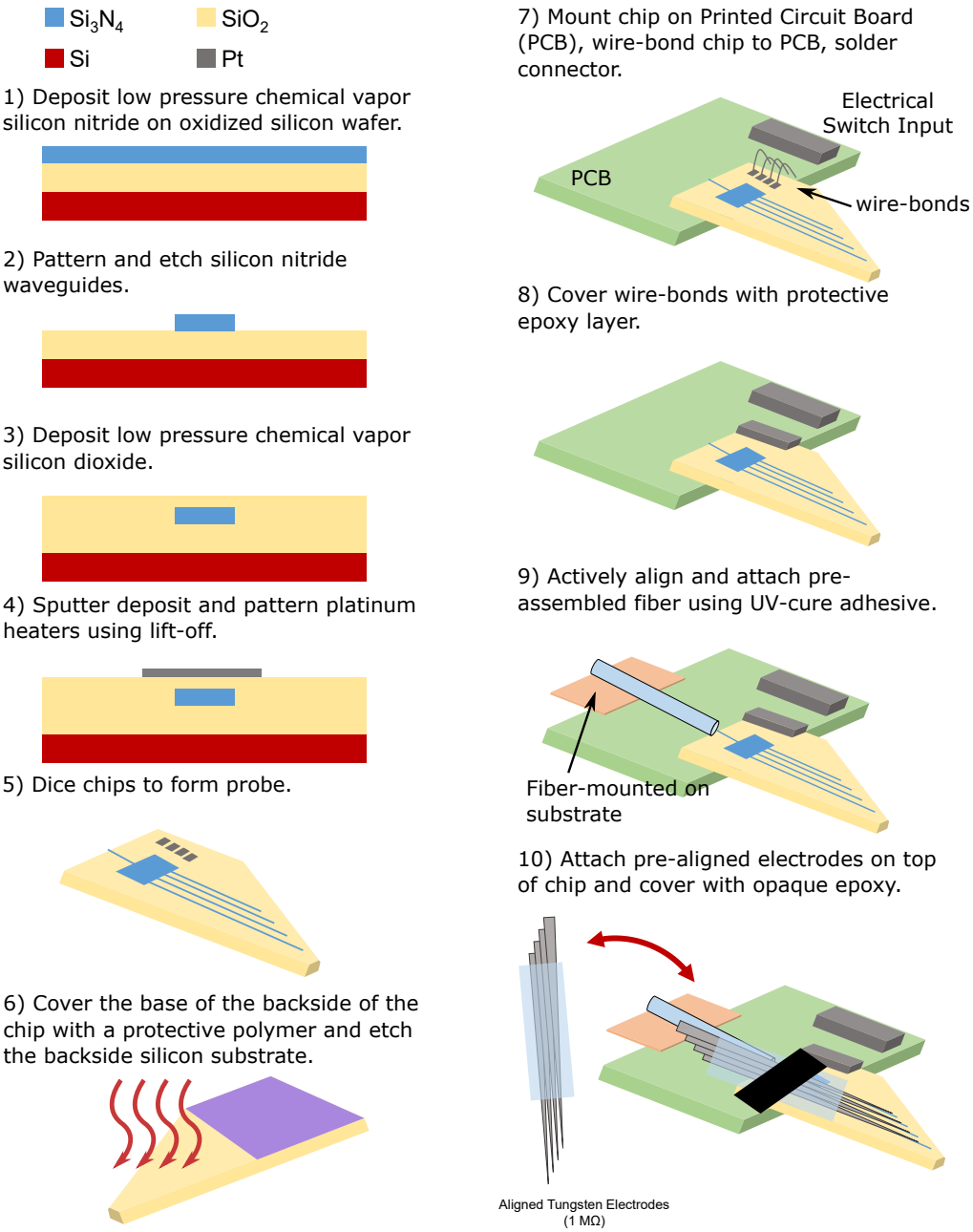

Figure 6.3: ***In Vivo* Device Fabrication and Packaging.**

slip glass and anti-adhesive (Rain-X) aligned with a micro-manipulator stage. Finally, a standard pinhead connector is soldered to the PCB to complete the electrical packaging.

6.3.2 Fiber Packaging

Robust fiber packaging is critical for *in vivo* experiments that will use the nanophotonics platform. The alignment of the fiber, especially in the blue wavelength range, is very sensitive because one must use horn tapers instead of inverse tapers at these small wavelengths due to fabrication tolerances. This alignment must stay in tact as the probe is inserted into the animal and must withstand any large head movements.

We have developed a method that allows for edge coupling with any fiber (lensed or cleaved). First the fiber is attached to a larger piece of glass or silicon with the fiber tip extending about 1-2 mm. This fiber assembly is next aligned using a micro-positioning stage. A small amount of adhesive is placed toward the edge under the fiber assembly and cured in multiple steps, allowing for re-alignment between each step. Previous attempts at attaching fibers in which the fiber is glued directly to the chip has been unreliable because as the glue cures in uv, it contracts leading to misalignment that is permanent. By creating a larger rigid substrate, the fiber assembly, to glue to another large rigid substrate, the PCB, the force of the contraction of the glue is not enough to severely misalign the fiber. Care must be taken to ensure the gap between the fiber assembly and the PCB are not too small because the forces due to capillary action in a small gap (<100 μm) can be very large.

In our case, because we are packaging neural recording electrodes as well on top of the chip, special precaution was taken to minimize any bumps above the fiber that would prevent the recording electrodes from sitting close to the grating outputs. We used fiber assembly in which the fiber is embedded within the glue, so that the top of the glue is flush with the top of the fiber. Therefore, the fiber assembly had to sit with the substrate facing towards the PCB to minimize the bump on the top, so this gap was approximately 300 μm.

Of course grating couplers can be used to couple the fiber which can have a much higher alignment tolerance. However, special precaution must be taken to get the angle of emission correct from the grating. Also, these couplers are not as broadband as edge couplers.

6.3.3 Neural Recording Electrode Packaging

For the neural recordings we use tungsten electrodes that we manually align near each grating output. We keep the recording electrode within 20-30 microns of the grating. We avoid placing the tip of the electrode directly on top of the grating output because this can cause the light-induced artifact that can obscure the neural signals (see Fig. 6.4). It is an open question the proper configuration of these electrodes to the micron-scale beams for optimal neural excitation and recording. For the devices with an array of electrodes, we pre-align the electrodes by embedding the array in uv-curable adhesive that is set in a mold covered with anti-adhesive. This molding procedure allows one to cleanly remove the embedded array of recording electrodes, which can be made to be ~100 μm thick about the size of the recording electrodes. This can be placed

on top of the fiber assembly and aligned very closely with the gratings on the chip. Finally, another opaque black epoxy is used at the top of the chip to fix the recording electrodes to the chip. This prevents any misalignment of the recording electrodes during insertion. We choose an opaque black epoxy to prevent the stray light from the input fiber from traveling into the brain, which can be another source for the light-induced artifact.

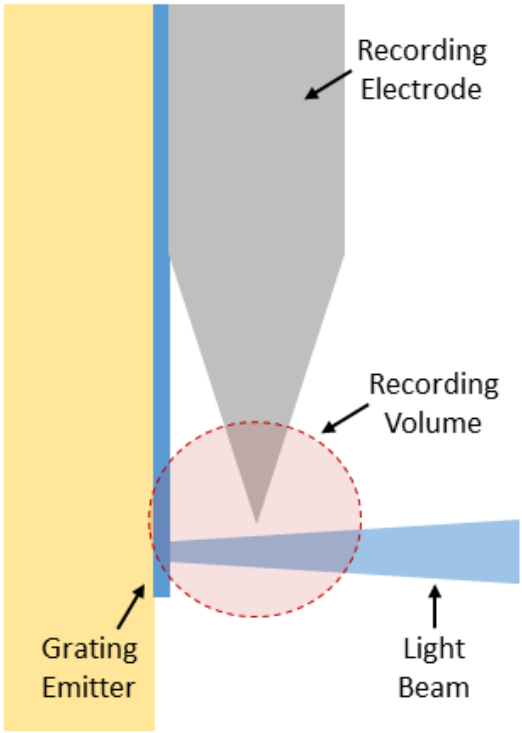

Figure 6.4: **Recording electrode to light beam configuration.**

6.4 Optical Device Performance

6.4.1 1x2 Switch Optical Transmission

To create high resolution spatial patterns, we designed switches with high ON/OFF contrast ratios of 17 dB allowing for a large number of closely spaced emitters that do not leak light to their neighbors. Figure 6.5a shows a microscope image and scanning electron microscope (SEM) image of the fabricated and packaged device. In Fig. 6.5c, we show the switching power, or the power required to switch the light completely from port 1 to port 2 is approximately 30 mW. The extinction ratio, or ON/OFF contrast ratio, between the two outputs of the device is about 50:1 or 17 dB. The efficiency of this device can be improved using light-recycling methods and improving thermal delivery to the waveguide.

6.4.2 1x2 Switch Speed Characterization

Due to the micron-scale size of the device, this platform enables reconfiguration on a time scale of 20 microseconds which is faster than the neural activity time scale. The plot in Fig. 6.5d shows the transient time scale of the optical light in port 1 as a heater is turned OFF and the light switches from output port 2 to output port 1. The speed of the device is limited by this slower heater cooling time response of 20 microseconds. This switching speed is much faster than necessary for most optogenetics experiments[98].

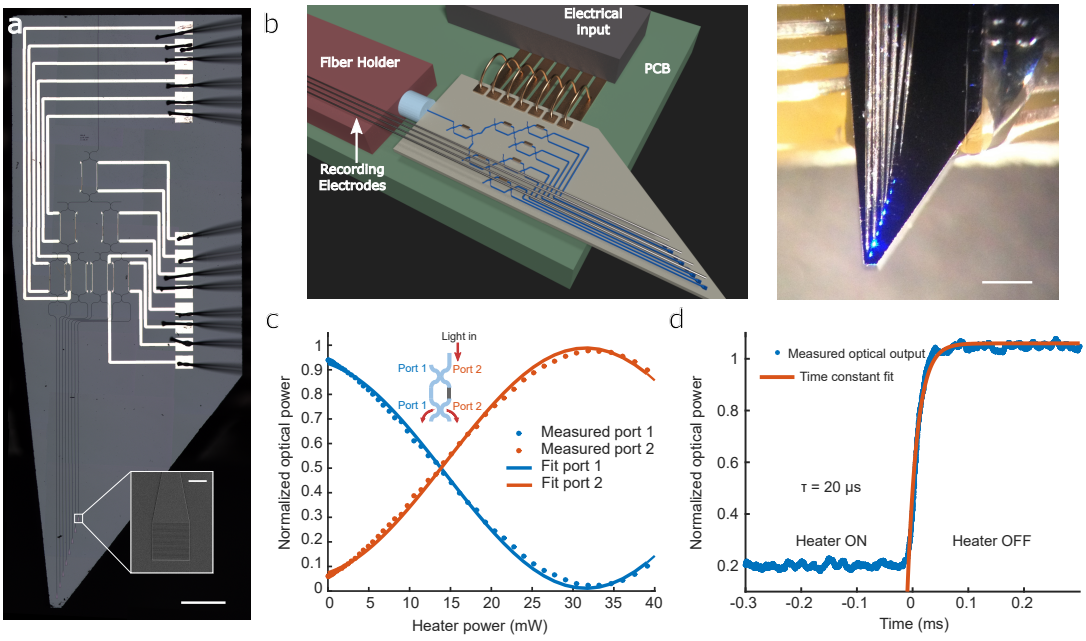

Figure 6.5: **Performance of fabricated nanophotonic switch.** a) Microscope image of the fabricated chip (scale bar is 500 μm). Inset shows scanning electron microscope image of the grating emitter (scale bar is 10 μm). b) Left, the schematic shows the fiber and electrical packaging of the neural probe. Right, microscope image of the packaged device with electrodes aligned near the emitters (~20 μm) and 473 nm optical output (scale bar is 500 μm). c) Plot shows normalized optical output power measured through output port 1 and output port 2 of the MZI switch, when light is input through input port 2. For a single switch, the measured switch power for full conversion from output port 1 to output port 2 is 30 mW and the ON:OFF contrast ratio is 50:1 (or 17 dB extinction). d) Plot shows the response time of output port 1 switching on when the heater is turned off. The switching time (τ) is 20 μs, which we calculate by fitting an exponential to the measured optical output.

6.4.3 1x8 Switch Spatial Distribution of Light

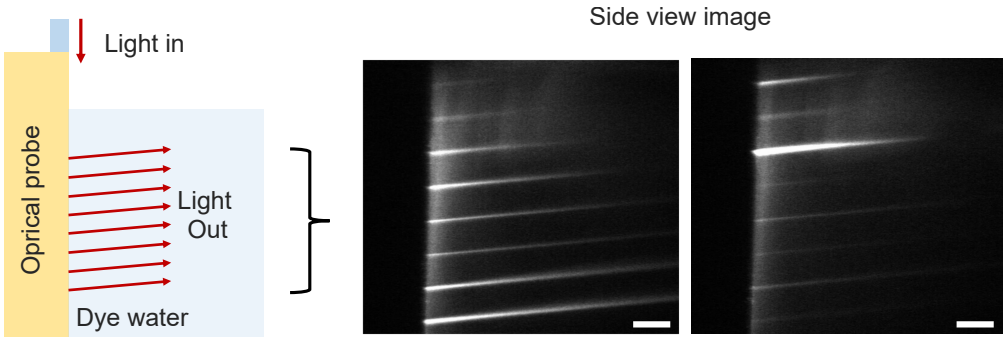

Figure 6.6: **Fluorescent imaging of spatial light distribution.**Left: Schematic of imaging of spatial distribution of light output from the nanophotonic probe in fluorescent dye from the side. Right: Side view of the grating emitters with 473 nm blue light transmitting through Alexa-Fluor 488 dye (scale bar is 125 μm).

To demonstrate the arbitrary reconfiguration of a high-resolution spatial output patterns, we image the light distribution of an 8-channel probe with different switch configurations. First, we image the probe from the side as it excites fluorescent dye (Alexa Fluor 488) to show the grating emitters produce a beam with low divergence (See Fig. 6.6). Based on near-field imaging of our grating emitter, we measure the divergence angle to be 2.2° transverse to the waveguide propagation and 3.75° along the waveguide propagation. From this we estimate a conical volume that is enlarged by light scattering of light. Assuming a density of approximately 1 neuron every $30\mu m \times 30\mu m \times 30\mu m$, we estimate this volume excites approximately 3 neurons. By applying different amounts of power to different switches in the switching network, we can create different optical patterns of highly collimated beams. We show microscope images of the

8 spots being illuminated independently with low cross-talk and details on the switch configurations necessary to achieve different states (see Fig. 6.7).

With 50 mW input power, we estimate an optical power density of approximately of 15 mW/mm incident upon a neuron 100 μm away, including scattering. This power is much larger than the optical threshold for neural excitation cited in literature which ranges from 0.4 mW/mm^2 to 10 mW/mm^2 [122]. The primary loss in the device comes from coupling losses due to the mode-mismatch from the fiber to the waveguide, which can be improved using an adiabatic coupler at the input [156]. The propagation losses can be minimized using multi-pass electron beam lithography which smooths sidewall roughness and reduces scattering losses [30].

6.5 *In Vivo* Demonstration of Neural Switching

6.5.1 Characterization of Single 1x2 Switch *In Vivo*

For the *in vivo* experiment, we choose a mouse line that allows for direct and fast targeting of neurons. We used Gad2-IRES-Cre knock-in mice (Jackson Labs, #010802) and injected the Cre-dependent AAV-EF1a-DIO-CHETA-eYFP vector into 3 sites targeting the visual cortex and hippocampus (Anterior-Posterior: 3.2 mm, Medial-Lateral: 2.4 mm, Dorsal-Ventral: 0.4 mm, 0.8 mm, 1.5 mm; 0.2 μl per site). ChETA is a ChR2 variant that allows neurons to be driven by light at high frequencies (>40 Hz). The virus delivery results in ChETA expression specifically in cortical and hippocampal Gad2 interneurons. Interneurons are a class of neurons that relay information between other sensory or motor neurons.

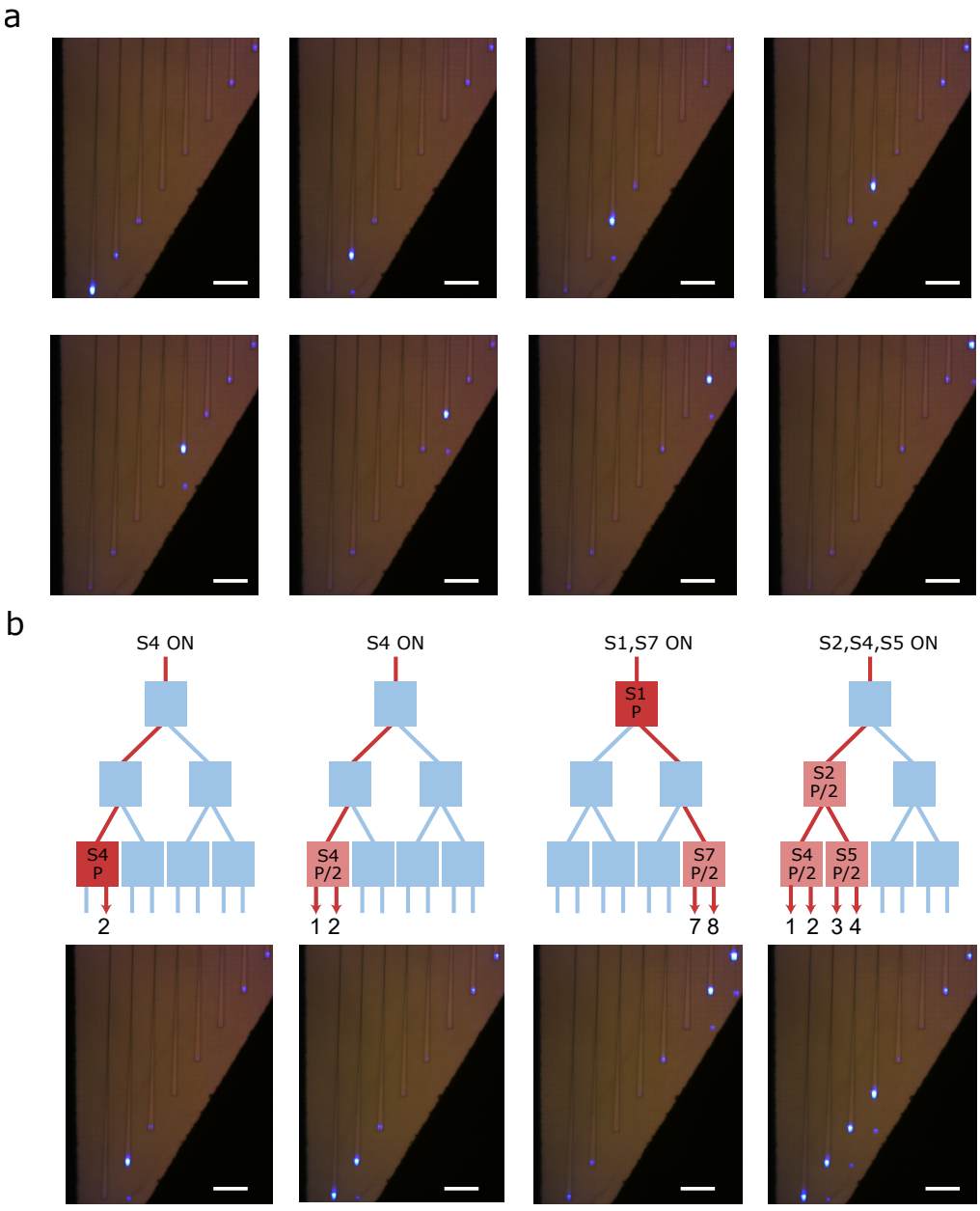

Figure 6.7: **Creating patterns of light using switching network.** a) Microscope images of each of the 8 emitters being turned on individually. b) Examples of detailed switch configurations. The light enters through the top and exits through arrows indicated below. Switches indicated by a blue box are off, and switches in solid red are on. P indicates full power and P/2 indicates half the power.

We chose this mice line because Gad2 interneurons locally inhibit other pyramidal neurons, minimizing the indirect activation of cells that are not expressing ChETA. The integrated device was implanted into the same viral injection sites in a head-fixed anesthetized mouse.

Figure 6.8 shows a diagram of the experiment including the neural recording system (Neuralynx). Noise is a critical issue during electrophysiology experiments because the extracellular neural signals are in the tens of μV regime. The headstage provides unity gain amplification. This improves the common mode rejection ratio (CMRR) performance for the entire recording system. This better CMRR allows for better artifact and other common mode noise signal rejection. During the neural recording we filter from 0.6-6 kHz which captures all of the frequency components of the neural spike signal. The neural data was processed by our neuroscience collaborator, Qian Li from Adam Kepecs' group at Cold Spring Harbor using the same spike sorting procedures outlined in a previous journal article [157].

Using a single switch, we show the ability to modulate the states of two distinct neurons located 875 um apart with driving frequencies up to 200 Hz and a neuron firing rate of 100 Hz, unprecedented in implantable probes to date. As shown in Fig. 6.9a, by applying different amounts of power to switch 1 (S1) in the switching network, we can direct a highly collimated beam towards either the top or the bottom emitter, each targeting layer 2/3 of the visual cortex and hippocampus CA1 respectively (beam 1-2). We only show the electrodes (Ch 1-2, grey lines) on the diagram that recorded neurons.

We recorded 2 single neurons using spike sorting procedures one near Ch1 and one near Ch2 that follow the states of the light beams dictated by switch 1

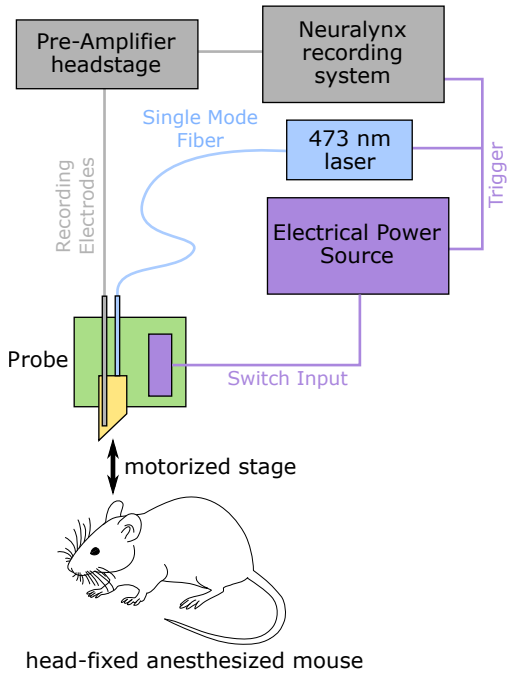

Figure 6.8: **Experimental setup for *in vivo* experiment.**

(S1). By aligning spike events to the onset of 1-ms light beam in spike raster and peri-stimulus time histogram (Fig. 6.9b), each directly activated neuron showed robust spike firing activities with short first-spike latency and small jitter. By applying light stimulation with different frequencies (Fig. 6.9c), we found that both neurons were capable of being driven with high fidelity when the light beam was switched up to 200 Hz (actual firing rate of the individual neurons were 100 Hz). These driving frequencies have not been shown in previous implantable probes.

Occasionally, we isolated additional non-Gad2 pyramidal neurons from the same recording electrode that shows an inhibition rather than activation. This is another confirmation that our Gad2 interneurons are being activated because they cause an inhibition effect. This also shows that the recording electrode

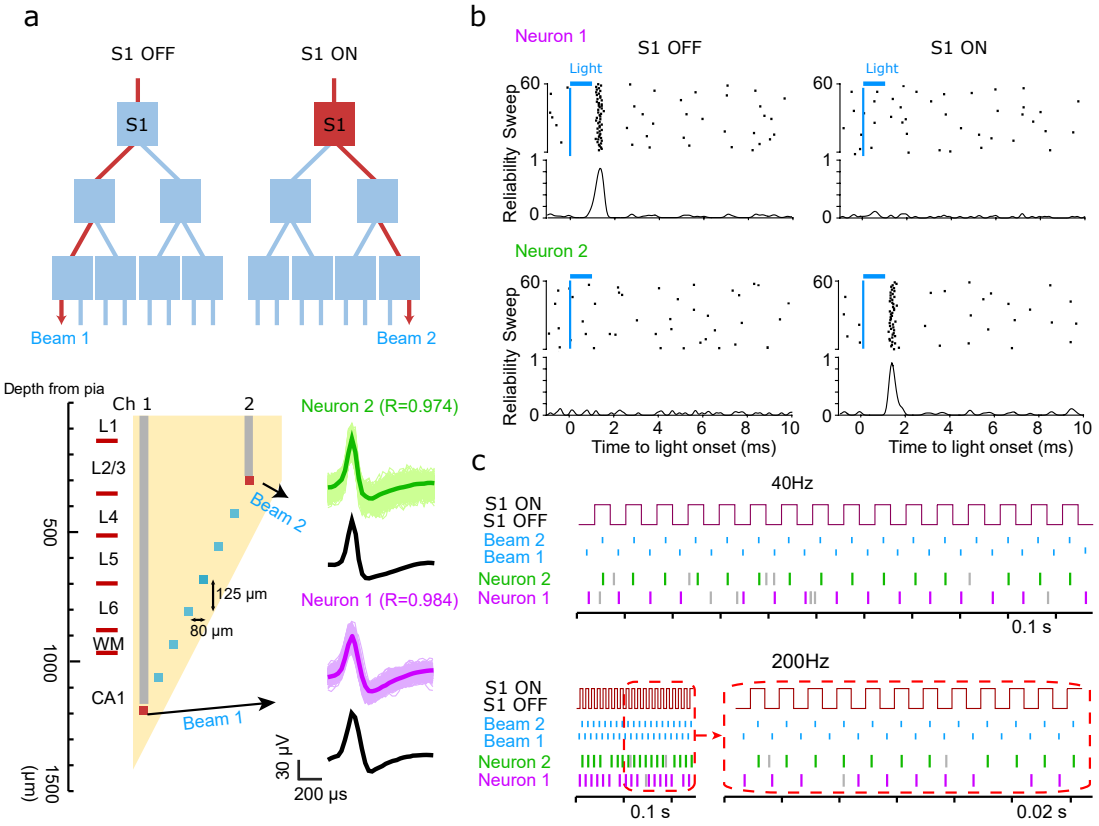

Figure 6.9: **In-vivo characterization of single switch (S1).** a) Top: switch diagram shows how S1 state (OFF or ON) determines the beam direction (beam 1 or 2). Bottom: schematic of beam and electrode arrangement for single switch *in vivo* experiment. The depth of each recording site is indicated on the left. Electrode channel 1 and 2 (Ch 1-2 in grey lines) are positioned next to beam 1 and 2 (red squares separated by 875 m in depth). From each recording site, a single neuron (Neuron 1-2) is identified by evaluating the waveform similarity (R) of averaged spontaneous (colored bold line, superimposed with individual spikes in colored fine lines) and light evoked spikes (black bold line). Individual spontaneous spikes waveforms are shown in colored fine lines).b) Spike raster and peri-stimulus time histograms (PSTH) of Neuron 1 and 2 during switch OFF (left) or ON (right) state. All spike events (black dots) are aligned to light onset (blue line). Bin size: 100 μs . c) Representative spike activities of Neuron 1 and 2, both follow the ON/OFF state of S1 with strong fidelity at both 40 Hz and 200 Hz. The colored line indicates light-activated spike, and the grey line indicates the spontaneous spike.

although it can pick up multiple neurons is only showing single neuron light-induced activity.

6.5.2 Generating Spatiotemporal Neural Spike Patterns *In Vivo*

Finally, we demonstrate the capability of the device to use patterned light beams to drive multiple independent neurons to generate complex spatiotemporal neural spike patterns *in vivo* that are precisely defined and repeatable. Figure 6.10a shows the track of the neural probe that was coated with a fluorescent dye inserted into the brain from a representative insertion. We use a combination of switches to drive 3 different beams at different depths within the mouse (beam 1, beam 2 and beam 3). As shown in Fig 6.10b, three different tungsten electrodes (Ch 1-3, grey lines) were positioned next to 3 emitters located at 250 μm (beam 1 in CA1), 500 μm (beam 2 in Layer 6 in V1), and 1000 μm (beam 3 in Layer 2/3 in V1) from the probe tip. This allowed for selective and independent multi-point excitation and recording of spatially separated neurons along the device. In this particular device, we had an issue with crosstalk between nearest neighbor emitters. For simplicity, we have drawn the beams and electrodes that we independently controlled to generate the neural patterns.

We successfully isolated 3 simultaneously recorded neurons from 3 electrode contacts respectively, each corresponding to illumination emitter at different depths (Ch 1-3). In Fig. 6.10c, we show a representative neural spike pattern generated by our device. The neural spike pattern shows strong correlations with the states of the optical beam. Here we demonstrate a burst pattern at 40 Hz and 200 Hz and random pattern at 40 Hz. These frequencies indicate the

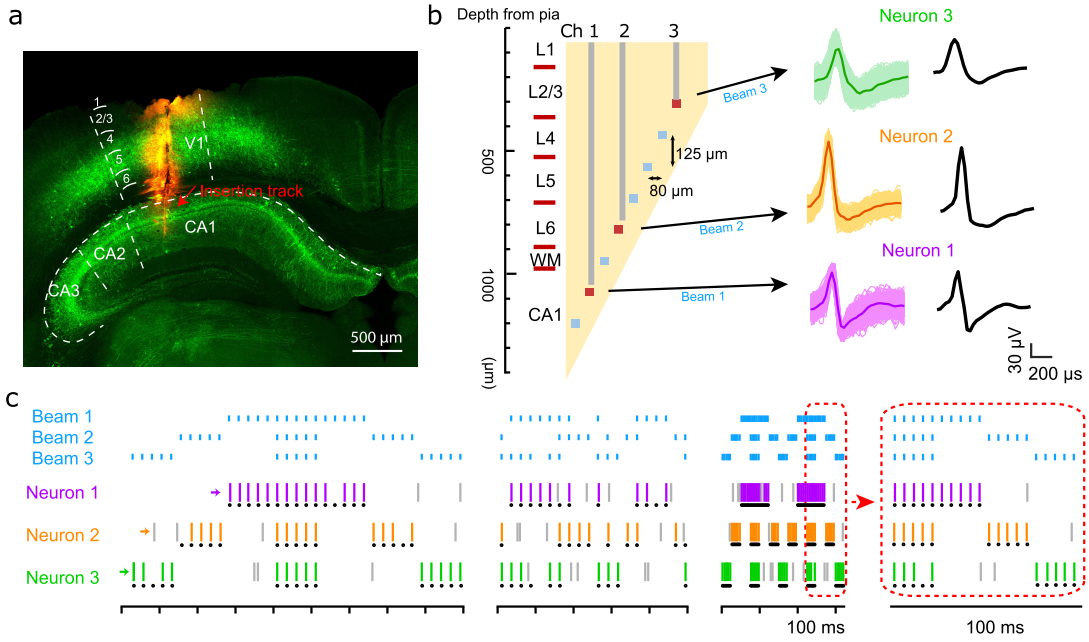

Figure 6.10: **Nanophotonic generation of high spatiotemporal neural spike patterns *in vivo*.** a) Coronal section from a representative insertion where red indicates the probe track. b) Schematic of beam and electrode arrangement for in-vivo demonstration of fast, independent optical control of three ChR2-expressing Gad2 interneurons activity. The depth of each recording site is indicated on the left. For simplicity, we show the 3 recording channels (Ch 1-3 in 3 grey lines) positioned next to beam 1-3 (3 red squares), spanning 750 μm in depth. From each recording site, a single ChR2-expression Gad2 interneuron (Neuron 1-3) is recorded. c) Representative spike trains of 3 individual Gad2 interneurons driven by series of light pulses delivered in 3 patterns: 1) 5-burst regular sequence at 40 Hz, 2) random sequence with highest frequency at 40 Hz, and 3) 5-burst sequence at 200 Hz. The red dotted line box shows a zoom out of the 200 Hz 5-burst sequence. Black dot indicated the timestamp when light evoked spike supposes to occur.

frequency between changing states and light stimulation frequency.

To show that the pattern generation is reliable, we repeat these sequences 10 times and calculate how reliably the neurons can follow these patterns. We quantified the optically evoked responses crossing different stimulation patterns by generating peri-stimulus raster and histogram and measuring the spike firing fidelity (spike reliability in Fig. 6.11a). Here we show the burst pattern and a random repeated pattern over 10 trials (sweeps). The random repeated pattern shows every combination of the three beams can be reproduced reliably by the three neurons.

The trial-to-trial first spike latency and jitter were stable across repeated deliveries of light pulses with different frequencies, demonstrating the device allowing for patterned population neural manipulation with cellular precision and high fidelity. This was measured across five recordings from 4 animals and 12 neurons exhibiting directly light evoked spikes (see Figure 6.11b-c).

6.6 Discussion

This demonstration of reliably generating complex neural spike patterns can be used in neural behavior studies by allowing one to replay previously recorded neural patterns to understand behavior and brain function. To date, most behavior experiments have been limited to single fiber excitation combined with electrophysiology recordings. This would enable more complex experiments that use the localized stimulation of neurons.

In our demonstration, only a specific set of neurons are able to be activated

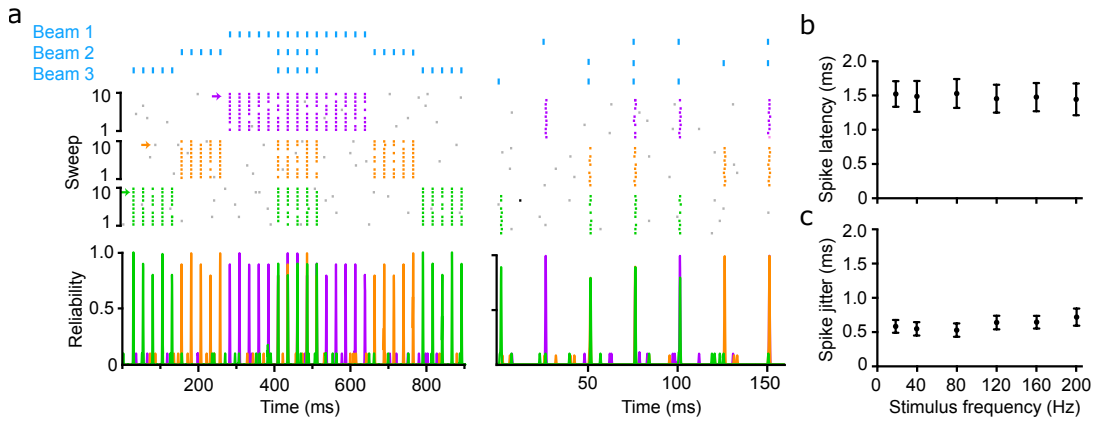

Figure 6.11: **Reliability of *in vivo* neural spike generation.** a) shows representative 10 sweeps of these patterns 3 neurons (following the configuration and color code from the previous figures) in response to the repeated regular (left) and random (right) light stimulation. The peri-stimulus time histogram demonstrates the high reliability of light response. Bin size: 100 μs. b) Summary of trial-to-trial spike latency referring to light onset throughout multiple stimulation frequencies (n=13 sorted neurons from 4 mice). c) Jitter of spike time across repeated light-evoked spike trains throughout multiple stimulation frequencies (n=13 sorted neurons from 4 mice).

by light defined by their genetics. We estimate given the density of these GAD2 neurons, we are activating between 1-2 neurons within 100 μm. For purely single cell activation, the gratings can be designed with a modulated duty cycle to shape the emission of the beam to a focal spot that overlaps with only a single neuron [158, 159]. However, with such high precision one must have a dense array or movable spots for practical use in experiments.

This demonstration of using thermo-optic tuning of the phase on a visible nanophotonic platform is the first step towards a compact platform for steering and shaping optical beams for biological applications. All previous demonstrations of large-scale phased arrays in the near-infrared regime have used thermo-

optic phase tuners because other methods induce too much loss or become prohibitively large [32, 160]. With full control of the phase and amplitude of the light beams one can create arbitrary patterns for excitation and correct for scattering effects using adaptive optics methods.

This platform is highly scalable due to its multiplexing potential. The ability to multiplex optical signals using multiple degrees-of-freedom of light is being used extensively for optical communications applications as discussed in the previous chapters. Each optical channel could potentially be used to redirect light to different spatial locations. For example, wavelength-division multiplexing has been the workhorse of optical transceivers allowing large (100 Gbps) data transfer rates using wavelength channels[1]. More recently, the transverse spatial mode has been used for mode-division multiplexing to further increase the number of channels on the optical communication platform as discussed in the previous chapters of this dissertation[20].

The ability to combine our reconfigurable nanophotonics platform with integrated electronics could lead to a multi-functional platform in which one can both excite optically and record electrical neural signals with high spatiotemporal resolution deep within the brain. This could enable behavior studies in neuroscience that have not been possible to date using existing technologies.

BIBLIOGRAPHY

[1] D. Dai and J. E. Bowers, "Silicon-based on-chip multiplexing technologies and devices for Peta-bit optical interconnects," Nanophotonics **3** (2014).

[2] D. Dai, J. Wang, S. Chen, S. Wang, and S. He, "Monolithically integrated 64-channel silicon hybrid demultiplexer enabling simultaneous wavelength- and mode-division-multiplexing: Monolithically integrated 64-channel silicon hybrid demultiplexer," Laser & Photonics Reviews **9**, 339–344 (2015).

[3] K. Tanizawa, K. Suzuki, M. Toyama, M. Ohtsuka, N. Yokoyama, K. Matsumaro, M. Seki, K. Koshino, T. Sugaya, S. Suda, G. Cong, T. Kimura, K. Ikeda, S. Namiki, and H. Kawashima, "Ultra-compact 32 32 strictly-non-blocking Si-wire optical switch with fan-out LGA interposer," Optics Express **23**, 17599 (2015).

[4] Y. Shen, N. C. Harris, S. Skirlo, M. Prabhu, T. Baehr-Jones, M. Hochberg, X. Sun, S. Zhao, H. Larochelle, D. Englund, and M. Soljai, "Deep learning with coherent nanophotonic circuits," Nature Photonics **11**, 441–446 (2017).

[5] J. Sun, E. Timurdogan, A. Yaacobi, E. S. Hosseini, and M. R. Watts, "Large-scale nanophotonic phased array," Nature **493**, 195–199 (2013).

[6] J. C. F. Matthews, A. Politi, A. Stefanov, and J. L. O'Brien, "Manipulation of multiphoton entanglement in waveguide quantum circuits," Nature Photonics **3**, 346–350 (2009).

[7] N. C. Harris, G. R. Steinbrecher, M. Prabhu, Y. Lahini, J. Mower, D. Bunandar, C. Chen, F. N. C. Wong, T. Baehr-Jones, M. Hochberg, S. Lloyd, and D. Englund, "Quantum transport simulations in a programmable nanophotonic processor," Nature Photonics **11**, 447–452 (2017).

[8] K. Luke, Y. Okawachi, M. R. E. Lamont, A. L. Gaeta, and M. Lipson, "Broadband mid-infrared frequency comb generation in a Si_3n_4 microresonator," Optics Letters **40**, 4823 (2015).

[9] A. Dhakal, P. C. Wuytens, F. Peyskens, K. Jans, N. L. Thomas, and R. Baets, "Nanophotonic Waveguide Enhanced Raman Spectroscopy of Biological Submonolayers," ACS Photonics **3**, 2141–2149 (2016).

[10] E. Knill, R. Laflamme, and G. J. Milburn, "A scheme for efficient quantum computation with linear optics," Nature **409**, 46–52 (2001).

[11] A. Politi, J. C. F. Matthews, and J. L. O'Brien, "Shors Quantum Factoring Algorithm on a Photonic Chip," Science **325**, 1221–1221 (2009).

[12] A. Politi, M. J. Cryan, J. G. Rarity, S. Yu, and J. L. O'Brien, "Silica-on-Silicon Waveguide Quantum Circuits," Science **320**, 646–649 (2008).

[13] J. B. Spring, B. J. Metcalf, P. C. Humphreys, W. S. Kolthammer, X.-M. Jin, M. Barbieri, A. Datta, N. Thomas-Peter, N. K. Langford, D. Kundys, J. C. Gates, B. J. Smith, P. G. R. Smith, and I. A. Walmsley, "Boson Sampling on a Photonic Chip," Science **339**, 798–801 (2013).

[14] M. Tillmann, B. Daki, R. Heilmann, S. Nolte, A. Szameit, and P. Walther, "Experimental boson sampling," Nature Photonics **7**, 540–544 (2013).

[15] A. Crespi, R. Osellame, R. Ramponi, D. J. Brod, E. F. Galvo, N. Spagnolo, C. Vitelli, E. Maiorino, P. Mataloni, and F. Sciarrino, "Integrated multimode interferometers with arbitrary designs for photonic boson sampling," Nature Photonics **7**, 545–549 (2013).

[16] E. S. Boyden, F. Zhang, E. Bamberg, G. Nagel, and K. Deisseroth, "Millisecond-timescale, genetically targeted optical control of neural activity," Nature Neuroscience **8**, 1263–1268 (2005).

[17] D. Dai, Y. Tang, and J. E. Bowers, "Mode conversion in tapered submicron silicon ridge optical waveguides," Optics Express **20**, 13425–13439 (2012).

[18] H. Haus, "Coupling of Modes - Resonators and Couplers," in "Waves and Fields in Optoelectronics," (Prentice Hall, Inc., New Jersey, 1984).

[19] L. Lu, S. Zhao, L. Zhou, D. Li, Z. Li, M. Wang, X. Li, and J. Chen, "16 16 non-blocking silicon optical switch based on electro-optic Mach-Zehnder interferometers," Optics Express **24**, 9295 (2016).

[20] L.-W. Luo, N. Ophir, C. P. Chen, L. H. Gabrielli, C. B. Poitras, K. Bergmen, and M. Lipson, "WDM-compatible mode-division multiplexing on a silicon chip," Nature Communications **5** (2014).

[21] J. Wang, P. Chen, S. Chen, Y. Shi, and D. Dai, "Improved 8-channel silicon

mode demultiplexer with grating polarizers," Optics Express **22**, 12799–12807 (2014).

[22] B. Stern, X. Zhu, C. P. Chen, L. D. Tzuang, J. Cardenas, K. Bergman, and M. Lipson, "On-chip mode-division multiplexing switch," Optica **2**, 530 (2015).

[23] D. Ohana, B. Desiatov, N. Mazurski, and U. Levy, "Dielectric Metasurface as a Platform for Spatial Mode Conversion in Nanoscale Waveguides," Nano Letters **16**, 7956–7961 (2016).

[24] D. Ohana and U. Levy, "Mode conversion based on dielectric metamaterial in silicon," Optics Express **22**, 27617–27631 (2014).

[25] J. Lu and J. Vuckovic, "Objective-first design of high-efficiency, small-footprint couplers between arbitrary nanophotonic waveguide modes," Optics Express **20**, 7221–7236 (2012).

[26] Z. Li, M.-H. Kim, C. Wang, Z. Han, S. Shrestha, A. C. Overvig, M. Lu, A. Stein, A. M. Agarwal, M. Lonar, and N. Yu, "Controlling propagation and coupling of waveguide modes using phase-gradient metasurfaces," Nature Nanotechnology **12**, 675–683 (2017).

[27] S. Stopinski, M. Malinowski, R. Piramidowicz, E. Kleijn, M. K. Smit, and X. J. M. Leijtens, "Integrated Optical Delay Lines for Time-Division Multiplexers," IEEE Photonics Journal **5**, 7902109–7902109 (2013).

[28] H. Gu, Z. Wang, B. Zhang, Y. Yang, and K. Wang, "Time-Division-Multiplexing-Wavelength-Division-Multiplexing-Based Architecture for ONoC," IEEE/OSA Journal of Optical Communications and Networking **9**, 351–363 (2017).

[29] H. Okayama, Y. Onawa, D. Shimura, H. Yaegashi, and H. Sasaki, "Polarization rotation Bragg grating using Si wire waveguide with non-vertical sidewall," Optics Express **22**, 31371 (2014).

[30] X. Ji, F. A. S. Barbosa, S. P. Roberts, A. Dutt, J. Cardenas, Y. Okawachi, A. Bryant, A. L. Gaeta, and M. Lipson, "Ultra-low-loss on-chip resonators with sub-milliwatt parametric oscillation threshold," Optica **4**, 619 (2017).

[31] E. Shah Hosseini, S. Yegnanarayanan, A. H. Atabaki, M. Soltani, and A. Adibi, "High quality planar silicon nitride microdisk resonators for

integrated photonics in the visible wavelength range," Optics Express **17**, 14543 (2009).

[32] M. R. Watts, J. Sun, C. DeRose, D. C. Trotter, R. W. Young, and G. N. Nielson, "Adiabatic thermo-optic MachZehnder switch," Optics Letters **38**, 733 (2013).

[33] J. L. O'Brien, "Optical Quantum Computing," Science **318**, 1567–1570 (2007).

[34] N. Gisin, G. Ribordy, W. Tittel, and H. Zbinden, "Quantum cryptography," Reviews of Modern Physics **74**, 145–195 (2002).

[35] H. J. Kimble, "The quantum internet," Nature **453**, 1023–1030 (2008).

[36] N. M. Linke, D. Maslov, M. Roetteler, S. Debnath, C. Figgatt, K. A. Landsman, K. Wright, and C. Monroe, "Experimental comparison of two quantum computing architectures," Proceedings of the National Academy of Sciences **114**, 3305–3310 (2017).

[37] J. W. Silverstone, D. Bonneau, J. L. O'Brien, and M. G. Thompson, "Silicon Quantum Photonics," IEEE Journal of Selected Topics in Quantum Electronics **22**, 390–402 (2016).

[38] I. Aharonovich, D. Englund, and M. Toth, "Solid-state single-photon emitters," Nature Photonics **10**, 631–641 (2016).

[39] P. C. Humphreys, B. J. Metcalf, J. B. Spring, M. Moore, X.-M. Jin, M. Barbieri, W. S. Kolthammer, and I. A. Walmsley, "Linear Optical Quantum Computing in a Single Spatial Mode," Physical Review Letters **111**, 150501 (2013).

[40] A. Crespi, R. Ramponi, R. Osellame, L. Sansoni, I. Bongioanni, F. Sciarrino, G. Vallone, and P. Mataloni, "Integrated photonic quantum gates for polarization qubits," Nature Communications **2**, 566 (2011).

[41] J. M. Lukens and P. Lougovski, "Frequency-encoded photonic qubits for scalable quantum information processing," Optica **4**, 8 (2017).

[42] M. Chen, N. C. Menicucci, and O. Pfister, "Experimental Realization of Multipartite Entanglement of 60 Modes of a Quantum Optical Frequency Comb," Physical Review Letters **112**, 120505 (2014).

[43] Z. Xie, T. Zhong, S. Shrestha, X. Xu, J. Liang, Y.-X. Gong, J. C. Bienfang, A. Restelli, J. H. Shapiro, F. N. C. Wong, and C. Wei Wong, "Harnessing high-dimensional hyperentanglement through a biphoton frequency comb," Nature Photonics **9**, 536–542 (2015).

[44] M. Pysher, Y. Miwa, R. Shahrokhshahi, R. Bloomer, and O. Pfister, "Parallel Generation of Quadripartite Cluster Entanglement in the Optical Frequency Comb," Physical Review Letters **107**, 030505 (2011).

[45] R. H. Hadfield, "Single-photon detectors for optical quantum information applications," Nature Photonics **3**, 696–705 (2009).

[46] F. Najafi, J. Mower, N. C. Harris, F. Bellei, A. Dane, C. Lee, X. Hu, P. Kharel, F. Marsili, S. Assefa, K. K. Berggren, and D. Englund, "On-chip detection of non-classical light by scalable integration of single-photon detectors," Nature Communications **6** (2015).

[47] S. Yokoyama, R. Ukai, S. C. Armstrong, C. Sornphiphatphong, T. Kaji, S. Suzuki, J.-i. Yoshikawa, H. Yonezawa, N. C. Menicucci, and A. Furusawa, "Ultra-large-scale continuous-variable cluster states multiplexed in the time domain," Nature Photonics **7**, 982–986 (2013).

[48] J. I. Cirac and H. J. Kimble, "Quantum optics, what next?" Nature Photonics **11**, 18–20 (2017).

[49] A. G. Fowler, M. Mariantoni, J. M. Martinis, and A. N. Cleland, "Surface codes: Towards practical large-scale quantum computation," Physical Review A **86** (2012).

[50] E. Martn-Lpez, A. Laing, T. Lawson, R. Alvarez, X.-Q. Zhou, and J. L. O'Brien, "Experimental realization of Shor's quantum factoring algorithm using qubit recycling," Nature Photonics **6**, 773–776 (2012).

[51] X.-s. Ma, B. Dakic, W. Naylor, A. Zeilinger, and P. Walther, "Quantum simulation of the wavefunction to probe frustrated Heisenberg spin systems," Nature Physics **7**, 399–405 (2011).

[52] Y. Wang, H. Yun, Z. Lu, R. Bojko, W. Shi, X. Wang, J. Flueckiger, F. Zhang, M. Caverley, N. A. F. Jaeger, and L. Chrostowski, "Apodized Focusing Fully Etched Subwavelength Grating Couplers," IEEE Photonics Journal **7**, 1–10 (2015).

[53] W. J. Munro, K. A. Harrison, A. M. Stephens, S. J. Devitt, and K. Nemoto, "From quantum multiplexing to high-performance quantum networking," Nature Photonics **4**, 792–796 (2010).

[54] H.-J. Briegel, W. Dr, J. I. Cirac, and P. Zoller, "Quantum Repeaters: The Role of Imperfect Local Operations in Quantum Communication," Physical Review Letters **81**, 5932–5935 (1998).

[55] M. Fox, *Quantum Optics: An Introduction* (Oxford University Press, New York, NY, USA, 2006).

[56] M. Reck, A. Zeilinger, H. J. Bernstein, and P. Bertani, "Experimental realization of any discrete unitary operator," Physical Review Letters **73**, 58–61 (1994).

[57] C. K. Hong, Z. Y. Ou, and L. Mandel, "Measurement of subpicosecond time intervals between two photons by interference," Physical Review Letters **59**, 2044–2046 (1987).

[58] Z. Y. Ou, E. C. Gage, B. E. Magill, and L. Mandel, "Fourth-order interference technique for determining the coherence time of a light beam," Journal of the Optical Society of America B **6**, 100–103 (1989).

[59] V. Giovannetti, S. Lloyd, and L. Maccone, "Quantum-Enhanced Measurements: Beating the Standard Quantum Limit," Science **306**, 1330–1336 (2004).

[60] B. J. Metcalf, J. B. Spring, P. C. Humphreys, N. Thomas-Peter, M. Barbieri, W. S. Kolthammer, X.-M. Jin, N. K. Langford, D. Kundys, J. C. Gates, B. J. Smith, P. G. R. Smith, and I. A. Walmsley, "Quantum teleportation on a photonic chip," Nature Photonics **8**, 770–774 (2014).

[61] M. A. Broome, A. Fedrizzi, S. Rahimi-Keshari, J. Dove, S. Aaronson, T. C. Ralph, and A. G. White, "Photonic Boson Sampling in a Tunable Circuit," Science **339**, 794–798 (2013).

[62] S. Aaronson and A. Arkhipov, "The Computational Complexity of Linear Optics," in "Proceedings of the Forty-third Annual ACM Symposium on Theory of Computing," (ACM, New York, NY, USA, 2011), STOC '11, pp. 333–342.

[63] B. P. Lanyon, M. Barbieri, M. P. Almeida, T. Jennewein, T. C. Ralph, K. J.

Resch, G. J. Pryde, J. L. OBrien, A. Gilchrist, and A. G. White, "Simplifying quantum logic using higher-dimensional Hilbert spaces," Nature Physics **5**, 134–140 (2009).

[64] S. Groblacher, T. Jennewein, A. Vaziri, G. Weihs, and A. Zeilinger, "Experimental quantum cryptography with qutrits," New Journal of Physics **8**, 75 (2006).

[65] T. Zhong, H. Zhou, R. D. Horansky, C. Lee, V. B. Verma, A. E. Lita, A. Restelli, J. C. Bienfang, R. P. Mirin, T. Gerrits, S. W. Nam, F. Marsili, M. D. Shaw, Z. Zhang, L. Wang, D. Englund, G. W. Wornell, J. H. Shapiro, and F. N. C. Wong, "Photon-efficient quantum key distribution using time-energy entanglement with high-dimensional encoding," New Journal of Physics **17**, 022002 (2015).

[66] M. Neeley, M. Ansmann, R. C. Bialczak, M. Hofheinz, E. Lucero, A. D. O'Connell, D. Sank, H. Wang, J. Wenner, A. N. Cleland, M. R. Geller, and J. M. Martinis, "Emulation of a Quantum Spin with a Superconducting Phase Qudit," Science **325**, 722–725 (2009).

[67] A. Mair, A. Vaziri, G. Weihs, and A. Zeilinger, "Entanglement of the orbital angular momentum states of photons," Nature **412**, 313–316 (2001).

[68] N. K. Langford, R. B. Dalton, M. D. Harvey, J. L. OBrien, G. J. Pryde, A. Gilchrist, S. D. Bartlett, and A. G. White, "Measuring Entangled Qutrits and Their Use for Quantum Bit Commitment," Physical Review Letters **93**, 053601 (2004).

[69] J. T. Barreiro, N. K. Langford, N. A. Peters, and P. G. Kwiat, "Generation of Hyperentangled Photon Pairs," Physical Review Letters **95**, 260501 (2005).

[70] E. Nagali, L. Sansoni, F. Sciarrino, F. De Martini, L. Marrucci, B. Piccirillo, E. Karimi, and E. Santamato, "Optimal quantum cloning of orbital angular momentum photon qubits through HongOuMandel coalescence," Nature Photonics **3**, 720–723 (2009).

[71] E. Karimi, D. Giovannini, E. Bolduc, N. Bent, F. M. Miatto, M. J. Padgett, and R. W. Boyd, "Exploring the quantum nature of the radial degree of freedom of a photon via Hong-Ou-Mandel interference," Physical Review A **89**, 013829 (2014).

[72] A. Mohanty, M. Zhang, A. Dutt, S. Ramelow, P. Nussenzveig, and

M. Lipson, "Quantum interference between transverse spatial waveguide modes," Nature Communications **8**, 14010 (2017).

[73] G. Corrielli, A. Crespi, R. Geremia, R. Ramponi, L. Sansoni, A. Santinelli, P. Mataloni, F. Sciarrino, and R. Osellame, "Rotated waveplates in integrated waveguide optics," Nature Communications **5** (2014).

[74] C. Xiong, X. Zhang, A. Mahendra, J. He, D.-Y. Choi, C. J. Chae, D. Marpaung, A. Leinse, R. G. Heideman, M. Hoekman, C. G. H. Roeloffzen, R. M. Oldenbeuving, P. W. L. van Dijk, C. Taddei, P. H. W. Leong, and B. J. Eggleton, "Compact and reconfigurable silicon nitride time-bin entanglement circuit," Optica **2**, 724 (2015).

[75] A. Peruzzo, A. Laing, A. Politi, T. Rudolph, and J. L. O'Brien, "Multimode quantum interference of photons in multiport integrated devices," Nature Communications **2**, 224 (2011).

[76] L.-T. Feng, M. Zhang, Z.-Y. Zhou, M. Li, X. Xiong, L. Yu, B.-S. Shi, G.-P. Guo, D.-X. Dai, X.-F. Ren, and G.-C. Guo, "On-chip coherent conversion of photonic quantum entanglement between different degrees of freedom," Nature Communications **7**, 11985 (2016).

[77] M. F. Saleh, B. E. A. Saleh, and M. C. Teich, "Modal, spectral, and polarization entanglement in guided-wave parametric down-conversion," Physical Review A **79**, 053842 (2009).

[78] D. Bharadwaj, K. Thyagarajan, M. Karpinski, and K. Banaszek, "Generation of higher-dimensional modal entanglement using a three-waveguide directional coupler," Physical Review A **91**, 033824 (2015).

[79] Y.-D. Yang, Y. Li, Y.-Z. Huang, and A. W. Poon, "Silicon nitride three-mode division multiplexing and wavelength-division multiplexing using asymmetrical directional couplers and microring resonators," Optics Express **22**, 22172 (2014).

[80] L. F. Frellsen, Y. Ding, O. Sigmund, and L. H. Frandsen, "Topology optimized mode multiplexing in silicon-on-insulator photonic wire waveguides," Optics Express **24**, 16866 (2016).

[81] L. H. Gabrielli, D. Liu, S. G. Johnson, and M. Lipson, "On-chip transformation optics for multimode waveguide bends," Nature Communications **3**, 1217 (2012).

[82] S.-Y. Tseng, Y. Kim, C. J. K. Richardson, and J. Goldhar, "Implementation of discrete unitary transformations by multimode waveguide holograms," Applied Optics **45**, 4864–4872 (2006).

[83] E. Nagali, L. Sansoni, L. Marrucci, E. Santamato, and F. Sciarrino, "Experimental generation and characterization of single-photon hybrid ququarts based on polarization and orbital angular momentum encoding," Physical Review A **81**, 052317 (2010).

[84] S. Ramelow, A. Farsi, S. Clemmen, D. Orquiza, K. Luke, M. Lipson, and A. L. Gaeta, "Silicon-Nitride Platform for Narrowband Entangled Photon Generation," arXiv:1508.04358 [physics, physics:quant-ph] (2015). ArXiv: 1508.04358.

[85] A. Dutt, K. Luke, S. Manipatruni, A. L. Gaeta, P. Nussenzveig, and M. Lipson, "On-Chip Optical Squeezing," Physical Review Applied **3**, 044005 (2015).

[86] A. Yariv, "Coupled-mode theory for guided-wave optics," IEEE Journal of Quantum Electronics **9**, 919–933 (1973).

[87] D. C. Burnham and D. L. Weinberg, "Observation of Simultaneity in Parametric Production of Optical Photon Pairs," Physical Review Letters **25**, 84–87 (1970).

[88] J. S. Fakonas, H. Lee, Y. A. Kelaita, and H. A. Atwater, "Two-plasmon quantum interference," Nature Photonics **8**, 317–320 (2014).

[89] M. Zukowski, A. Zeilinger, and M. A. Horne, "Realizable higher-dimensional two-particle entanglements via multiport beam splitters," Physical Review A **55**, 2564–2579 (1997).

[90] M. Bachmann, P. A. Besse, and H. Melchior, "General self-imaging properties in N N multimode interference couplers including phase relations," Applied Optics **33**, 3905 (1994).

[91] S.-Y. Tseng, C. Fuentes-Hernandez, D. Owens, and B. Kippelen, "Variable splitting ratio 2 2 MMI couplers using multimode waveguide holograms," Optics Express **15**, 9015 (2007).

[92] W. A. Zortman, D. C. Trotter, and M. R. Watts, "Silicon photonics manufacturing," Optics Express **18**, 23598 (2010).

[93] L. F. Nicolas-Alonso and J. Gomez-Gil, "Brain Computer Interfaces, a Review," Sensors **12**, 1211–1279 (2012).

[94] M. Scanziani and M. Husser, "Electrophysiology in the age of light," Nature **461**, 930–939 (2009).

[95] R. Yuste, "From the neuron doctrine to neural networks," Nature Reviews Neuroscience **16**, 487–497 (2015).

[96] F. A. Azevedo, L. R. Carvalho, L. T. Grinberg, J. M. Farfel, R. E. Ferretti, R. E. Leite, W. J. Filho, R. Lent, and S. Herculano-Houzel, "Equal numbers of neuronal and nonneuronal cells make the human brain an isometrically scaled-up primate brain," The Journal of Comparative Neurology **513**, 532–541 (2009).

[97] S. Herculano-Houzel, "The human brain in numbers: a linearly scaled-up primate brain," Frontiers in Human Neuroscience **3** (2009).

[98] J. A. Cardin, M. Carln, K. Meletis, U. Knoblich, F. Zhang, K. Deisseroth, L.-H. Tsai, and C. I. Moore, "Driving fast-spiking cells induces gamma rhythm and controls sensory responses," Nature **459**, 663–667 (2009).

[99] V. S. Sohal, F. Zhang, O. Yizhar, and K. Deisseroth, "Parvalbumin neurons and gamma rhythms enhance cortical circuit performance," Nature **459**, 698–702 (2009).

[100] F. Zhang, J. Vierock, O. Yizhar, L. E. Fenno, S. Tsunoda, A. Kianianmomeni, M. Prigge, A. Berndt, J. Cushman, J. Polle, J. Magnuson, P. Hegemann, and K. Deisseroth, "The Microbial Opsin Family of Optogenetic Tools," Cell **147**, 1446–1457 (2011).

[101] K. Deisseroth, "Optogenetics," Nature Methods **8**, 26–29 (2011).

[102] J. Y. Cohen, S. Haesler, L. Vong, B. B. Lowell, and N. Uchida, "Neuron-type-specific signals for reward and punishment in the ventral tegmental area," Nature **482**, 85–88 (2012).

[103] H. E. Covington, M. K. Lobo, I. Maze, V. Vialou, J. M. Hyman, S. Zaman, Q. LaPlant, E. Mouzon, S. Ghose, C. A. Tamminga, R. L. Neve, K. Deisseroth, and E. J. Nestler, "Antidepressant Effect of Optogenetic Stimulation of the Medial Prefrontal Cortex," Journal of Neuroscience **30**, 16082–16090 (2010).

[104] J. B. Bryson, C. B. Machado, M. Crossley, D. Stevenson, V. Bros-Facer, J. Burrone, L. Greensmith, and I. Lieberam, "Optical Control of Muscle Function by Transplantation of Stem Cell-Derived Motor Neurons in Mice," Science **344**, 94–97 (2014).

[105] N. Olofsson, I. Lazaridis, K. Meletis, M. Carln, U. Tingstrom, and H. Karlsson, "Lasers, Optics Enhance Optogenetics Studies," .

[106] S. L. Jacques, "Optical properties of biological tissues: a review," Physics in Medicine and Biology **58**, R37–R61 (2013).

[107] N. G. Horton, K. Wang, D. Kobat, C. G. Clark, F. W. Wise, C. B. Schaffer, and C. Xu, "In vivo three-photon microscopy of subcortical structures within an intact mouse brain," Nature Photonics **7**, 205–209 (2013).

[108] S. J. Husson, A. Gottschalk, and A. M. Leifer, "Optogenetic manipulation of neural activity in *C. elegans* : From synapse to circuits and behaviour," Biology of the Cell **105**, 235–250 (2013).

[109] J. Yoon, M. Lee, K. Lee, N. Kim, J. M. Kim, J. Park, H. Yu, C. Choi, W. D. Heo, and Y. Park, "Optogenetic control of cell signaling pathway through scattering skull using wavefront shaping," Scientific Reports **5** (2015).

[110] A. M. Aravanis, L.-P. Wang, F. Zhang, L. A. Meltzer, M. Z. Mogri, M. B. Schneider, and K. Deisseroth, "An optical neural interface: *in vivo* control of rodent motor cortex with integrated fiberoptic and optogenetic technology," Journal of Neural Engineering **4**, S143–S156 (2007).

[111] F. Zhang, V. Gradinaru, A. R. Adamantidis, R. Durand, R. D. Airan, L. de Lecea, and K. Deisseroth, "Optogenetic interrogation of neural circuits: technology for probing mammalian brain structures," Nature Protocols **5**, 439–456 (2010).

[112] K. Jiang, "Optogenetics without the genetics Science Life," (2015).

[113] J. P. Rickgauer and D. W. Tank, "Two-photon excitation of channelrhodopsin-2 at saturation," Proceedings of the National Academy of Sciences **106**, 15025–15030 (2009).

[114] A. M. Packer, L. E. Russell, H. W. P. Dalgleish, and M. Husser, "Simultaneous all-optical manipulation and recording of neural circuit activity with cellular resolution in vivo," Nature Methods **12**, 140–146 (2014).

[115] E. Papagiakoumou, F. Anselmi, A. Bgue, V. de Sars, J. Glckstad, E. Y. Isacoff, and V. Emiliani, "Scanless two-photon excitation of channelrhodopsin-2," Nature Methods **7**, 848–854 (2010).

[116] B. K. Andrasfalvy, B. V. Zemelman, J. Tang, and A. Vaziri, "Two-photon single-cell optogenetic control of neuronal activity by sculpted light," Proceedings of the National Academy of Sciences **107**, 11981–11986 (2010).

[117] W. Yang, J.-e. Miller, L. Carrillo-Reid, E. Pnevmatikakis, L. Paninski, R. Yuste, and D. Peterka, "Simultaneous Multi-plane Imaging of Neural Circuits," Neuron **89**, 269–284 (2016).

[118] G. Duemani Reddy, K. Kelleher, R. Fink, and P. Saggau, "Three-dimensional random access multiphoton microscopy for functional imaging of neuronal activity," Nature Neuroscience **11**, 713–720 (2008).

[119] G. Katona, G. Szalay, P. Mak, A. Kaszs, M. Veress, D. Hillier, B. Chiovini, E. S. Vizi, B. Roska, and B. Rzsa, "Fast two-photon in vivo imaging with three-dimensional random-access scanning in large tissue volumes," Nature Methods **9**, 201–208 (2012).

[120] F. Pisanello, L. Sileo, I. Oldenburg, M. Pisanello, L. Martiradonna, J. Assad, B. Sabatini, and M. DeVittorio, "Multipoint-Emitting Optical Fibers for Spatially Addressable InVivo Optogenetics," Neuron **82**, 1245–1254 (2014).

[121] F. Pisanello, G. Mandelbaum, M. Pisanello, I. A. Oldenburg, L. Sileo, J. E. Markowitz, R. E. Peterson, A. Della Patria, T. M. Haynes, M. S. Emara, B. Spagnolo, S. R. Datta, M. De Vittorio, and B. L. Sabatini, "Dynamic illumination of spatially restricted or large brain volumes via a single tapered optical fiber," Nature Neuroscience **20**, 1180–1188 (2017).

[122] F. Wu, E. Stark, P.-C. Ku, K. Wise, G. Buzski, and E. Yoon, "Monolithically Integrated LEDs on Silicon Neural Probes for High-Resolution Optogenetic Studies in Behaving Animals," Neuron **88**, 1136–1148 (2015).

[123] R. Scharf, T. Tsunematsu, N. McAlinden, M. D. Dawson, S. Sakata, and K. Mathieson, "Depth-specific optogenetic control in vivo with a scalable, high-density LED neural probe," Scientific Reports **6**, 28381 (2016).

[124] N. McAlinden, D. Massoubre, E. Richardson, E. Gu, S. Sakata, M. D. Dawson, and K. Mathieson, "Thermal and optical characterization of micro-

LED probes for in vivo optogenetic neural stimulation," Optics Letters **38**, 992 (2013).

[125] N. McAlinden, E. Gu, M. D. Dawson, S. Sakata, and K. Mathieson, "Optogenetic activation of neocortical neurons in vivo with a sapphire-based micro-scale LED probe," Frontiers in Neural Circuits p. 25 (2015).

[126] C. Griffin, E. Gu, H. W. Choi, C. W. Jeon, J. M. Girkin, M. D. Dawson, and G. McConnell, "Beam divergence measurements of InGaNGaN microarray light-emitting diodes using confocal microscopy," Applied Physics Letters **86**, 041111 (2005).

[127] T.-i. Kim, J. G. McCall, Y. H. Jung, X. Huang, E. R. Siuda, Y. Li, J. Song, Y. M. Song, H. A. Pao, R.-H. Kim, C. Lu, S. D. Lee, I.-S. Song, G. Shin, R. Al-Hasani, S. Kim, M. P. Tan, Y. Huang, F. G. Omenetto, J. A. Rogers, and M. R. Bruchas, "Injectable, Cellular-Scale Optoelectronics with Applications for Wireless Optogenetics," Science **340**, 211–216 (2013).

[128] I. J. Cho, H. W. Baac, and E. Yoon, "A 16-site neural probe integrated with a waveguide for optical stimulation," in "2010 IEEE 23rd International Conference on Micro Electro Mechanical Systems (MEMS)," (2010), pp. 995–998.

[129] Y. Son, H. Jenny Lee, J. Kim, H. Shin, N. Choi, C. Justin Lee, E.-S. Yoon, E. Yoon, K. D. Wise, T. Geun Kim, and I.-J. Cho, "In vivo optical modulation of neural signals using monolithically integrated two-dimensional neural probe arrays," Scientific Reports **5**, 15466 (2015).

[130] A. N. Zorzos, E. S. Boyden, and C. G. Fonstad, "Multiwaveguide implantable probe for light delivery to sets of distributed brain targets," Optics Letters **35**, 4133 (2010).

[131] A. N. Zorzos, J. Scholvin, E. S. Boyden, and C. G. Fonstad, "Three-dimensional multiwaveguide probe array for light delivery to distributed brain circuits," Optics Letters **37**, 4841 (2012).

[132] E. Segev, J. Reimer, L. C. Moreaux, T. M. Fowler, D. Chi, W. D. Sacher, M. Lo, K. Deisseroth, A. S. Tolias, A. Faraon, and M. L. Roukes, "Patterned photostimulation via visible-wavelength photonic probes for deep brain optogenetics," Neurophotonics **4**, 011002 (2016).

[133] A. M. Shanes, "Electrochemical aspects of physiological and pharmaco-

logical action in excitable cells. II. The action potential and excitation," Pharmacological Reviews **10**, 165–273 (1958).

[134] C. K. Kim, A. Adhikari, and K. Deisseroth, "Integration of optogenetics with complementary methodologies in systems neuroscience," Nature Reviews Neuroscience **18**, 222–235 (2017).

[135] M. Shein-Idelson, L. Pammer, M. Hemberger, and G. Laurent, "Large-scale mapping of cortical synaptic projections with extracellular electrode arrays," Nature Methods **14**, 882–890 (2017).

[136] Z. Israel and K. J. Burchiel, eds., *Microelectrode Recording in Movement Disorder Surgery* (Georg Thieme Verlag, Stuttgart, 2004). DOI: 10.1055/b-002-56126.

[137] R. Yuste and W. Denk, "Dendritic spines as basic functional units of neuronal integration," Nature; London **375**, 682–4 (1995).

[138] A. C. Kwan, "What Can Population Calcium Imaging Tell Us About Neural Circuits?" Journal of Neurophysiology **100**, 2977–2980 (2008).

[139] C. Stosiek, O. Garaschuk, K. Holthoff, and A. Konnerth, "In vivo two-photon calcium imaging of neuronal networks," Proceedings of the National Academy of Sciences **100**, 7319–7324 (2003).

[140] T.-W. Chen, T. J. Wardill, Y. Sun, S. R. Pulver, S. L. Renninger, A. Baohan, E. R. Schreiter, R. A. Kerr, M. B. Orger, V. Jayaraman, L. L. Looger, K. Svoboda, and D. S. Kim, "Ultrasensitive fluorescent proteins for imaging neuronal activity," Nature **499**, 295–300 (2013).

[141] Y. Gong, C. Huang, J. Z. Li, B. F. Grewe, Y. Zhang, S. Eismann, and M. J. Schnitzer, "High-speed recording of neural spikes in awake mice and flies with a fluorescent voltage sensor," Science **350**, 1361–1366 (2015).

[142] L. Jin, Z. Han, J. Platisa, J. Wooltorton, L. Cohen, and V. Pieribone, "Single Action Potentials and Subthreshold Electrical Events Imaged in Neurons with a Fluorescent Protein Voltage Probe," Neuron **75**, 779–785 (2012).

[143] S. H. Yun and S. J. J. Kwok, "Light in diagnosis, therapy and surgery," Nature Biomedical Engineering **1**, 0008 (2017).

[144] J. K. Doylend, M. J. R. Heck, J. T. Bovington, J. D. Peters, L. A. Coldren, and

J. E. Bowers, "Two-dimensional free-space beam steering with an optical phased array on silicon-on-insulator," Optics Express **19**, 21595–21604 (2011).

[145] F. Aflatouni, B. Abiri, A. Rekhi, and A. Hajimiri, "Nanophotonic coherent imager," Optics Express **23**, 5117 (2015).

[146] Q. Xu, B. Schmidt, S. Pradhan, and M. Lipson, "Micrometre-scale silicon electro-optic modulator," Nature **435**, 325–327 (2005).

[147] C. T. Phare, Y.-H. Daniel Lee, J. Cardenas, and M. Lipson, "Graphene electro-optic modulator with 30 GHz bandwidth," Nature Photonics **9**, 511–514 (2015).

[148] M. Soltani, J. Lin, R. A. Forties, J. T. Inman, S. N. Saraf, R. M. Fulbright, M. Lipson, and M. D. Wang, "Nanophotonic trapping for precise manipulation of biomolecular arrays," Nature Nanotechnology **9**, 448–452 (2014).

[149] X. Cai, J. Wang, M. J. Strain, B. Johnson-Morris, J. Zhu, M. Sorel, J. L. O'Brien, M. G. Thompson, and S. Yu, "Integrated Compact Optical Vortex Beam Emitters," Science **338**, 363–366 (2012).

[150] A. Mohanty, Q. Li, M. A. Tadayon, G. R. Bhatt, J. Cardenas, S. A. Miller, A. Kepecs, and M. Lipson, "Reconfigurable visible nanophotonic switch for optogenetic applications (Conference Presentation)," (2017), p. 100520D.

[151] E. Shim, Y. Chen, S. Masmanidis, and M. Li, "Multisite silicon neural probes with integrated silicon nitride waveguides and gratings for optogenetic applications," Scientific Reports **6**, 22693 (2016).

[152] L. Hoffman, M. Welkenhuysen, A. Andrei, S. Musa, Z. Luo, S. Libbrecht, S. Severi, P. Soussan, V. Baekelandt, S. Haesler, G. Gielen, R. Puers, and D. Braeken, "High-density optrode-electrode neural probe using SixNy photonics for in vivo optogenetics," (IEEE, 2015), pp. 29.5.1–29.5.4.

[153] L. Hoffman, A. Subramanian, P. Helin, B. Du Bois, R. Baets, P. Van Dorpe, G. Gielen, R. Puers, and D. Braeken, "Low Loss CMOS-Compatible PECVD Silicon Nitride Waveguides and Grating Couplers for Blue Light Optogenetic Applications," IEEE Photonics Journal **8**, 1–11 (2016).

[154] M. Welkenhuysen, L. Hoffman, Z. Luo, A. De Proft, C. Van den Haute,

V. Baekelandt, Z. Debyser, G. Gielen, R. Puers, and D. Braeken, "An integrated multi-electrode-optrode array for in vitro optogenetics," Scientific Reports **6**, 20353 (2016).

[155] T. Goh, M. Yasu, K. Hattori, A. Himeno, M. Okuno, and Y. Ohmori, "Low loss and high extinction ratio strictly nonblocking 1616 thermooptic matrix switch on 6-in wafer using silica-based planar lightwave circuit technology," Journal of Lightwave Technology **19**, 371–379 (2001).

[156] A. Khilo, M. A. Popovi, M. Araghchini, and F. X. Krtner, "Efficient planar fiber-to-chip coupler based on two-stage adiabatic evolution," Optics Express **18**, 15790 (2010).

[157] D. Kvitsiani, S. Ranade, B. Hangya, H. Taniguchi, J. Z. Huang, and A. Kepecs, "Distinct behavioural and network correlates of two interneuron types in prefrontal cortex," Nature **498**, 363–366 (2013).

[158] X. Chen, C. Li, C. Fung, S. Lo, and H. Tsang, "Apodized Waveguide Grating Couplers for Efficient Coupling to Optical Fibers," IEEE Photonics Technology Letters **22**, 1156–1158 (2010).

[159] K. K. Mehta and R. J. Ram, "Precise and diffraction-limited waveguide-to-free-space focusing gratings," Scientific Reports **7** (2017).

[160] D. N. Hutchison, J. Sun, J. K. Doylend, R. Kumar, J. Heck, W. Kim, C. T. Phare, A. Feshali, and H. Rong, "High-resolution aliasing-free optical beam steering," Optica **3**, 887 (2016).